THE UNIVERSITY *of* EDINBURGH

In-situ diagnostics of the packed bed in post-combustion CO_2 capture using electrical capacitance tomography

Yuan Chen

THE UNIVERSITY *of* EDINBURGH

Thesis submitted to the degree of Doctor of Philosophy

The University of Edinburgh
School of Engineering

August 2022

Declaration

I hereby declare that the work presented in this thesis is my own unless otherwise acknowledged. This thesis has not been submitted for any other degree or professional qualification except to The University of Edinburgh for the degree of Doctor of Philosophy.

Yuan Chen

Date: 26/08/2022

Acknowledgements

I would like to my principal supervisor Dr Chang Liu, for his insightful guidance and encouragement. Thank you for always been there to help and push me beyond my limits. All of my achievements would not have been possible without his expertise, assistance and suggestions. I want to thank my co-supervisors Dr Jiabin Jia and Dr Mathieu Lucquiaud for their feedback and guidance throughout my PhD journey has been invaluable in my development as a researcher. I would also like to thank Dr Yunjie Yang. His help in operating and testing the ECT test rigs has been invaluable.

The Agile Tomography group has grown considerably since I first started working in Edinburgh. Thanks to everyone in the group for providing a friendly and collaborative work environment. Even though we will be spread throughout the world, I will always remember all the good memories in Edinburgh fondly. I also learned a lot from Dr Hancong Wu, Dr Yong Bao, Dr Paul Tait and Dr Godwin Enemali, either by discussing problems with them or through osmosis from listening to other conversations.

In addition, I would like to thank Dr Carolina Font-Palma and Dr David Cann of the University of Hull, without whom a significant portion of this thesis would not have been possible. I would also like to thank the assistance I have had from technicians at the School of Engineering. Mr Derek Watson helped me modify the test rig, and Mr Douglas Carmichael for help with LabVIEW programming.

Most importantly, my gratitude to my parents Mrs Meifang Zhou and Mr Jinhua Chen is beyond measure. Throughout my life, they have always sacrificed to ensure that I had the best opportunities possible, and they have constantly believed in me, encouraged me to dream big and helped me pursue those dreams. I cannot express my gratitude for their support over the years and I dedicate this thesis to them.

Lay Summary

The post-combustion capture process is a crucially important climate change mitigation technology. The thesis explores the connection between the liquid holdup and the optimal process control and operation of the post-combustion capture process by using Electrical Capacitance Tomography (ECT). ECT is a non-destructive imaging technique that monitors the permittivity distribution in a confined space. Compared with other imaging techniques, ECT has the advantages of low cost, fast imaging speed, non-destructive and non-invasive nature. Therefore, it has been widely applied in industrial process tomography, including multiphase flow imaging, fluidized beds imaging, bubbling beds imaging, and flame imaging.

This thesis aims to apply ECT to real-time packed column imaging and improve the performance of ECT in liquid holdup calculation. The successful development of an online measurements system using ECT would result in an effective solution to the requirements of carbon capture applications that need to *in situ* diagnosis of packed column. To achieve this objective, the thesis demonstrates the design and implementation of the ECT sensor, from the perspective of data collection system improvement, a more convenient flooding diagnosis method, a highly accurate and precise liquid holdup estimation method and better tomographic image reconstruction methods for the test rigs. Lab-scale test campaigns were carried out at two different post-combustion test rigs to investigate the effects of varying packed column process variables on CO_2 capture efficiency. The first experiment was carried out on a counter-current flow packed column, while the second was carried out on a cryogenic carbon capture packed column. The knowledge of packed column cross-sectional images and hydrodynamics were used to demonstrate, for the first time, diagnostics of the packed column using *in situ* online measurements using ECT. These novel methods can be used in combination with advanced process control strategies to improve the safety, flexibility and efficiency of post-combustion capture plants.

Contents

List of Figures

List of Tables

Abbreviations

A3C	Advanced Cryogenic Carbon Capture
BAU	Business as Usual
CCS	Carbon Capture and Storage
CCUS	Carbon Capture Utilisation and Storage
CLC	Chemical Looping Combustion
ECT	Electrical Capacitance Tomography
ECI	Electrical Capacitance Image
FEM	Finite Element Method
LBP	Local Binary Patterns
LPM	Litres Per Minute
LNG	Liquefied Natural Gas
MEA	Monoethanolamine
PTFE	Polytetrafluoroethylene
SNR	Signal-to-Noise Ratio
SGDM	Stochastic Gradient Descent with a Momentum
RMSE	Root Mean Square Error
ID	Inside Diameter
IR	Infra-Red
OD	Outer Diameter

WLR Water to Liquid Ratio

3D Three Dimensional

List of symbols

α	Void fraction
α_{liquid}	Water liquid ratio
A	Cross-sectional area of the capture column
C_l	Capacitance when the column is filled with plastic packing and air
C_f	Capacitance when the packed column is flooding
C_F	Capacitance when the packed column is filled with water
C_{norm}	Normalized capacitance
C_{mea}	Measured capacitance
C_{ref}	Reference capacitance
C_l	Low-permittivity calibration capacitances
C_h	High-permittivity calibration capacitances
ε	Permittivity of material
ε_{gas}	Permittivity of air
ε_{liquid}	Permittivity of liquid
T	Temperature
M	Number of measurements
Q	Air volumetric flow rate
G	Normalized permittivity change
S	Sensitivity map matrix

J	Index of the measurement
N	Maximum number of ECT measurements, 28 in this study
K	Pixel number of the sensitive field
w	Maximum number of pixels
n	Total number of sensors
ΔP	Pressure drop
ΔP_{irr}	Pressure drop through an irrigated packed column
P_f	Flooding index
h	Height
c	CNN input ECI
θ	Hyperparameters of CNN-ECI
h_L	Liquid holdup
h_0	Liquid holdup below the loading point
g	Gravitational constant
Z	Total height of packing
L_2	Regularisation term
w	Weight vector
λ	Regularisation coefficient
Ω	Regularisation function
y	Volume fraction of CO_2 in the gas phase

v	Superficial velocity
c_p	Specific heat capacity of the packing material
ρ	Density
ρ_L	Density of liquid
U_{frost}	Frost front velocity
U_L	Liquid loading
Q_g	Cooling duty required by the gas phase
Fr_L	Froude number for liquid
dT	Temperature change
E_{RMS}	Root mean square error
x	Measurement path-dependent empirical parameter

Publication List

Below is a list of published articles and datasets based on the work in this PhD programme.

Journal Papers

1. **Y. Chen**, C. Liu, Y. Yang, M. Lucquiaud, J. Jia, Flooding Prognostic in Packed Columns based on Electrical Capacitance Tomography and Convolution Neural Network. IEEE Transactions on Instrumentation and Measurement, vol. 71, pp. 1-14, 2022.

2. **Y. Chen**, D. Cann, J. Jia, C. Font-Palma, Preliminary Study of CO_2 Frost Formation during Cryogenic Carbon Capture using Tomography Analysis, Fuel, vol. 328, p. 125271, 2022.

3. **Y. Chen,** G. Chinello, P. Tait, J. Jia, A new correlation to determine the Lockhart-Martinelli parameter from vertical differential pressure for horizontal Venturi tube over-reading correction, Flow Measurement and Instrumentation, 2022. (Submitted).

4. Z. Li, **Y. Chen**, Y. Yang, C. Liu, M. Lucquiaud, J. Jia, Flow regime transition in counter-current packed column monitored by ECT, Chemical engineering journal 420 (2021) 129841.

5. P. Tait, **Y. Chen**, W. Senjyu, T. Watanabe, Y. Inamura, V. Presotto, R. Mojsak, G. Chinello, J. Jia, Determination of Void Fraction in Wet-Gas Vertical Flows via Differential Pressure Measurement, Flow Measurement and Instrumentation 83 (2021) 102080.

Conference Papers

6. **Y. Chen**, Z. Li, Y. Yang, J. Jia, C. Liu, M. Lucquiaud, Simulation of Flooding Phenomenon in Packed Column using Electrical Capacitance Tomography, 2019 IEEE International Conference on Imaging Systems and Techniques (IST), IEEE, 2019.

Dataset

7. **Y. Chen**, C. Liu, Y. Yang, M. Lucquiaud, J. Jia, Dataset for "CNN-aided Flooding Prognostic in Packed Column using Electrical Capacitance Tomography.", University of Edinburgh, 2021, Edinburgh DataShare, https://doi.org/10.7488/ds/3151

8. P. Tait, **Y. Chen**, W. Senjyu, T. Watanabe, Y. Inamura, V. Presotto, R. Mojsak, G. Chinello, J. Jia, Dataset for "Determination of Void Fraction in Wet-Gas Vertical Flows via Differential Pressure Measurement", University of Edinburgh, 2021, Edinburgh DataShare, https://doi.org/10.7488/ds/3168

9. C. Font-Palma, J. Jia, **Y. Chen**, and D. Cann, Electrical Capacitance Tomography and Temperature profiles data for the experiment of CO2 frost formation during cryogenic carbon capture with tomography analysis at The University of Chester, 2020, UKCCSRC Data and Information Archive, https://www2.bgs.ac.uk/ukccs/accessions/projects.html#item162545?projectID=20909612

Abstract

Climate change is commonly acknowledged as a result of increased greenhouse gas levels in the atmosphere. The excess use of fossil fuels and consequential emission of greenhouse gases is causing global warming. Global warming or climate change is a global issue that requires concerted efforts on a planetary scale to reduce the amount of carbon accumulated into the atmosphere. Post-combustion capture with amine solvents is the most matured technology and plays an essential role in addressing the issue of CO_2 emission. Flooding phenomenon is an operation problem exists in post-combustion process, which reduces CO_2 capture efficiency and causes potential damage to the equipment. This process must be avoided to ensure continued carbon dioxide absorption. However, knowledge of the flow regime transition process involved in flooding is currently limited due to a lack of an *in situ* diagnostic technique for process monitoring and a lack of comprehensive datasets which reflect the practical carbon capture process. Furthermore, the nature of interface of air and liquid during flooding onset is not well known and according to correlations for flooding point and packed column capacity estimation, which have uncertainties of up to $\pm$30%. The inability to accurately operate the carbon capture process could lead to a decrease in CO_2 capture efficiency, safety issues, oversizing of the packed column and increased CO_2 capture costs.

The work described in this thesis proposes to diagnose packed columns in the post-combustion capture process through electrical capacitance tomography (ECT) as a real-time qualitative and quantitative imaging method. Comprehensive packed column models have been built for each post-combustion carbon capture system, using COMSOL Multiphysics with MATLAB as the simulation software. To ensure an objective simulation of the performance of ECT in different post-combustion carbon capture systems, the representation of packed column geometry structure and material electrical permittivity have been verified and calibrated based on real-scenario test conditions. For each carbon capture system, many parametric simulations were performed to evaluate the effect on tomographic imaging. The correctional images of post-combustion carbon capture packed column were reconstructed from the simulation data and the feasibility of ECT for packed column diagnosis was evaluated.

To further validate the feasibility of ECT, a laboratory-scale test campaign on two different types of post-combustion test rigs were conducted to investigate the effect of different packed column process variables on tomographic images. The column constitutes a transparent pipe filled with packing material, in which is easy to observe the flooding onset and flow regime transition. The liquid distribution and holdup are monitored through ECT, which allows variations in the predominant characteristics of flooding events to be investigated in greater detail than in previous research. Furthermore, combined with Convolutional Neural Networks (CNN), ECT enables a high degree of accuracy with only $\pm 1\%$ error on liquid holdup calculation and greater robustness in environments affected by flooding with strong turbulence flow. In addition, ECT technology has attracted great interest in the field of cryogenic carbon capture, which captures CO_2 by cryogenically desubliming CO_2 out of the flue gas as CO_2 frost on the cold surfaces of the heat exchangers. The technique was found to provide half the cost and energy of the state-of-the-art carbon capture methods. However, this process could lead to several operational problems, such as plugging. ECT could help a process engineer to understand the process of frost formation and provide key tomographic images and process parameters to facilitate cryogenic carbon capture implementation. The successful development of an ECT system would result in an *in situ*, agile, non-intrusive and low-cost monitoring tool for the requirements of packed column diagnosis.

Chapter 1 Introduction

1.1 Background and motivation

The World Health Organisation (WHO) has declared that climate change is the greatest threat to global health in the 21st century [1]. Climate change and global warming are widely believed to be a result of greenhouse gas (GHG) emissions, primarily CO_2 [2]. Greenhouse gases stay in the atmosphere, where they are transparent to sunlight. When the Earth emits that heat as infra-red (IR), radiation, the greenhouse gases absorb it and reflect the heat back to earth. This creates a greenhouse effect and increasing levels of CO_2 emitted to atmosphere is causing global warming.

Post-combustion capture (PCC) technologies are essential in addressing the problem of CO_2 emission [3]. The chemical absorption and scrubbing process are mature and proven methods of capturing CO_2 from point sources [4]. However, carbon dioxide absorption rate in packed column will be limited by the tendency of the column to flood [5]. The occurrence of flooding is a significant drawback of various counter-current operations such as amine-based carbon capture [6]. To avoid flooding, the PCC packed column design needs to consider the flooding point. The pressure drop is a key factor indicating the flooding phenomenon in packed columns. However, the pressure drop cannot provide information about the liquid distribution holdup and liquid holdup of packed columns [7]. The liquid holdup is interesting as it could indicate flooding, hydrodynamics and mass transfer in a packed column [8]. In addition, both liquid and vapour maldistribution could significantly affect packing efficiency [9]. Therefore, real-time monitoring of liquid holdup and liquid distribution is imperative for safely operating packed columns.

First developed in the late 1980s, ECT is a tomographic imaging modality to visualize the conductivity distribution within the sensing area [10]. ECT's basic working principle is to apply electric voltage to selected electrodes and measure the corresponding capacitance. Since its development, ECT has been widely used for monitoring industrial processes to estimate key process parameters, e.g., liquid holdup, and capture fast-change phenomena [7]. ECT has the benefit of simplicity, non-intrusiveness, rapid response time and low cost. Relevant cases include the use of ECT

for liquid distribution and holdup measurements, like fluidized bed pneumatic conveying systems, bubbling beds, and counter-current flow packed columns [7, 11-15].

In various carbon capture operation processes, a non-intrusive real-time monitoring method with a good temporal resolution is highly desirable for studying hydrodynamics and mass transfer [16]. The liquid distribution and holdup obtained would provide crucial insights into process engineering analysis. Previous research has validated ECT for measuring the liquid distribution and holdup [14]. Although ECT is less competitive than X-ray tomography in terms of spatial resolution, it could easily meet the demands of high-speed and real-time multiphase flow imaging [17]. Using tomography to detect and image liquid distribution in counter-current flows, engineers can easily diagnose the flooding phenomenon and packing efficiency, enabling a better understanding of hydrodynamics, mass transfer and design optimisation of the packed column [7]. Although the development of ECT to date is inspiring, research into the improvement of the technology is ongoing, and the challenges still exist in industry-scale carbon capture applications.

1.2 Aims and objectives

This project mainly focuses on exploring and developing the ECT technique for lab-scale experiments, with particular emphasis on absorption packed column and cryogenic packed column diagnosis. The primary goals are firstly, to exploit agile, adaptable and reliable ECT systems for real-time flooding monitoring and maldistribution diagnosis during packed column operation. Secondly, ECT will be combined with machine learning methods to characterise liquid distribution, holdup and monitor the flooding phenomenon. Finally, ECT will be applied to measure frost distribution at cryogenic carbon capture. To achieve the aims of this project, the work described in this thesis uses simulation and lab-scale experimental studies to:

- Design and construct a test rig which can be used to observe the on-site flooding for counter-current flow.

- Demonstrate the feasibility of applying ECT for packed column liquid distribution imaging.

- Conduct numerical and experimental studies on real-time flooding monitoring. Develop models to demonstrate the correlation between the flooding in the packed column and ECT data.

- Develop a machine learning model for liquid holdup prediction more accurately and flooding prediction. Perform experimental validation of developed machine learning method.

- Test ECT's the functionality in providing real-time, continuous measurements of frost formation for cryogenic carbon capture.

1.3 Main contributions

The work in this thesis is separated into two areas, the first of which involves ECT for amine-based, counter-current flow, packed column diagnosis, while the second of which describes ECT for cryogenic packed column diagnosis. The main contributions of this thesis are outlined below for each scenario:

- **Amine-based counter-current flow packed column**

    - The first use of ECT for packed column flooding imaging. A flooding index was developed for early warning of on-site flooding and is identified as the key metric for achieving optimised capture plant operation.

    - A CNN-aided ECT method was developed for high accuracy liquid holdup calculation and greater robustness in environments affected by flooding with strong turbulence flow. The proposed model is validated using experimentally measured ECT profile data.

    - A dataset of simulation and real packed column flooding scenarios was

obtained using a multimodal measurement system. The superiority of ECT is verified by comparing the results of different methods.

- **Cryogenic packed column**
    - The feasibility of ECT for cryogenic packed column frost formation imaging was investigated by comparing the reconstructed images with simulation results. This can be used to demonstrate, for the first time, an ability to monitor the cryogenic carbon capture process using real-time tomography.
    - A dataset is obtained for defining real-time CO_2 frost and frost accumulation process within a cryogenic packed column.

1.4 Thesis layout

The thesis consists of 6 chapters, the rest of which are summarised as follows.

Chapter 2 reviews the background of carbon capture, the foundations of packed columns and ECT, the ECT reconstruction algorithms, and the novel applications of ECT. Different methods of packed column diagnosis are also compared with their fundamentals introduced.

Chapter 3 details the design and construction of the ECT used for counter-current flow packed column diagnosis. The performance of the ECT system and flooding index method is evaluated in the experiments.

Chapter 4 proposes a high-accuracy and robust method for flooding monitoring using CNN-aided ECT. Results from the proposed method are compared to results from conventional methods. The compatibility of these results is also discussed.

Chapter 5 investigates the potential to apply ECT for cryogenic carbon capture applications. Ceramic beads packing were wetted as a preliminary step to simulate CO_2 frost formation. The simulations and experimental campaigns demonstrate real-

time monitoring of frost formation using ECT. The results show that ECT could effectively monitor the changes in relative permittivity caused by the frost formation in real time.

Chapter 6 summarises the overall conclusions from this work. Recommendations for future work are also discussed based on the novel development produced in the thesis.

Chapter 2 Literature review

2.1 Introduction

This thesis focuses on developing of an ECT system and utilising the system to diagnose the packing column in CO_2 capture. In order to achieve the research goals, it is essential to thoroughly study the existing literature to determine the research that has been conducted and those applicable to this thesis. This chapter will seek to identify research gaps that must be filled in order to advance the development of the diagnostics of the packing column. This thesis focuses on the tomographic analysis of the fundamentals of packed column flooding and cryogenic carbon capture packed column frosting.

In the following contexts, a detailed description of carbon capture and the need for an *in situ* diagnosis tool are provided, covering the conventional methods of flooding monitoring that have been studied. A brief description of the ECT system will be presented and the existing ECT systems for packed column imaging will be discussed. In addition, the recent advances in ECT image reconstruction algorithms and liquid holdup calculation methods are briefly summarised. Finally, a brief review of other ECT applications will be given. This chapter provides background and justification for the research undertaken and related studies conducted in the literature are discussed.

2.2 Background about carbon capture

Business-as-usual (BAU) scenarios have long been considered a baseline scenario that examines the consequences of continuing current trends in population, economy, energy, technology, and human behaviour [18]. The world's total energy consumption is projected to increase by around 25% in the BAU scenario [19]. Scientific evidence suggests that one of the dominant causes of climate change is the excessive emissions of CO_2 into the atmosphere [20]. The ambitious target of net zero-carbon emissions by 2050, agreed by the UK and other countries, has made carbon capture and storage (CCS) necessary to achieve those targets [21]. The UK is considering the long-term

development of the carbon capture utilisation and storage (CCUS) strategy and plans to implement large-scale deployment of the CCUS technology [22].

The removal of the greenhouse gas CO_2 from the burning of fossil fuels is known as carbon capture and storage technology [3]. By injecting CO_2 at a depth of several thousand metres into a geological reservoir, such as depleted oil or a saline reservoir rock [23, 24], it is possible to stop the accumulation of CO_2 in the atmosphere and permanently isolate it from the carbon cycle. The three main categories of carbon capture techniques are oxy-fuel combustion [25], post-combustion [26], and pre-combustion [27]. Adsorption [28], chemical or physical absorption [29], cryogenic [30], membrane separations [31], and chemical looping combustion (CLC) [32] are the main pre- and post-combustion carbon capture techniques.

The background of carbon capture, its necessity, and the methods of carbon capture that are now known will all be covered in this chapter. This literature review will examine studies done on amine-based post-combustion capture and cryogenic carbon capture, two of the most recent carbon capture methods.

2.2.1 Amine-based post-combustion carbon capture

Post-combustion capture is the most mature and most effective technology currently among the various carbon-capture technologies [33]. Post-combustion capture refers to the removal of CO_2 from flue gases after the combustion process occurs. This allows carbon capture and storage to be directly integrated with many industry's CO_2 emission sources, such as a power station, without making any change to the base design of industrial processes. It also means that it is possible to design new power stations in anticipation of the addition of carbon capture. Post-combustion capture relies on absorption and uses a solvent solution to capture CO_2 by the chemical or physical reaction. Among the carbon capture technologies, chemical absorption is the most mature and is widely employed due to its excellent selectivity and effectiveness at capturing CO_2 at low concentrations [34]. The recommended option is amine-based absorbents like monoethanolamine (MEA) [35].

One of the world's first and largest commercial amine solvent technology CCS integrated coal-fired power plants is the SaskPower Boundary Dam CCS Project in Estevan, Saskatchewan, Canada [36]. The plant was opened in 1959, and the CCS facility became operational in 2014 [37]. Canadian federal regulations limit the amount of CO_2 that can be released from a coal-fired unit that is reaching the end of its useful life of 50 years [38]. With boundary dam's Unit 3 reaching that mark, it was the perfect candidate for carbon capture. Unit 3 has been retrofitted with carbon capture technology, replacing the turbine. This will prolong its useful life by decades, allowing SaskPower to capture up to 90% of all greenhouse gases from this unit. Until February 2022, the CCS facility at Boundary Dam Power Station captured 41,584 tonnes of carbon dioxide [37]. The average daily capture when using CCS was 2,796 tonnes per day, with maximum capture in one day of 2,950 tonnes [37]. Building on the lessons learned here, SaskPower's case study can be applied to the most of coal-fired power stations around the world.

The main drawbacks of absorption technology include the need for large amounts of amine and large absorber columns for the solvent to effectively capture CO_2 as well as the energy-intensive regeneration of the solvent and CO_2 desorption requirements, which have a significant impact on the operational costs [39]. Amine-based solvents are now the most widely used post-combustion CO_2 capture technique. However, current technologies are too energy-intensive for widespread adoption, and emerging lower energy alternatives will require more development and demonstration under realistic conditions [40]. Other post-combustion carbon capture techniques are more suitable for large emitters. [41]. Experimental study or pilot-scale tests with inner column diameters ranging from 19 mm to 597 mm and various packing methods have been detailed in earlier research on the variables influencing post-combustion carbon capture absorption efficiency [42].

While it is possible to measure a number of process parameters in real time; including CO_2 concentration at the absorber's intake and outlet [43], stripper pressure, fuel gas flow rates, and solvent flow rates, it is still challenging to assess the solvent distribution and liquid holdup continuously [14]. This prevents it from being used as a control variable and makes it difficult to conclude how liquid flow rates react to dynamic

operations. Although studies indicate that amine-based absorption has almost reached its maximum efficiency [44], other methods, such as cryogenic carbon capture [30] and direct air capture [45], may still have the opportunity for growth.

2.2.2 Cryogenic carbon capture

Cryogenic carbon capture enables the physical phase change method of CO_2 separation from flue gas instead of a chemical separation method. There is growing interest in cryogenic carbon capture to address the need for new methods to capture CO_2 to tackle the present challenge of climate change [30]. This technique can offer a high CO_2 removal level and produce high purity of CO_2, which can be used in the food industry or to make chemicals [46]. Cryogenic processes typically use very low temperatures (about −100 °C or below) that physically separates CO_2 by desubliming out CO_2 and generating a frost. Tuinier et al. [47] show that in the presence of identical favourable circumstances and a ready cold source, cryogenic carbon capture would be a more cost-effective method of carbon capture than amine-based absorption and membrane technologies [48].

Ali et al. [49] had previously conducted investigations on energy minimisation in cryogenic beds during the purification of natural gas with a high CO_2 component. They examined how process variables such as the initial temperature of the cryogenic bed, feed composition, and feed flow rate affected the energy used, bed saturation, bed pressure, and cycle time. Font-Palma et al. [30] reviewed the different cryogenic carbon capture techniques in development, their advantages, and the challenges preventing their commercialisation. Modelling work has been done to help the prediction of CO_2 frost points of natural gas in liquefied natural gas (LNG) systems [50]. However, the excessive accumulation of CO_2 frost on a heat exchanger's surface reduces heat transfer rates, which in turn reduces process efficiency [51, 52]. Previous research identified the necessity of employing packed beds in advanced arrangements that provide periodically transition between CO_2 collection, sublimation, and bed cooling conditions [53]. Another configuration overcomes this limitation by using a moving packed bed, the advanced cryogenic carbon capture (A3C) process, which

feasibility has been assessed through modelling and economic analyses [54]. The moving bed architecture enables continual regeneration of the frosted bed material, which is subsequently recycled back into the capture column. Additionally, the velocity of CO_2 frost advance within a static packed bed could enable the construction of a moving bed column that would provide continuous CO_2 removal. [46]. To allow the cooling of bed material and CO_2 frost formation simultaneously, the effectiveness of different types of bed material was investigated for a moving bed system, and combining the precooling and capture steps within the cryogenic capture column is illustrated by Cann et al. [55].

The ability to operate at near-atmospheric pressure is an advantage of cryogenic carbon capture. But it also has problems with heat transfer efficiency. The method loses heat transfer efficiency over time as CO_2 is trapped as a layer of frost on the heat transfer surface. The capture system must periodically be shut down for regeneration in order to recover the frost from the heat transfer surface. The factors that affect overall CO_2 removal quality and efficiency in cryogenic carbon capture systems are, therefore, the initial bed temperature, inlet CO_2 fractions, packing material and the frost layer produced on the surface of packing material [56]. Water in moist air or refrigeration cycles is the main topics of research in crystal (or nucleation) and frost development. There is one report available regarding binary data of nitrogen and CO_2 mixtures for the variation of frost thickness, density and thermal conductivity in a cryogenic plate used visual inspections and images taken through the transparent packed column pipe [57]. However, these can only provide information about the frost layer at the outer circle of the packed column, and the exact amount of frost cannot be directly calculated. Thus, the study in this thesis will address this research gap through the application of ECT to better understand CO_2 frost formation under varying factors. Understanding the mechanism of frost formation within a packed column aids in the design of a new cryogenic carbon capture system.

2.3 Fundamentals of packed column

2.3.1 Properties of a packed column

A packed column is an essential equipment in many chemical unit processes, such as CO_2 absorption [58]. Due to its large capacity, low price, and high efficiency, it has drawn a lot of attention [59]. Structured packing is composed of a repeating geometric pattern and consists of a multitude of channels where a gravity-driven falling liquid film flows downwards along the packing walls in the presence of an upward flowing gas at a constant pressure gradient [60], shown in Figure 2-1. It is used in the packed column to ensure that there is a large contact area between the combustion gas and the chemical solvent to maximise carbon capture efficiency [61].

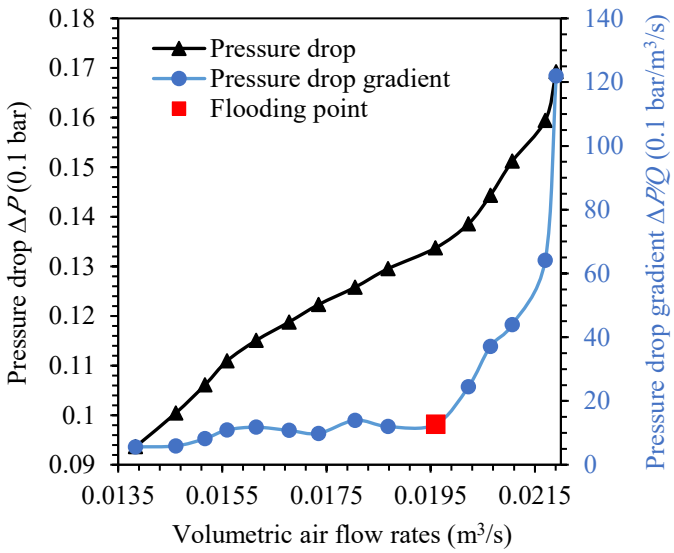

Figure 2-1: Comparison between pressure drop and pressure drop gradient across the whole packed column.

Chemical post-combustion carbon capture has a number of drawbacks, including the need for very densely packed columns and difficulty in scaling down economically for industrial applications like fertilisers, steelmaking, and refineries [39, 46]. Among the existing post-combustion carbon capture technologies, few focus on column design optimisation, which is essential for reducing the cost of investment in the capture process. It can be achieved either by developing new high-performance packing or an adequate design of packed columns [62]. However, flooding occurs in packed columns

when either the gas or liquid flow is increased beyond the capacity of the column, accompanied by a sharp increase of the pressure drop, loss of mass transfer efficiency, and heavy entrainment [63]. Features used to identify flooding regimes include the appearance of flow reversal, excessive entrainment, a sharp rise in pressure drop, a sharp rise in the liquid holdup, and a sharp fall in efficiency [6]. In this context, accurate prediction of the onset of flooding is of critical importance. Therefore, it is a common practice to design and operate absorption columns below the flooding point and achieve the best mass transfer with lower gas velocities and thus lower pressure drops. Lower gas velocities effectively cause packed column diameters to be oversized, which raises capital costs.

2.3.2 Flooding in packed columns

Flooding occurs in packed columns when either the gas or liquid flow is raised above the capacity of the column, accompanied by a sharp increase of the pressure drop, loss of mass transfer efficiency, and heavy entrainment [63]. Flooding provides a significant concern for counter-current flow in a vertical packed column. Flooding not only significantly reduces mass transfer efficiency but also has other negative effects, such as forcing liquid into gas pipelines and subsequently destroying equipment [7]. A higher pressure occurring at the bottom of the column and connected pipes can result in equipment damage, pipe leakage and even explosion. In order to provide a better explanation of the packed column flooding mechanism, the terminologies involved will be presented in detail.

- Loading point: At the loading point of a column, the gas velocity is high enough to destabilise the liquid film and influence the liquid flow. After this point, the liquid will accumulate in the column and lead to higher liquid holdup and higher pressure drop until flooding happens.

- Flooding point: Flooding point is the upper limit of the packed column operation. At this point, there is an excessive accumulation of liquid in the entire packed column.

- Liquid holdup: Liquid holdup is an important hydrodynamic property to estimate packed column performance and is defined as the ratio of the volume of a packed column occupied by the liquid to the total volume of the packed column.

Flooding points, as an indication of the upper capacity limit of a packed column, will affect packed column design. In a counter-current packed column, operating in the loading zone between the loading and flooding points is recommended to achieve a high mass transfer rate [64]. Therefore, a counter-current packed column is generally designed to 70-80% of the flooding point velocity [64, 65], or a lower boundary of 60% for safety concerns [66]. This practice provides a sufficient margin to (a) allow uncertainties associated with the prediction of the flooding point and (b) to keep the designed point away from the region where efficiency rapidly diminishes (just below the flooding point). However, this method leads to oversized packed column diameters, which reduces efficiency. When employed for CCS operations with MEA and other amines, the flooding point of structured packings may be greatly overestimated, resulting in the oversizing of packed columns for CCS operations [67].

Numerous experimental and numerical research has been conducted to determine how to prevent flooding in counter-current flow packed columns. Some studies optimised packing sizes and operating parameters [68] or packing arrangements [69] to push the flooding limits towards much higher throughputs in counter-current set-ups. However, these practices come at the expense of reducing the mass transfer rate. Furthermore, flooding still occurs accidentally even if the above measures are taken. Therefore, a safety factor, typically a percentage of the flooding velocity, is implemented to select operating gas velocities when sizing packed columns and to avoid detrimental effects on absorption efficiency. In order to prevent packed columns from flooding during operation, various empirical and theoretical flooding models have been used to predict the gas velocity at the flooding point [70, 71]. However, the accuracy of these forecasts always depend on empirical parameters related to the packed column applied, which is difficult to obtain. Failure to effectively estimate and avoid flooding may lead to a reduction in production, equipment damage, safety problems, and an oversizing of column diameters once large safety factors are implemented.

2.4 Packed column monitoring methods

2.4.1 Pressure drop

Pressure drop, liquid holdup and packed column flooding are closely linked [6]. It is generally recognised that the pressure drop inside the column is the most crucial variable for flooding prognosis [72, 73]. In the past decade, several empirical or semi-empirical correlations have been developed to determine the loading and flooding points and pressure drop in the pre-loading and loading zones for either random or structured packing [74-77]. However, there are great differences between the various correlations documented in the literature [78].

The most common pressure drop (ΔP) calculation is the Ergun equation, which could predict the dry packing pressure drop within the packed column:

$$\Delta P = \frac{150\times\mu\times L}{D_p^2}\frac{(1-\varepsilon)^2}{\varepsilon^3}v_s + \frac{1.75\times L\times\rho}{D_p}\frac{(1-\varepsilon)}{\varepsilon^3}v_s|v_s| \tag{2.1}$$

where v_s the superficial velocity of the fluid, μ the kinematic viscosity of water, L the total height of the packed column, D_p the particle diameter of bed material and ε the bed void fraction. The first and second terms in the equation represent the viscous energy losses and kinetic energy losses within the packed column, respectively. While many cases may be covered by this equation, other scholars have worked to construct pressure drop equations for particular fields.

Stichlmair et al. [79] extended the applicability of Ergun equation to describe the pressure drop of an irrigated bed. The irrigated pressure drop is obtained by iterative calculations. As a starting point, the irrigated pressure is assumed to be equal to the dry pressure drop.

$$\frac{\Delta P_{irr}}{\rho_L g Z} = \frac{\Delta P_{dry}}{\rho_L g Z}\times\frac{\left\{1-\varepsilon\left[1-\frac{h_0}{\varepsilon}\left[1+20\left(\frac{\Delta P_{irr}}{\rho_L g Z}\right)^2\right]\right]\right\}^{\left(2+\frac{C}{3}\right)}}{1-\varepsilon} \times\left[1-\frac{h_0}{\varepsilon}\left[1+20\left(\frac{\Delta P_{irr}}{\rho_L g Z}\right)^2\right]\right]^{-4.65} \tag{2.2}$$

where ΔP_{irr} is the pressure drop through an irrigated bed, ρ_L is the density of liquid, g is the gravitational constant, Z is the total height of packing, h_0 is the liquid holdup below the loading point. The results of the pressure drop from equation (2.2) on the first iteration could replace the dry pressure drop for further iterations. The above steps are repeated, and the final results are obtained until iterations do not change the pressure drop quoted. Razi et al. [80] concluded a large number of studies in the literature establishing correlations for predicting pressure drop and flooding point in packed column. The majority of cutting-edge techniques monitor pressure drop, which increases noticeably just before flooding occurs [74]. However, online flooding detection by invasive pressure transducers may delay action since proper identification of the loading point and flooding point needs a full curve of pressure drop [7].

2.4.2 Liquid holdup

The alternative to identify flooding is to monitor the increase in liquid holdup in the packed column [81]. Below the loading point, the holdup is a function only of the liquid rate. According to Jammula et al. [82], liquid holdup and film thickness in a structured packed column increases with increasing gas flow rates above the loading point. The region where there is an influence on the gas rate is commonly known as the loading region. In the loading region, the liquid will accumulate in the column and lead to higher liquid holdup and higher pressure drop until flooding happens. Several liquid holdup correlations were developed during the past few decades. The results from different correlations vary greatly and depend on the assumptions and packing type used.

For example, Billet [78] concluded in his work that the global liquid holdup below the loading point can be predicted using the following equation.

$$h_0 = 0.555 Fr_L^{\frac{1}{3}} \tag{2.3}$$

where the Froude number is defined as

$$Fr_L = U_L^2 \frac{a}{g\varepsilon^{4.65}} \tag{2.4}$$

where U_L is the liquid loading, a the specific surface area of packing, g the gravitational constant and ε the packed column void fraction. Due to the change in flow pattern after flooding occurs, the mechanism of liquid holdup is also changed. Therefore, for liquid holdup above the loading point a new correlation is required.

Since global pressure drop and global liquid holdup are closely linked [6]. Stichlmair et al. [79] concluded in their work that the influence of gas friction and the effect of the pressure gradient can be combined in a single dimensionless pressure drop term in the form $\Delta P_{irr}/(Z\rho_L g)$ and the following correlation can be used for liquid holdup above the loading point.

$$h = h_o \left[1 + 20 \left(\frac{\Delta P_{irr}}{Z\rho_L g}\right)^2\right] \tag{2.5}$$

The best example of a model that uses liquid holdup as a principal component in pressure drop and mass transfer model development is the Billet random packed model [83]. However, a major limitation of this model is its dependency on packing specific constants for model predictions. So models similar to the Billet model are necessary for structured packing without any of the Billet model's limitations.

In previous studies on packed column flooding, only the global liquid holdup has been measured between the packed column liquid inlet and outlet [80]. However, measurement of global liquid holdup by draining the packed column is unrealistic for CCS applications.

2.4.3 X-ray tomographic techniques

X-ray tomography is a "hard field" tomographic technology, which has the advantages of high spatial resolution and high temporal resolution [84]. Radiation-based tomographic techniques can image the cross sections of the packed column at different axial positions [85], providing information on liquid holdup, and hydrodynamic liquid spreading patterns of rotating packed beds [86, 87], bubbling fluidized beds [88] and

counter-current flow distillation columns [85]. Janzen et al. [89] used X-ray tomography to investigate liquid holdup, liquid distribution and hydrodynamics in structured packing under flooding conditions. Furthermore, Janzen et al. [90] applied ultrafast electron beam X-ray tomography to overcome the disadvantages of the slow sampling frequency of the conventional data acquisition system. Thus, the system with a high temporal resolution of 2,000 images per second could obtain the dynamic liquid holdup and the real-time liquid distributions. However, the shortcomings in X-ray tomography include radiation hazards and expensive equipment [91]. Therefore, X-ray tomographic techniques are difficult to use for a long time and on a large scale in an industrial environment.

2.4.4 Comparisons for packed column monitoring methods

Each of the previously listed packed column monitoring technologies has its own advantages and disadvantages. The application of these process variables into packed column monitoring depends on the compatibility with the present technology and packing material in industry. Table 2-1 shows the comparison of the above-mentioned methods for packed column diagnosis.

Table 2-1: Comparison of monitoring methods for packed column diagnosis.

Monitoring technology	Advantages	Challenges
Pressure drop	Simple, cheap, most mature technology.	Intrusive, limited information from points measurement. Require a full pressure drop curve to diagnose flooding.
Liquid holdup	Cheap, highly mature technology.	Interrupt operation process. Conventional draining methods are difficult to measure liquid holdup.
X-ray tomographic techniques	Non-invasive, high temporal resolution and spatial resolution.	Radiation hazards, expensive equipment, slow data acquisition
ECT	Non-radiative, non-invasive, fast, low-cost, high temporal resolution.	ECT will struggle to image systems that utilise a grounded metallic packing [14].

As a non-radiative, non-invasive, fast and low-cost tomographic modality, ECT can possibly be implemented directly to the process scale, and it may be possible to gain operational insights to operate packed columns closer to the flooding point safely [92]. Relative to the x-ray tomographic techniques introduced in the previous section, the non-linear effect is often referred to as the "soft-field effect" inherent in ECT systems. Subsequent sections will specify the principles and applications of ECT.

2.5 Fundamentals of electrical capacitance tomography

ECT is a tomographic technique focusing on detecting permittivity changes inside the sensing area [92], as shown in Figure 2-2. The measured capacitances are used to retrieve the cross-sectional permittivity distribution within the sensing area based on a pre-calculated sensitivity map. For the forward problem of ECT, the linearised model describing the relationship between normalized capacitance data C_{norm} and the normalised permittivity change g is given by:

$$C_{norm} = Sg \tag{2.6}$$

where S is the matrix giving a sensitivity map for each electrode pair. Therefore, the inverse problem of ECT is to calculate the relative permittivity distribution from the measured capacitances. An ECT sensor suffers a non-linear behaviour, particularly for high permittivity media such as water and a thick pipe wall. The problem of non-linear sensor behaviour is of a fundamental nature, with its roots in the equations governing the behaviour of the electrical field [93].

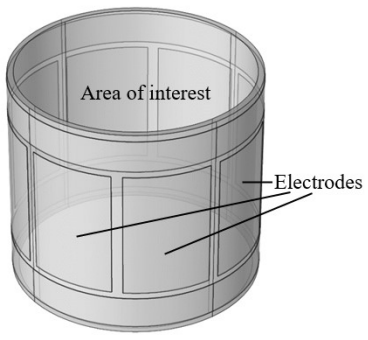

Figure 2-2: Simulated electrodes and area of interest.

Image reconstruction is the objective of solving the ECT inverse problem. But this process is ill-conditioned and inherently non-linear. For the problem of non-linearity, a change in such local coefficient produces a change in the underlying field solution that does not follow a linear relationship with coefficient. The accuracy of the final solution for the estimated permittivity distribution is determined by the degree of such non-linearity and the number of available independent capacitance measurements. The number of capacitance measurements is usually much smaller than the number of pixels to be determined so the image reconstruction process is also ill-conditioned. The ill-posed problem also affects how noise and small perturbations on the measured data influence the reconstructed image quality. Common image reconstruction algorithms can be referred to in Yang and Peng [94].

Although various normalising methods have been created and published in literatures, the parallel and series normalisation are most commonly used [95]. The parallel scheme assumes that the total capacitance between a pair of electrodes is the sum of many smaller banks of different dielectric regions running in parallel from electrode to electrode [92]. For the parallel normalisation, the intermediate pre-pixel normalised capacitance at each measured electrode pair under the condition of gas-liquid flow is given by:

$$C_{norm} = \frac{C_{mea(j)} - C_{l(j)}}{C_{h(j)} - C_{l(j)}}, j = 1,2, \dots, N \tag{2.7}$$

where j is index of the measurement, N the maximum number of measurements. $C_{mea(j)}$ is the measured capacitance at the j^{th} electrode pair. $C_{l(j)}$ and $C_{h(j)}$ are the reference capacitances at the j^{th} electrode pair when the sensing field is full of low permittivity media (air) and high permittivity media (water), respectively.

On the other hand, the series normalisation scheme assumes a series connection and performs normalisation by using the reciprocal of the capacitances. For the series normalisation scheme, the intermediate pre-pixel normalised capacitance at each measured electrode pair under the condition of gas-liquid flow is given by:

$$C_{norm} = \frac{\frac{1}{C_{mea(j)}} - \frac{1}{C_{l(j)}}}{\frac{1}{C_{h(j)}} - \frac{1}{C_{l(j)}}}, j = 1,2, \dots, N \tag{2.8}$$

Recent studies have shown that either the two-end or the single-end calibration methods can be used for normalising the measured capacitances [14]. For the two-end calibration method, the ECT sensor is calibrated between the lowest and the highest permittivity limits. However, it is less practical in industrial applications to do the calibration with high permittivity media as it requires the column cross section to be filled with water. For the single-end calibration method, only single reference media is needed [14]. The single-end normalisation model is expressed as:

$$C_{norm} = \frac{C_{mea(j)}}{C_{ref(j)}}, j = 1,2, \dots, N \tag{2.9}$$

where $C_{ref(j)}$ is the reference capacitance when the packed column is full of low permittivity media, i.e. air with packing. However, this reference capacitance is not constant. It is affected by the real experimental conditions such as wetting and pre-flooding of the packing.

Under a linear approximation, the relationship between permittivity distribution and the measured capacitance is expressed as:

$$\frac{C_{mea(j)}}{C_{ref(j)}} \approx \frac{\sum_{k=1}^{w} \varepsilon_{mea(k)} s_{j,k}(\varepsilon_{mea(k)})}{\sum_{k=1}^{w} \varepsilon_{ref(k)} s_{j,k}(\varepsilon_{ref(k)})} \tag{2.10}$$

where k is the pixel number of the sensitive field and w the maximum number of pixels. The measured and reference permittivity at the k^{th} pixel is represented by $\varepsilon_{mea(k)}$ and $\varepsilon_{ref(k)}$, respectively. The sensitivity matrix S can be calculated using the finite element method (FEM) in advance.

2.6 ECT system for packed column diagnostics

2.6.1 System architecture and principle of operation

Figure 2-3 shows a schematic view of ECT measurement system, which consists of sensors, control circuits, data acquisition, and a computer with image visualisation software. The ECT sensing problem corresponds to the reconstruction of the dielectric

distribution in an imaging domain from a set of capacitance measurements taken at the domain boundary, from between a set of electrodes placed around the domain.

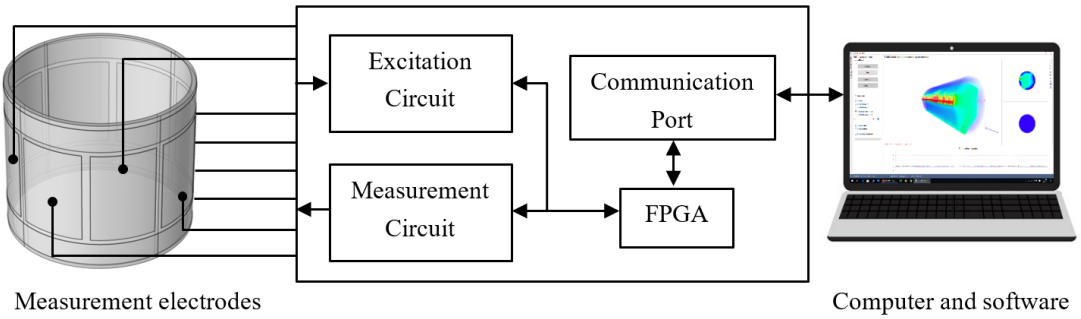

Figure 2-3: Diagram of ECT measurement system.

In an ECT system, the total number of available independent capacitance measurements M, measured using the n sensors, is given by equation (2.11).

$$M = \frac{n(n-1)}{2} \tag{2.11}$$

Each electrode produces a different electric field and imaging area. All capacitance measurements need to be normalised so that they can be used simultaneously for image reconstruction [92]. In this thesis, the development of a lab-scale ECT system will be demonstrated in Section 3.2.1.

2.6.2 Image reconstruction algorithms

In the previous sections, both the forward and inverse problems of ECT are introduced. Image reconstruction is the objective of solving the ECT inverse problem. To date, several studies have investigated image reconstruction algorithms for ECT [94, 96]. There are two main types of imaging reconstruction algorithms for ECT: algebraic and optimisation techniques [92]. The imaging domain is initially segmented into tiny pixels for this purpose. Then, the electric field is computed inside the imaging domain when one single electrode is excited with a unit potential while the others are grounded. The sensitivity matrix can be calculated with following equation:

$$S_{ij} = V_{0j} E_{si}(x, y, z) \cdot E_{di}(x, y, z) \tag{2.12}$$

where E_{si} is the electrical field distribution at the voxel j location given the source electrode in pair i is activated with unit voltage and other electrodes are grounded. Similarly, E_{di} is the electrical field distribution produced at voxel j location given the detector electrode of pair i activated with unit voltage and other electrodes are grounded. V_{0j} is the volume of voxel j. The linear relationship between the capacitance response to a perturbation on any given pixel permittivity is defined in equation (2.12). This is a rough estimation since it overlooks the non-linearity brought on by interactions between many pixel disturbances at various places [92]. This significantly influences the resultant electric field and thus the measured capacitance values. The first-order Born approximation in scattering theory is analogous to the approximation that the sensitivity matrix in equation (2.12) undergoes mathematically. The results produced by equation (2.12) can be accuracy if the contrast between the dielectric constants of different materials is not too high and the fractional volume of the perturbed pixel area is small [92].

1) Linear back projection

The first attempt to reconstruct images for ECT was made using linear back-projection (LPB) [97]. The sensor response to dielectric distribution can also be simplified as linear with respect to the sensitivity matrix. The solution obtained using LBP algorithm can be expressed as:

$$\hat{g} = S^T \lambda \tag{2.13}$$

where $\hat{g}$ is the pixel values, S^T is the transpose of the sensitivity matrix, and λ is the measured capacitance vector. The calculation solution of LBP is very fast, especially suitable for some applications that require real-time imaging [94]. But since it is a linear approximation, the reconstructed images are suffered from visible artefacts. Those artefacts are caused by the "soft-field" (non-linear) nature of the ECT problem.

2) Landweber algorithm

To reduce these artifacts to obtain improved images or high-precision quantitative information, iterative algebraic methods can be applied to solve the ECT problem. In those approaches, the initial pixel values can be calculated using a simple algorithm

images [98], e.g. LBP. The discrepancy between the original measured data and the forward solution is then minimised iteratively. This method significantly improves the reconstructed image quality. The Landweber algorithm is a variation of the steepest gradient descent method, which is the most common type of iterative algebraic reconstruction utilised in ECT [96]. This is defined in equations (2.14) and (2.15).

$$\hat{g}_{k+1} = \hat{g}_k - \alpha S^T (S_{\hat{g}k} - \lambda) \tag{2.14}$$

where a fixed relaxation factor α is set in the beginning of the iteration process [98], which is chosen base on the following constraint.

$$0 < \alpha < \frac{2}{\|S^T (S_{\hat{g}k} - \lambda)\|^2} \tag{2.15}$$

The image from the last iteration can be forward projected directly onto the sensitivity matrix. Since it utilises the same sensitivity matrix calculated in advance, this allows Landweber algorithm to iteration quickly. However, it is also limited by the linearisation error from representing the soft-field ECT problem using linear superposition of the sensitivity matrix [96]. The accuracy of iterative reconstruction approaches can be achieved by solving the forward problem using more accurate methods, e.g. FEM. However, this method needs to calculate the corresponding sensitive field in advance using the FEM. This makes iterative algorithms unsuitable for real-time imaging applications.

3) Deep leaning algorithms

With the rapid development of deep learning algorithms, data-driven ECT techniques have been validated for the optimisation of image reconstruction in many applications. Jin et al. [99] applied a deep learning-based method to accomplish image reconstruction from ECT.

Table 2-2: Comparison of the state-of-the-art image reconstruction algorithms for ECT.

Image reconstruction algorithms	Advantages	Challenges
LBP	Linear approximation could provide a fast solution. It can be used in fast data acquisition and real-time imaging applications.	Suffers from visible artefacts caused by the "soft-field" (non-linear) nature of the ECT problem.
Landweber algorithm	Iterative algebraic approaches could significantly improve image quality and mitigate the artefacts. The same sensitivity matrix calculated in advance could get results quickly.	The computational cost for the sensitivity matrix is significant and leads to slow data acquisition and offline imaging applications.
Deep learning algorithms	Features are automatically deduced. Process parameters, such as liquid holdup, can be obtained from the reconstructed images. Some mature networks can be directly applied to new ECT applications. Deep learning method is reliable when sufficient data and accurate data labels are available.	It may require a large amount of data to obtain good-quality images. The computational cost for training is expensive. Depending on the ECT application, selecting different parameters and training methods may be necessary.

Grzegorz et al. [100] used the long short-term memory network for intelligent selection of the best image reconstruction methods depending on the reconstructed case. There are a number of large cross-sectional studies which suggest a deep learning and regularisation-based hybrid algorithm further improves the ability to process a large amount of data in real time imaging [101-103]. In a recent study, Fabijańska and Banasiak [104] applied a graph convolutional network to improve 3D ECT images. This method improved the results of the best non-linear reconstruction algorithm. Compared with traditionally computational imaging algorithms, deep learning algorithms could take advantage of dealing with multiple input parameters and massive data. In addition to image reconstruction, some authors use ECT combined with deep learning for flow regime identification [105].

The previously discussed ECT imaging algorithms have different advantages and disadvantages. Applying these ECT image reconstruction algorithms to other CCS

applications depends on the compatibility with the needs in industry. Table 2-2 shows the comparison of the state-of-the-art image reconstruction algorithms for ECT.

2.6.3 Liquid holdup estimation

Studies have shown that either the ECT quantitative permittivity image reconstruction algorithm or ECT quantification of water to liquid ratio (WLR) methods can be used for liquid holdup estimation [106]. Li et al. [107] used the LBP algorithm to quantitatively derive the WLR and the thickness of the liquid layer of the annular flows. The liquid holdup calculation procedures are shown below.

$$C_n = \frac{\frac{1}{C_m(\varepsilon_m)} - \frac{1}{C_l(\varepsilon_l)}}{\frac{1}{C_h(\varepsilon_h)} - \frac{1}{C_l(\varepsilon_l)}} \tag{2.16}$$

where C_n is the normalised, capacitance. C_m is the measured raw capacitance, and C_l and C_h are the low-permittivity and high-permittivity calibration capacitances, respectively. The mixture permittivity model is derived from Ramu-Rao's model and proposed by Li et al. [7] to achieve a physics-based quantification of water liquid ratio from the raw capacitance measurements.

$$\varepsilon_m = \frac{1}{C_n(\frac{1}{\varepsilon_h} - \frac{1}{\varepsilon_l}) + \frac{1}{\varepsilon_l}} \tag{2.17}$$

where ε_m is the mixture permittivity, ε_h is the permittivity of water in this study, and ε_l is the permittivity of gas. The quantitative permittivity images are given by quantitative permittivity image reconstruction algorithm (LBP or iterative algorithms).

$$\hat{\varepsilon}(x,y) = \frac{\sum_{i=1}^{N-1}\sum_{j=i+1}^{N}(\varepsilon_m)_{ij}S_{ij(x,y)}}{\sum_{i=1}^{N-1}\sum_{j=i+1}^{N}S_{ij(x,y)}} \tag{2.18}$$

The image reconstruction algorithms are also used to generate images for real-time liquid distribution monitoring. Then, the quantitative permittivity images could be applied in oil-water dielectric mixing model for WLR calculations.

$$WLR = \frac{\varepsilon_{liquid} - \varepsilon_{oil}}{\varepsilon_{liquid} + 2\varepsilon_{oil}} \tag{2.19}$$

For a gas/oil/water three phase flow, the liquid holdup calculation is given by the gas-liquid dielectric mixing model.

$$\alpha_{liquid} = \left(\frac{\varepsilon_m - \varepsilon_{gas}}{\varepsilon_{liquid} - \varepsilon_{gas}}\right)^{\frac{1}{x}} \tag{2.20}$$

where α_{liquid} is the water liquid ratio, ε_{gas} the permittivity of air, ε_{liquid} the permittivity of water, and x is a measurement path-dependent empirical parameter. However, the image reconstruction process could suppress quite a good amount of information from the capacitance data and can be directly used to calculate the liquid holdup. The liquid holdup could be estimated without the reconstructed image [107] as illustrated in Figure 2-4. This model has been used in previous literature as a simple method for liquid in mixture ratio calculations. Examples include Wu et al. [1], Li et al. [107], Wang et al. [108] and Xie [109].

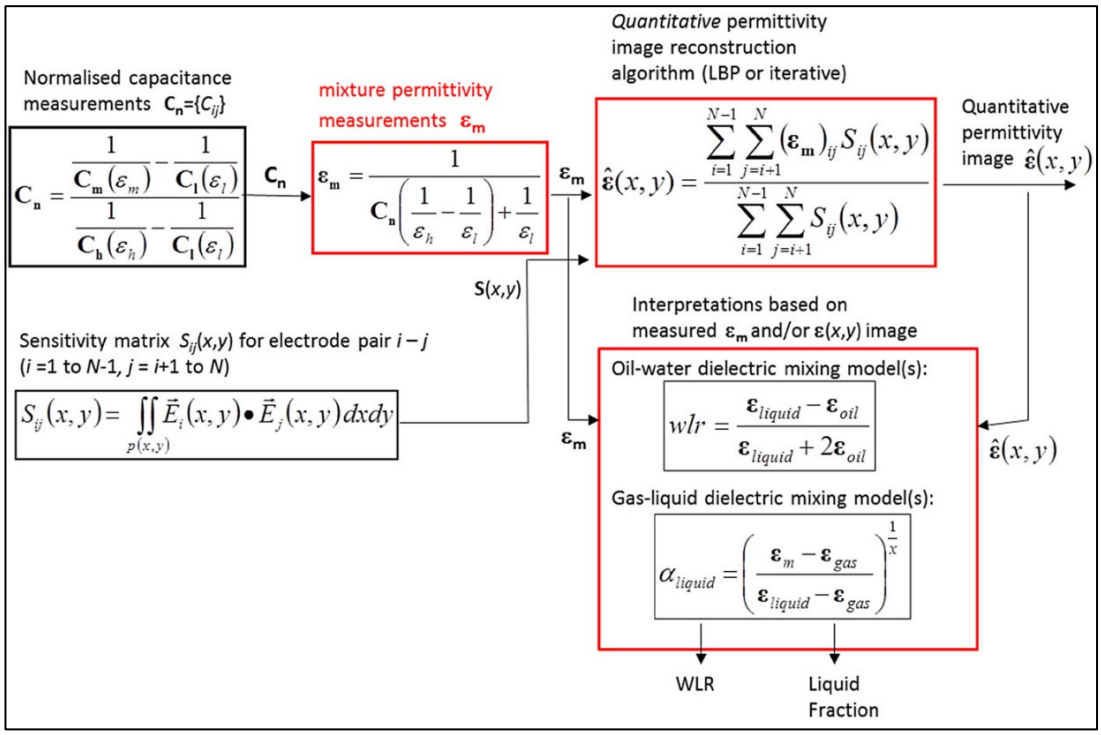

Figure 2-4: Calculation of liquid holdup based on image reconstruction method and the proposed new method. Reprinted with permission [107].

2.7 Electrical capacitance tomography applications

Commonly applied in multiphase flow measurement, process tomography has evolved significantly over the past decades. As a non-radiative, non-invasive, fast and low-cost tomographic modality, the application of ECT has been initialised to study the multiphase flow regime [110, 111]. ECT was employed previously by Wongkia et al. [112] to research the flooding capacity of counter-current gas-liquid flow in inclined packed beds equipped with small packings. Similarly, ECT was used to investigate pulse flow and pulse velocity in co-current trickle bed reactors [12], solid-phase distributions in a gas-solid fluidised bed [13, 15] and determination of the onset of bubbling and slugging in a fluidised bed [113]. Strazza et al. [114] used a simple two-electrode capacitance sensor for liquid holdup measurement in core-annular flows. However, the two-electrode sensor can only obtain one independent capacitance measurement without any spatial information about the target flow.

Various recent studies have shown that an ECT system can measure the liquid flow distribution and thus obtain the velocity measurement of two-phase flows [115, 116]. Several studies have used ECT to better understand the hydrodynamics of co-current flow in packed columns [117], dynamic liquid distribution in a fixed bed column [118] and monitor gas voids in a packed bed column [119].

Although ECT has been successfully used to measure liquid holdup and distribution in the packed column [11, 14, 117], imaging of liquid distribution has been barely studied under the flooding phenomenon or imaging frost formation process at the cryogenic packed column that enables timely warning of the occurrence of flooding or indicates the frosting of CO_2. This is also a motivation of this study.

2.8 Conclusions

This chapter provides background information necessary to understand the fundamentals of multi-disciplinary topics in this work. To achieve the goal of carbon neutrality, carbon capture and storage is an indispensable technology. Among the carbon capture technologies being studied, post-combustion capture has the potential

to be applied on a large scale because it can be retrofitted to existing power plants. The purpose of the chapter is to help understand the state-of-the-art carbon capture techniques and ECT techniques. While the impact of flooding involved in amine-based CO_2 capture and extremely low temperatures involved in cryogenic carbon capture on an ECT sensor is unknown. The diagnostic capabilities of ECT for packed columns are well established [14]. Even though the literature contains references to many of the individual basics, no attempt has been made to apply ECT to detect flooding or frosting and combine them into a unified technique. Subsequent chapters will describe the innovative work and scientific contributions made in the study.

Chapter 3 ECT for flooding monitoring

3.1 Introduction

The literature review shows a significant research gap in the diagnosis of packed beds in post-combustion CO_2 capture. Ultimate increasing the gas flow rate to increase the efficiency of CO_2 capture can lead to liquid accumulation and even full flooding in vertical packed columns. This reduces the mass transfer efficiency of the packed column and results in a larger pressure drop. Pressure drop measurement is the most established technique for predicting floods. However, they provide limited information for packed columns and do not meet the information required to develop high-performance packed columns with new solvents or operate the reaction process flexibly [7]. Therefore, it is timely to investigate the flooding process since it could potentially have useful applications in mass transfer processes for CO_2 capture. This chapter aims to develop an ECT-based flooding monitoring technology and quantify the differences between the conventional packed column flooding monitoring methods in the literature and the novel ECT method proposed by this work.

3.2 Methods

3.2.1 System design

The methodology used in this work has been fully characterized by Wu et al. [14], which investigated the effectiveness of the equipment and accuracy of the liquid holdup calculation. They also found that the ECT could measure the liquid distribution and calculate the liquid holdup inside the packed column with a liquid holdup up to 13%. With a flooded packed column, the performance of ECT is not precise because near the flooding point, water, as the dominant phase, may affect the accuracy of the measurement.

A schematic diagram of the ECT system with packing [17] is shown in Figure 3-1. Eight 100 mm long electrodes are mounted outside the packed column and surrounded by two grounded guard electrodes. The excitation signal is a sinusoidal wave voltage

with 14 Vp-p and 200 kHz frequency. In between the electrodes and the computer is a data acquisition system which is a control circuit that allows all acquired signals to be conditioned by the C/V circuit [120] and transmitted to the computer through USB 2.0. The data acquisition device of ECT is connected to the computer, and the image is reconstructed through Visual Multiphase Flow software to realize real-time liquid distribution imaging. The frame rate of the ECT system is 714 frames per second. The maximum signal-to-noise ratio (SNR) is 76.73 dB, and the minimum SNR is 62.25 dB.

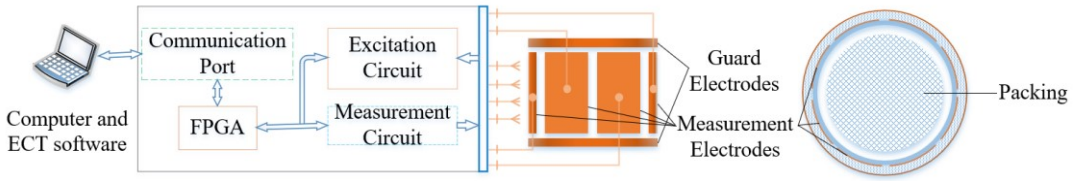

Figure 3-1: Schematic diagram of the ECT system with packing.

3.2.2 Simulation of flooding in packed column using ECT

To investigate the feasibility of ECT in imaging the liquid phase distribution in a packed column at flooding state, a 3D geometric model with Sulzer Mellapak 250Y packing is established in COMSOL Multiphysics software. Figure 3-2 shows the photos of Sulzer Mellapak 250Y packing being simulated in the models. To be consistent with the experimental setup, the packing material used in the simulation was also chosen to be plastic. The relative permittivities of the plastic, air and water used in the simulation are; $\varepsilon_{plastic}$=2, ε_{air}=1, and ε_{water}=78, respectively.

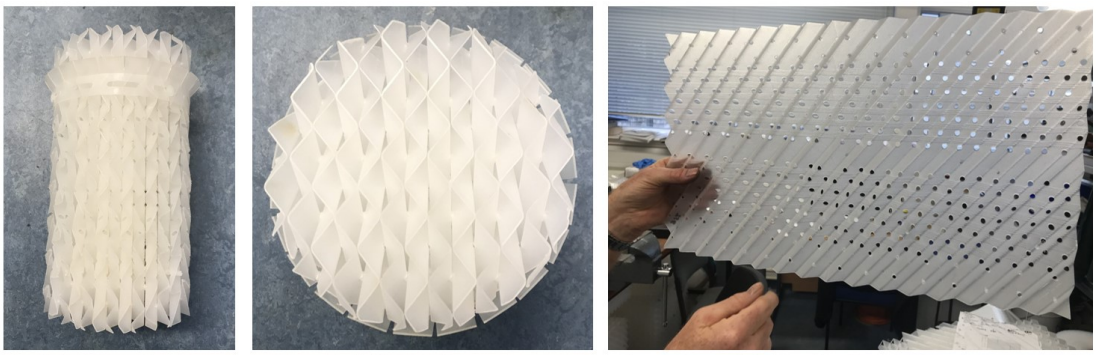

(a) front view (b) top view (c) single sheet view

Figure 3-2: Photos of Mellapak 250Y packing.

A flow diagram for the simulation process is shown in Figure 3-3. Since the distribution of the liquid in the packed column is very complex, the liquid was simplified as a simple sphere. A packed column contains 129 dispersed liquid droplets with a diameter of 8 mm, and the air fills the void space between the droplets, as shown in Figure 3-3 (a). Figure 3-3 (b) shows the setup of the ECT sensor with 8 electrodes and 2 guard electrodes around a plastic pipe [121]. The height of each electrode is 100 mm, and the length is 70.4 mm. The 8 electrodes are evenly distributed on the pipe surface with a gap of 8.5 mm. The basic ECT measurement strategy [10] was adopted in simulation to obtain the boundary capacitance data. Using this strategy, a completed data frame is composed of 28 independent measurements. Furthermore, Figure 3-3 (b) shows the pipe and ECT were covered with a shield electrode. A total of 6-layer droplets were added to the packing, as shown in Figure 3-3 (c). Figure 3-3 (d) shows the FEM mesh of the simulation model for forward problem calculation. The mesh was solved using COMSOL integrated solver. The sensitivity matrix was calculated by using the combination of COMSOL Multiphysics and MATLAB based on the created 1:1 sensor model as shown in Figure 3-3 (d).

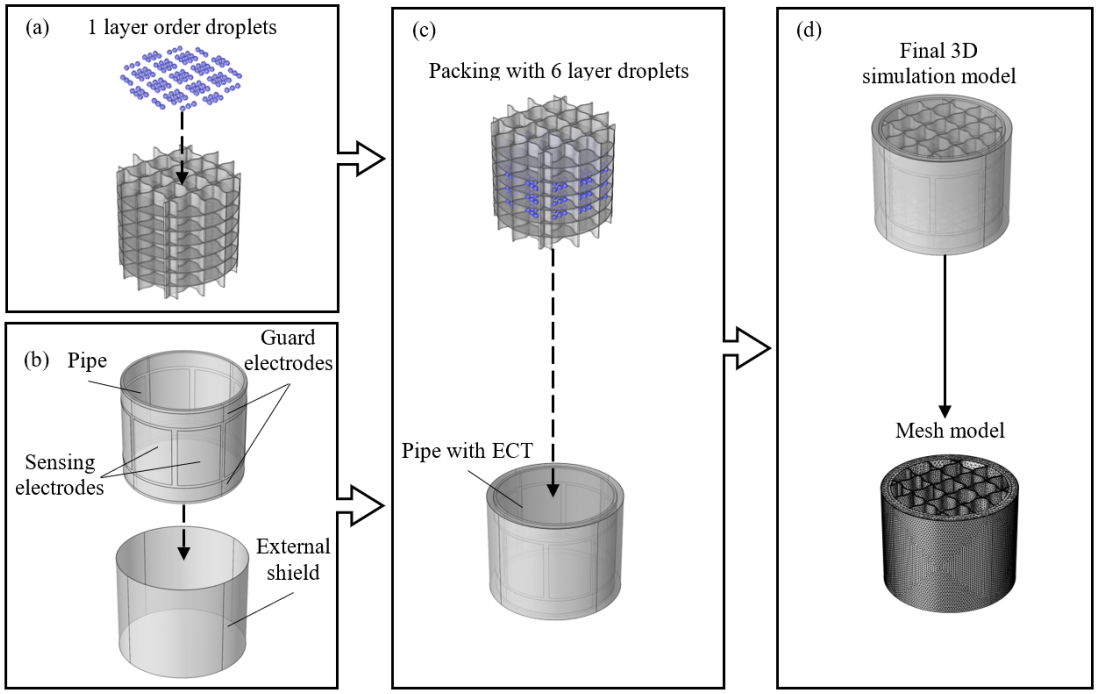

Figure 3-3: 3D schematic diagram of (a) 129 liquid droplets and simplified packing model, (b) pipe with ECT, (c) combination of packing model with droplets and ECT, (d) the final 3D simulation model and a mesh model for inverse problem calculation.

The purpose of the simulation is to determine the feasibility of liquid distribution imaging in packed columns with the liquid holdup higher than those in the previous study [14]. The permittivity of each droplet can be switched between liquid and gas through COMSOL to simulate high liquid holdup during flooding [122]. To monitor the flooding phenomenon of the packed column, the difference between the liquid distribution images was evaluated by quantitatively adjusting the overall liquid holdup. The static liquid holdup is calculated by the proportion of the liquid retained in the void spaces and the total pipe volume [123].

3.2.3 Experimental setup and campaign

When the simulation is completed, a counter-current flow packed column is built to monitor flooding with the ECT sensor, which is a 1130 mm height vertical column made out of polytetrafluoroethylene (PTFE), inside diameter (ID) of 190 mm, and outer diameter (OD) of 200 mm. The column is filled with four sections of structured packing Mellapak 250.Y manufactured by Sulzer Chemtech Ltd, as shown in Figure 3-4. The diameter of packing is 180 mm with the heights of packing as 315.0 mm, 157.5 mm, 157.5 mm and 315 mm from top to bottom, respectively. The void fraction of the selected packing material is about 88%. The packing geometry is characterized by an inclination angle of the flow channels with a horizontal direction of 45°. The packing elements, made of plastic, were alternately rotated around the axis of the column by 90° relative to each other to enable uniform liquid distribution. The schematic of the lab-scale experimental set-up for the flooding experiments is shown in Figure 3-4.

The column is operated in a counter-current flow configuration with liquid entering at the top of the column using a liquid distributor and the air entering at the bottom using a gas distributor. The liquid distributor used for liquid feeding has a diameter of 90 mm, and orifices of 4 mm in diameter. Liquid flow is controlled with an adjustable bypass valve with the liquid loads ranging from 13.4 to 38.9 $m^3/(m^2h)$ and monitored with an electromagnetic flowmeter (OMEGA, FMG71B-A-BSP, with an accuracy of $\pm$2.0%). Two blowers (Windjammer, 119153) introduce air into the column from the

bottom. In the experiments, the air volumetric flow rate was increased from 0.0104 to 0.0226 m^3/s in small increments. Liquid distributions were imaged via the ECT sensor at various longitudinal positions illustrated in the orange zones of Figure 3-4. The different locations of the measurements were chosen to examine the liquid distribution along with the column height. Two pressure transducers record the pressure at the top and bottom of the column, as shown in Figure 3-4.

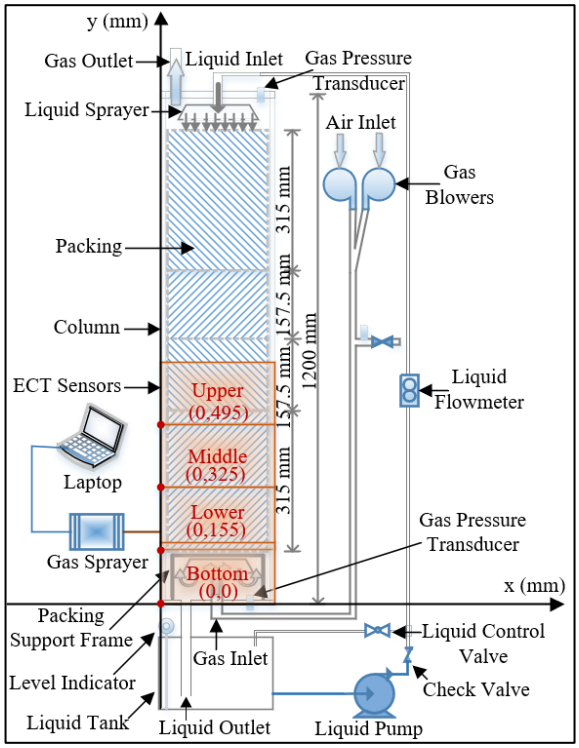

Figure 3-4: Schematic diagram of the experimental rig with ECT sensors.

The reference capacitances (C_l and C_F) were measured first. As mentioned above, C_l is the capacitance when the column is filled with plastic structured packing and stagnant air, as shown in Figure 3-5 (a). C_F is the capacitance when the packed column is filled with water, as shown in Figure 3-5 (b). The liquid flow rate was set at a constant value, while the gas flow rate was adjusted to the desired value. The real status of the column was photographed, and ECT images of the column were reconstructed. The gas flow rates were increased in the smallest increments of air volumetric flow rate until the column was flooded. At each gas flow rate, calibration measurement for ECT was firstly taken. Then, ECT data at each gas flow rate were collected for a period of 20 seconds and averaged for offline data analysis. Meanwhile, pressures at the top and bottom of the column are measured simultaneously.

Procedures of simultaneous measurements of pressure drop and ECT images were similar except that the ECT measurement at each flow condition was obtained from an independent run using two different calibration methods. In another normalisation method, as shown in Figure 3-5 (c), capacitance in flooding condition C_f is used as high permittivity limit to replace C_F. To avoid inaccuracy of capacitance reference, C_f is the average of 20 s measurement, rather than a single measurement, so that the variation of the normalised capacitance C_{norm} could be restricted.

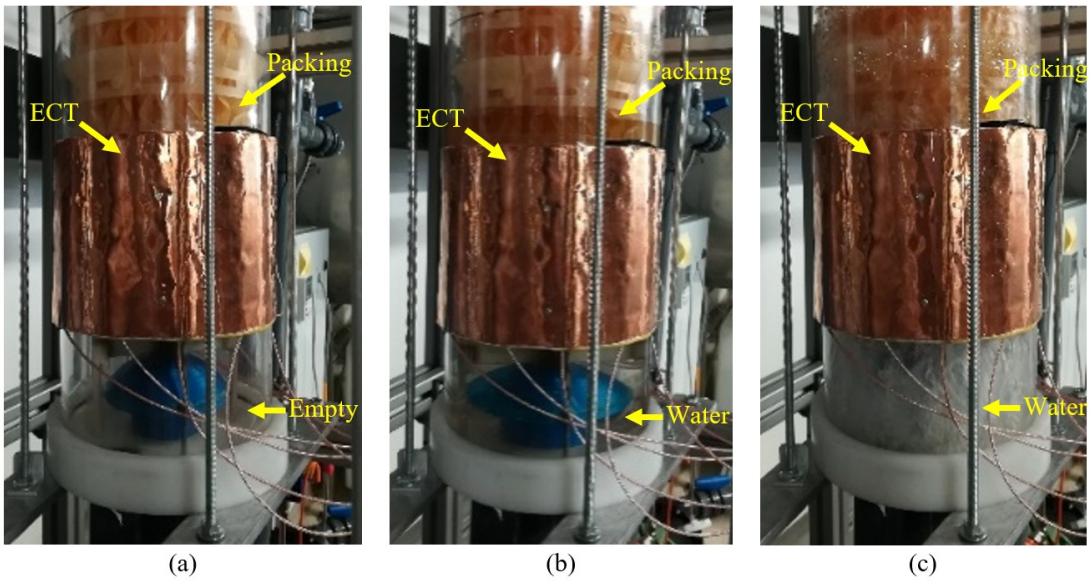

Figure 3-5: Photograph of the packing at different operating conditions: (a) empty, (b) submerged in water and (c) onset of flooding.

3.2.4 Development of flooding index theory

Liquid distribution, liquid holdup and packing efficiency are significantly affected by different operation regime in the structured packing column. There are three main operation regimes, i.e. pre-loading regime, loading regime and flooding regime [124]. P_f is used here to refer to the degree of local flooding or the local maximum liquid capacity of the packed column. The liquid entrainment may become excessive if P_f at a certain point is too high. The real-time liquid distributions were imaged at various longitudinal positions using the LBP algorithm [94] based on C_{norm}. To evaluate the stage of flooding quantitatively, the P_f is formulated in equation (3.1), where $G_{(j)}$ is the value of normalized permittivity at the j^{th} pixel and M is the total number of the pixels

of a reconstructed image. M is 3228 in this work. P_f represents the degree of a state approaching local flooding.

$$P_f = \frac{\sum_{j=1}^{M} G_{(j)}}{M} \tag{3.1}$$

In addition to pressure drop, P_f and ECT images of liquid distribution are able to quantitatively and qualitatively indicate the developing process of flooding in the packed column. The degree of local flooding and P_f are simplified as a linear relationship.

3.3 Results

3.3.1 Results from numerical simulation for the packed column flooding

The feasibility of monitoring the flooding phenomenon in a packed column with ECT was firstly validated by simulation. Figure 3-6 shows the image reconstruction of the packed column over a range of 0 to 750 liquid droplets. Water has a much larger permittivity than that of the plastic packing and the air. The permittivity is gradually increased when a larger number of liquid droplets are involved. The colour bar shown in Figure 3-6 is set for comparing the difference between the reconstructed images before and after the occurrence of flooding. The results suggest that the liquid is distributed in a 160 mm diameter circle in the centre of the packing. The maximum permittivity value is 0.1 when 750 droplets are added inside the packing. The minimum permittivity value is 0 when no droplet exists. Within the range of 0 to 750, the permittivity of the packing with droplets is increasing from 0 (0 droplets) to 0.1 (750 droplets), which can be clearly indicated by the reconstructed images before the occurrence of flooding. All these results demonstrate that ECT can accurately measure liquid holdup and can be used to diagnose the flooding phenomenon in packed columns.

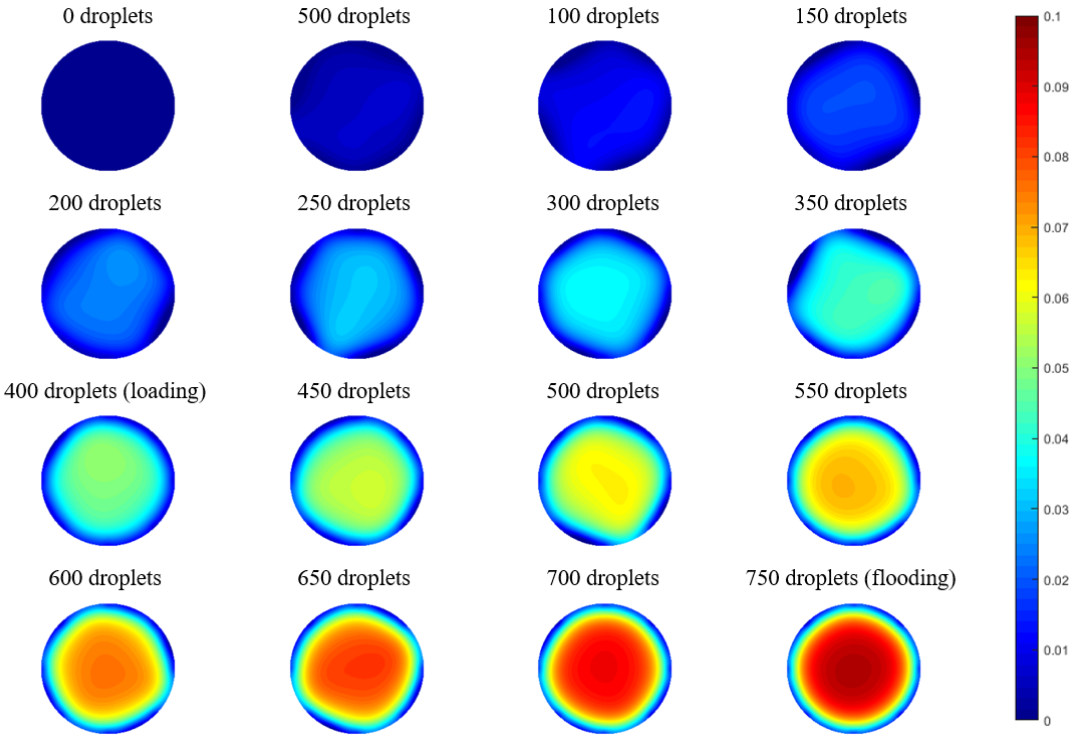

Figure 3-6: Reconstruction images of the packed column at a range of water droplets (from 0 to 750).

3.3.2 Results from experiment of counter-current packed column

The operating regions of a packed column can be identified, in principle, via visual inspection of a transparent column. The majority of industrial columns are, however, non-transparent. Monitoring pressure drop along the column is the conventional way of monitoring loading and flooding. Pressure drop in the packed column can be estimated using the empirical models [79, 125]. In these experiments, the liquid rate remained at 38.9 $m^3/(m^2\ h)$. Pressure drop is plotted in Figure 3-7 against an increasing volumetric flow rate for air from Q=0.0104 m^3/s to Q=0.0219 m^3/s. As illustrated in Figure 3-7, it is difficult to directly identify the loading point on the discrete pressure-drop points and the regression curve. The gradient rapidly increases from Q=0.0196 m^3/s, which indicates the loading point of the packed column. After the loading point is reached, liquid starts to accumulate at the bottom of the column. The operation of the packed column changes from the loading regime to flooding regime. The continuous increase of gas flow rates causes higher liquid holdup, which in turn causes a higher pressure drop and liquid starts bypassing the packing bed [69].

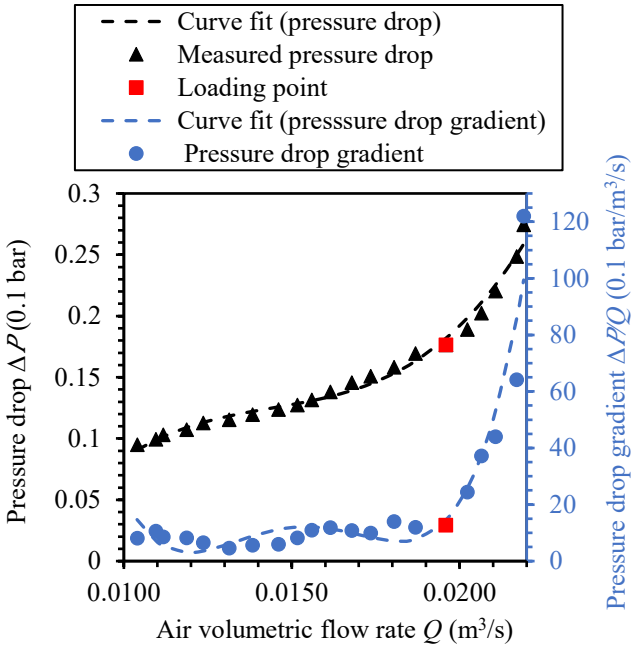

Figure 3-7: Pressure drop and gradient of pressure drop across the packed column for varying volumetric flow rates for air.

The flow regimes in the counter-current packed column are photographed, while ECT images are reconstructed over the column cross-section for the bottom position without packing and the lower position with structured packing. The ECT sensor was removed for visual observation in the structured packing area. In these experiments, the high capacitance reference was taken from the column filled with water, in order to monitor the transition process of gas-liquid distribution from pre-loading regime to flooding regime. Table 3-1 presents the measured liquid distributions at various volumetric flow rates for air from 0.0138 m^3/s to 0.0217 m^3/s. Red areas in the images represent higher liquid holdup, while the blue areas represent lower liquid holdup. ECT images are analysed separately in terms of the bottom and lower sections of the column.

Initially, a smooth falling liquid film could be seen when the volumetric flow rate for air is lower than 0.0162 m^3/s. Hydrodynamic instability corresponds to a transition from pre-loading regime to the loading regime, which associates with a significant increase of liquid holdup [126]. In the pre-loading regime with volumetric flow rate from 0.0138 m^3/s to 0.0162 m^3/s, the ECT images of the bottom section show that the liquid holdup and distribution patterns are stable. The liquid is uniformly distributed around the inner area of the column, and liquid holdup at the inner area is slightly

higher than that of the peripheral area. With the increase of volumetric flow rate for air from Q=0.0162 m^3/s onwards, visual observations during the experiments also confirm that there are droplets entrainment and flow reversal occurs in the packed column. Red patches and a red ring appear on the boundaries of the ECT images, indicating liquid is accumulated with a larger extent near the wall of the column than that in the centre of the column. Another possible explanation for this is that the fringe effect of electrical capacitance, i.e. the electric field distribution depends on the material distribution, and the electric field spreads to a large volume at both ends of an ECT sensor [127]. This field distortion at end of electrodes is referred to as the fringe effect. Therefore, the red circle area close to the electrode will be more sensitive to the liquid.

Table 3-1: Photos of the column and the reconstructed ECT images across the packed column for varying volumetric flow rates for air.

Air volumetric flow rate Q (m^3/s)	**0.0138**	**0.0146**	**0.0152**	**0.0156**	**0.0162**	**0.0168**	**0.0173**
Countercurrent flow							
Reconstructed Images (Lower)	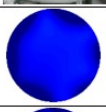	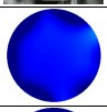	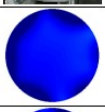	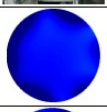	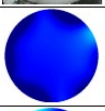	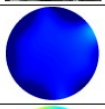	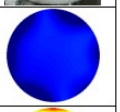
Reconstructed Images (Bottom)		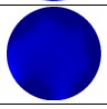		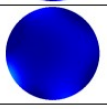	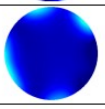	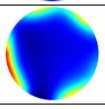	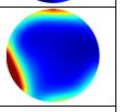
Air volumetric flow rate Q (m^3/s)	**0.0180**	**0.0187**	**0.0196**	**0.0202**	**0.0206**	**0.0211**	**0.0217**
Countercurrent flow							
Reconstructed Images (Lower)	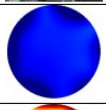	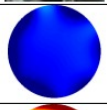	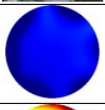	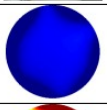	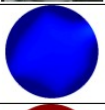	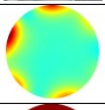	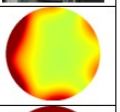
Reconstructed Images (Bottom)	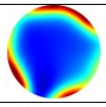	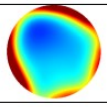	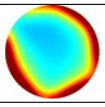	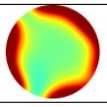	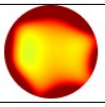	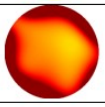	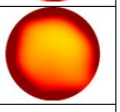
Colour map	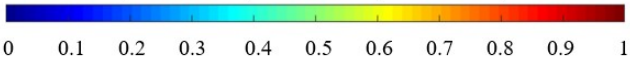 0 0.1 0.2 0.3 0.4 0.5 0.6 0.7 0.8 0.9 1						

Structured packing in the lower section prolongs residence time of the liquid phase. Therefore, volumetric flow rate for air up to Q=0.0162 m^3/s, the liquid holdup in the

lower section is higher than that in the bottom section. After the loading point is passed, the liquid flow across the lower section remains evenly distributed, namely, more liquid is homogeneously distributed in the packing area. Less liquid is distributed around the gap between packing and the column wall than that in the middle of the section. It implies that gas-liquid mass transfer will take place in the centre of the packing rather than the void space between the packing and column wall. A sudden transfer from the loading regime to flooding regime takes place from Q=0.0206 m^3/s to Q=0.0211 m^3/s. Excessive liquid accumulation occurs near the wall of the column. Since the liquid bypasses structured packing, the liquid holdup in the peripheral area is higher at Q=0.0217 m^3/s. By now, the gas kinetic energy is sufficiently high to destabilise the liquid film and reverse the liquid flow, leading to column flooding. These results demonstrate the advantage of using ECT over a conventional pressure drop method, as ECT can provide detailed spatial information at different stages of the flow regime in the packed column.

Monitoring flooding with ECT allows for a spatial determination of liquid distribution compared to a reference state. The flooding index P_f is introduced and determined in equation (3.1) to represent the degree of local flooding. P_f =1 implies that the cross section of packing has reached a state of liquid accumulation corresponding to flooding. In these experiments, the high capacitance reference was taken when the column was flooded. Reconstructed images and the corresponding P_f are shown in Table 3-2. Reconstructed images illustrate the liquid distribution at different column heights against volumetric flow rate for air. As volumetric flow rate increases, ECT images at the lower, middle and upper locations display the same transition before and after local flooding. For each section of packing, the structured packing holds liquid preferentially towards the centre of the column, before flooding occurs. When the volumetric flow rate reaches certain values, i.e. 0.0224 m^3/s, 0.0219 m^3/s, and 0.0211 m^3/s for the upper, middle and lower sections, respectively, the column is flooded quickly. As expected, local flooding starts first in the lower section of packing, then propagates to the middle and upper locations. Under this set of experiments, it is most beneficial for the ECT sensor to be installed at the bottom position if the loading point needs to be identified early. If the flooding point needs to be identified, the ECT sensor should be installed at the top position of the column. Although tomographic images

have relatively low spatial resolution, they are still able to indicate liquid distribution in the packed column, which is valuable for the opaque reaction columns.

Table 3-2: Reconstructed images corresponding to different sections of packed column for varying volumetric flow rates for air.

	Air volumetric flow rate Q (m^3/s)	0.0187	0.0196	0.0202	0.0206	0.0211	0.0217	0.0219	0.0224	0.0226
Upper	Reconstructed images	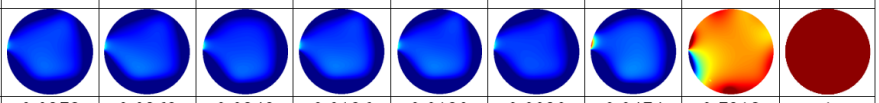								
	Flooding index P_f	0.0278	0.0269	0.0249	0.0196	0.0120	0.0020	0.0474	0.7318	1
Middle	Reconstructed images	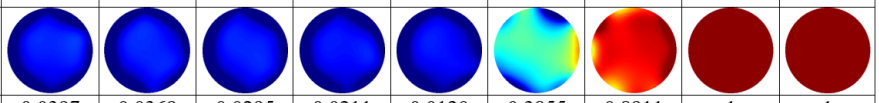								
	Flooding index P_f	0.0397	0.0369	0.0295	0.0211	0.0120	0.3855	0.8911	1	1
Lower	Reconstructed images	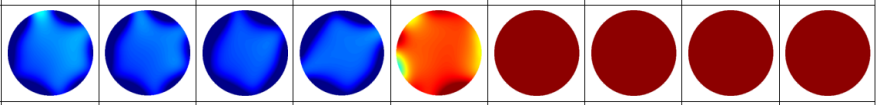								
	Flooding index P_f	0.1626	0.1316	0.0814	0.1104	0.8095	1	1	1	1
Colour map		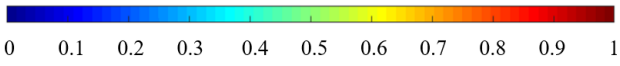								

The calculated P_f values were compared with the measured pressure drop. Figure 3-8 shows the influence of gas velocity on the P_f at the bottom of the column and pressure drop gradient. Error bars are derived based on the maximum and minimum value of measurements. It can be observed that the P_f at the column bottom starts to increase from Q=0.0152 m^3/s, while the pressure drop gradient has an obvious increase after 0.0196 m^3/s air volumetric flow rate. It is worth noting that the pressure drop describes the change of pressure across the column, while the ECT monitors the flooding index locally in the bottom section of the column. These results indicate that P_f obtained using ECT can provide more sensitive and accurate information for an early prognosis of flooding. It is also possible to detect flooding locally, and, by extension, increase confidence in operating with gas velocities closer to the column flooding velocity.

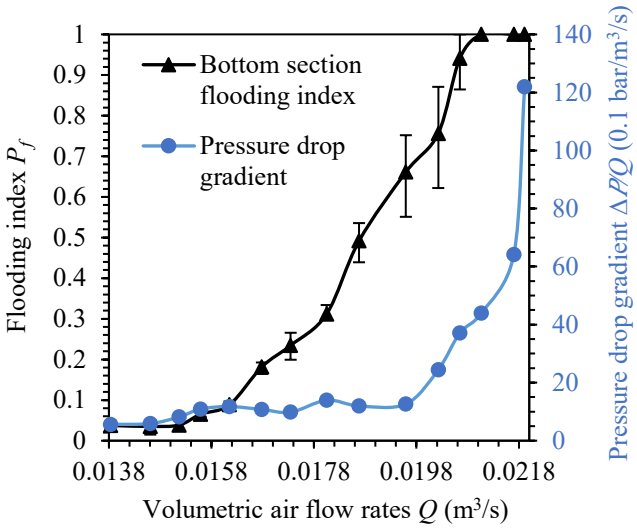

Figure 3-8: Comparison between flooding index P_f at the bottom section and pressure drop gradient across the whole packed column.

Figure 3-9 illustrates the influence of the volumetric flow rate for air to P_f at lower, middle and upper sections of the column. Three P_f curves of lower, middle and upper position have a similar developing trend. As the column is sequentially flooded across the lower section, the middle position and the upper position, three P_f curves reach the top sequentially. During this flooding process, the pressure drop against the volumetric flow rate is plotted in Figure 3-9 for clarity. There is no apparent inflection point on the pressure drop curve. In contrast, P_f extracted from ECT image can quantitatively indicate a degree of local flooding and reveal a sudden appearance of local flooding, for example, P_f=0.11 at Q=0.0206 m^3/s in the lower position. The transition of flooding took place rapidly and intensively between Q=0.0206 m^3/s to Q=0.0217 m^3/s. Large P_f variation at Q=0.0211 m^3/s reflects severe flow turbulence, which can be visually observed in the photos in Table 3-1. The same phenomenon is demonstrated on the curves of the middle and upper sections.

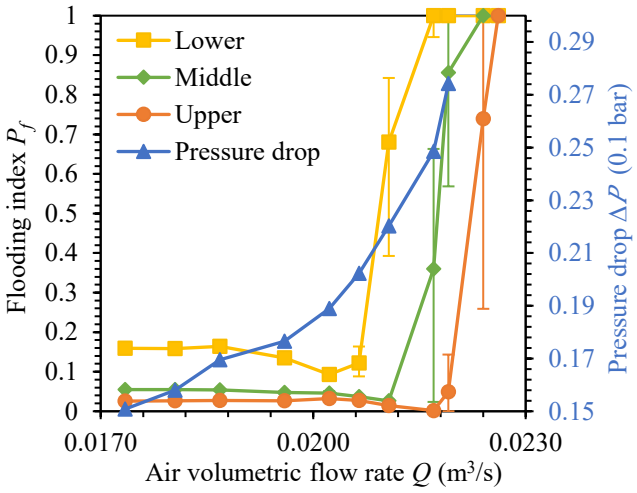

Figure 3-9: Comparison between flooding index P_f of different packing sections and pressure drop across the whole packed column.

The standard deviation of flooding index in Figure 3-8 and Figure 3-9 is caused by turbulent flow itself. High imaging rate of ECT, i.e. 714 frames per second, enables a fast snapshot of one individual cross-sectional image to truly reflect the nature of turbulent flow in the flooding process. It is worth mentioning another phenomenon. P_f always goes down first before flooding occurs, which indicates that the liquid holdup decreases then increases suddenly towards flooding. Taking the lower section as an example, the P_f drops from 0.16 to 0.09, then rises to 1.0. This phenomenon is consistent with results obtained in previous studies [128]. This phenomenon was repeatedly captured at all three sections. These results suggest that the use of P_f obtained using ECT can provide new insights into column operation for the early prognosis of local flooding compared to the traditional pressure drop method.

3.4 Conclusions

In this chapter, the details of the ECT system for diagnosis of packed column are presented. Simulations for the packed column from the loading point to the flooding point are developed in COMSOL Multiphysics. The simulations show that the ECT system is able to reconstruct the liquid phase distribution in the packed column and analyze the fluid dynamic characteristics, e.g. loading point and flooding point of the packed column. Furthermore, experimental results demonstrate the effectiveness of

ECT as a powerful tool for studying hydrodynamics in the packed column, which can be used to diagnose the flooding phenomenon in post-combustion CO_2 capture applications. The flooding index inferred from real-time measurements is a quantitative method to evaluate the degree of local flooding. The experimental results demonstrate that flooding can be predicted using the flooding index curve. In addition, the importance of ECT installation location for flooding prevention is demonstrated. Because ECT is a non-intrusive, portable imaging method, it could be deployed at the bottom of the packed column for the earliest detection of flooding.

This project is the first comprehensive investigation of ECT for packed column flooding applications. However, the flooding index model is too biased and imprecise. Future work should develop a more accurate quantitative method for flooding diagnosis by using ECT. The following chapter will use Convolutional Neural Network (CNN) aided ECT to predict the phenomenon of flooding within the test rig.

Publications from this chapter:

- Z. Li, **Y. Chen**, Y. Yang, C. Liu, M. Lucquiaud, J. Jia, Flow regime transition in counter-current packed column monitored by ECT, Chemical engineering journal 420 (2021) 129841.

- **Y. Chen**, Z. Li, Y. Yang, J. Jia, C. Liu, M. Lucquiaud, Simulation of Flooding Phenomenon in Packed Column using Electrical Capacitance Tomography, 2019 IEEE International Conference on Imaging Systems and Techniques (IST), IEEE, 2019.

Chapter 4 CNN aided ECT for flooding prognostic in packed columns

4.1 Introduction

In chapter 3, the feasibility of liquid distribution and flooding monitoring using ECT was verified. This chapter investigates the feasibility of ECT and CNN as an intensified alternative to conventional flooding prediction methods. The unique local measurement feature of ECT allows variations in the predominant characteristics of the flooding phenomenon to be better investigated than the conventional methods. Combined with CNN, the ECT system enables high accuracy on liquid holdup calculations and strong robustness in turbulent flow measurements [129].

This chapter also provides comprehensive comparisons between the packed column monitoring methods collected in chapter 3 in this thesis and methods from the wider literature. The liquid holdup predicted according to the conventional Maxwell equation did not match the measured values at high gas flow rates, showing discrepancies of up to 68%. In contrast, CNN is much superior to the Maxwell equation method at high gas flow rates, giving only 1% mean of difference than the reference liquid holdup. ECT supported by CNN shows great fidelity for non-invasive monitoring of local liquid holdup, allowing for more accurate, localised prediction of loading point and flooding point in packed columns [129].

4.2 Methods

4.2.1 Simulation setup and campaign

A packed column has an advantage in the application of CO_2 capture, where complex, three-dimensional (3D) packing structures maximize the gas solvent's contract area and, therefore, maximizes reaction efficiency [34]. The study of packing hydraulics, liquid distribution and its effects on carbon capture efficiency makes real-time quantitative imaging ability essential, among which diagnosis of flooding and liquid

maldistribution monitoring in real-time are regarded as particularly helpful [14]. Recent work reported in [130] demonstrates ECT has great potential for such purposes.

This study uses ECT to investigate the hydrodynamic of counter-current flow and liquid distribution in a counter-current flow packed column. A CNN is designed to build the relationship between ECT measurements and liquid holdup. In order to verify the performance of the proposed CNN model, a preliminary test dataset is generated by FEM. Our previous study [5] shows that the simulation datasets with different levels of liquid holdup generated by FEM could be used to evaluate the effectiveness and performance of this method.

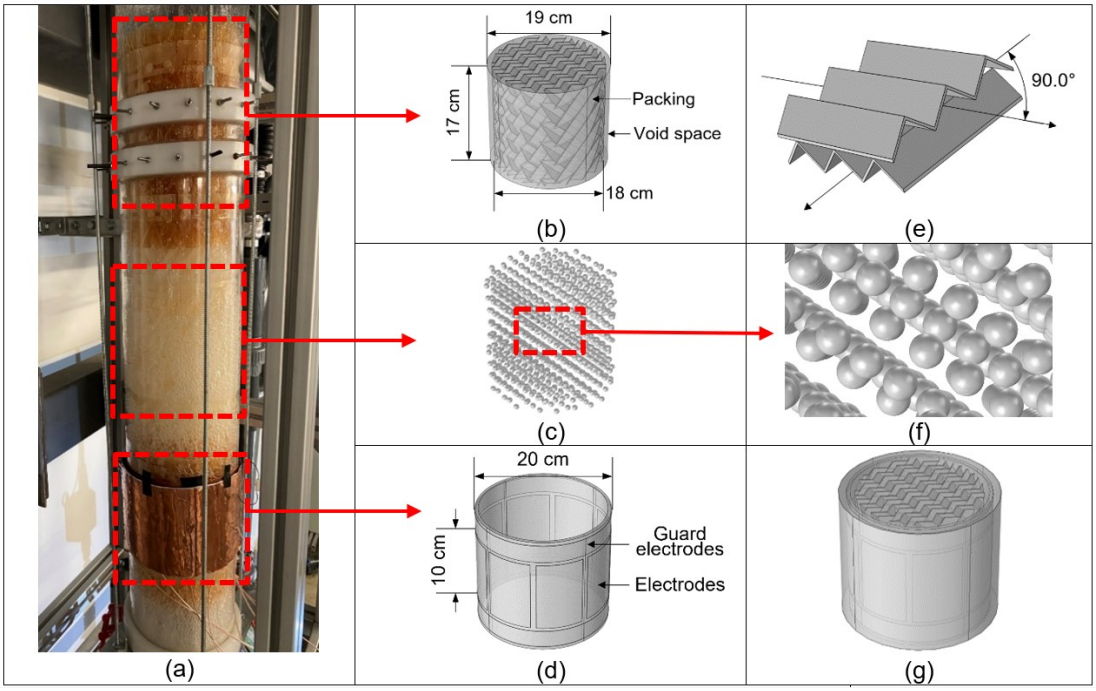

Figure 4-1: Simulation models of the packed bed shown from various perspectives: (a) a real packed bed; (b) a section of Mellapak 250.Y structured packing; (c) water droplets; (d) ECT sensor; (e) zoomed-in packing to show flow channel arrangement; (f) zoomed-in water droplets; and (g) final 3D simulation model.

In order to reveal the feasibility of predicting packed column liquid hold up, a selected number of liquid droplets were added into the packing to simulate variable levels of the liquid load. Figure 4-1 illustrates simulation models of a packed column with packing and an ECT sensor. In order to vary liquid holdup from 0% up to 17.8%, a maximum of 1323 droplets were added to the 3D packed column model. The diameter of each droplet is 4.5 mm. The real value of liquid holdup was calculated with the

number of droplets in the simulation, then compared with the predicted liquid holdup using CNN.

4.2.2 Experiment apparatus

The packed column test rig shown in Figure 4-2 is used to simulate a lab-scale counter-current absorption carbon capture application. The experimental rig is made of a transparent glass pipe to visually observe the flooding phenomenon in the column [65]. The packed column was built with an ID=190 mm, OD=200 mm, h=1130 mm. The packed column has been tested using polypropylene structured packings Mellapak 250.Y from Sulzer Chemtech Ltd. Four sections of 180 mm diameter packing with height equal to 315.0 mm, 157.5 mm, 157.5 mm and 315.0 mm are equipped in the packed column from bottom to top. As specified by the manufacturer, the Mellapak 250.Y packing have a low volume fraction, α=12%.

The column is operated in a counter-current flow configuration. The liquid from a water tank is supplied to the liquid distributor using a pump with an electronic controller and an OMEGA FMG71B-A-BSP magnetic inductive flow meter with an accuracy of $\pm$2.0%. Air from two Windjammer 119153 air blowers is injected into the column filled with structured packing through an air distributor at the bottom of the column to allow gas to flow into the column uniformly. The air flow rate is regulated by a voltage controller and measured by a TSI airflow TA465 multifunction anemometer with an accuracy of $\pm$3.0%. For a given liquid flow rate, the gas flow increases incrementally from a minimum value of 1.11 m/s up to 6.89 m/s. Two Cole-Parmer T-68075-10 pressure transducers, with a precision of $\pm$0.25%, are placed at the top and bottom of the column where the gas flow and liquid flow are introduced to the packed column. A WIKA FLM-S Magnetostrictive level transmitter with an accuracy of $\pm$0.5 mm is used to monitor the amount of liquid inside the water tank. By accounting for the liquid inventory staying in the piping of the system, the global liquid

holdup can be calculated. The measured liquid holdup is then used to verify the liquid holdup calculated by Maxwell equations.

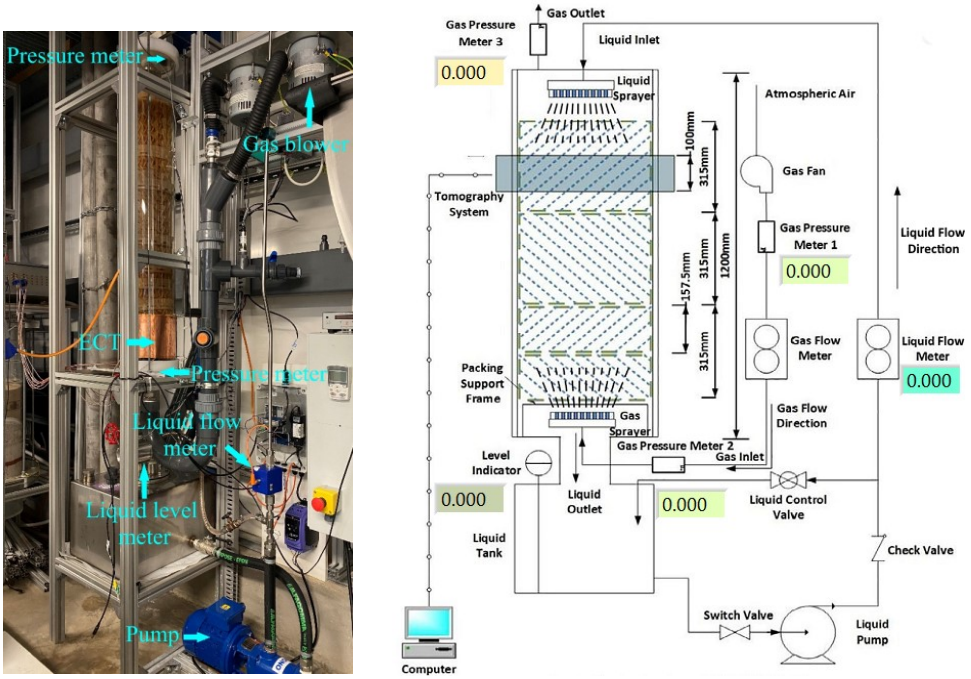

(a) (b)

Figure 4-2: (a) Photo and (b) schematic diagram of the experiment rig.

Before the experiments, the ECT sensor is calibrated with an empty pipe. In the experiments, the ECT sensor is positioned firstly at the bottom of the column, as shown in Figure 4-2 (a). Pressure differential readings are taken using the two pressure transducers placed at the top and bottom of the column, respectively. The level transmitter placed in the water tank is used to estimate the global liquid holdup within the region where the ECT sensor is mounted. In all experiments, the packed column is operated at a constant liquid flow rate (21.17 m^3/m^2h) whereas the gas flow rate is increased in the minimum increment until the column is flooded. The liquid flow rate is the rate (m^3/m^2h) at which the water moves down through the packed column during operation. The liquid flow rate is calculated by dividing the flow rate (m^3/h) by the cross-section area (m^2) of the packed column. The gas flow rate is changed every 3 minutes to ensure the flow pattern is stabilized after the change of the gas flow rate. Therefore, the data is acquired simultaneously using the ECT sensor, the pressure sensor, and the level meter for both unsteady-state and steady-state flows. The sampling frequencies of ECT are 714 fps. The sampling frequencies of pressure sensors, flow meters and the level meter are 10 Hz.

4.2.3 Dataset Construction

The first step in the dataset construction is to collect the flooding data for all the packed column experiments. The data from two scenarios, i.e. ECT installed on the bottom and top sections, are collected. When the flow pattern of the process is stable, a large amount of repeated data will be collected, which will possibly lead to overfitting. Only the most important section containing information about transients in the process is used [131]. The second step is to identify appropriate flooding indicators. Based on a previous study by some of the authors, the ECT measured capacitance can be a good indicator of flooding for the packed column [7]. Other variables, e.g. pressure drop and global liquid holdup, measured during the process will be used for comparison. An operating liquid load of 21.17 m^3/m^2h is used for all test conditions. The operating temperature is approximately 20 ^oC at 1.01 bar. Gas flow velocities from a minimum value of 1.11 m/s up to 6.89 m/s are tested to collect the data from the full range of available conditions to avoid data selection bias. The liquid holdup will constantly change as the gas flow velocities increase incrementally at the ECT measured location. The liquid holdup data is collected over 30 seconds at a rate of 10 Hz. For each scenario, 35 sets of different air flow rates are generated, each set with 300 samples. Therefore, a dataset with a total of 10,500 samples is created. The basic ECT measurement strategy is adopted [10] and a completed measurement cycle containing 28 capacitance measurements. Each sample contains an 8*8 Electrical Capacitance Image (ECI) which represents capacitance measurements and a true local liquid holdup derived from level meter measurements.

	1	2	3	4	5	6	7	8
1	C_{1-1}	C_{1-2}	C_{1-3}	C_{1-4}	C_{1-5}	C_{1-6}	C_{1-7}	C_{1-8}
2	C_{2-1}	C_{2-2}	C_{2-3}	C_{2-4}	C_{2-5}	C_{2-6}	C_{2-7}	C_{2-8}
3	C_{3-1}	C_{3-2}	C_{3-3}	C_{3-4}	C_{3-5}	C_{3-6}	C_{3-7}	C_{3-8}
4	C_{4-1}	C_{4-2}	C_{4-3}	C_{4-4}	C_{4-5}	C_{4-6}	C_{4-7}	C_{4-8}
5	C_{5-1}	C_{5-2}	C_{5-3}	C_{5-4}	C_{5-5}	C_{5-6}	C_{5-7}	C_{5-8}
6	C_{6-1}	C_{6-2}	C_{6-3}	C_{6-4}	C_{6-5}	C_{6-6}	C_{6-7}	C_{6-8}
7	C_{7-1}	C_{7-2}	C_{7-3}	C_{7-4}	C_{7-5}	C_{7-6}	C_{7-7}	C_{7-8}
8	C_{8-1}	C_{8-2}	C_{8-3}	C_{8-4}	C_{8-5}	C_{8-6}	C_{8-7}	C_{8-8}

Figure 4-3: A schematic diagram of ECI obtained from the 8-electrode ECT sensor.

Figure 4-3 shows an ECI of capacitance distribution. ECI could better reflect the nature of the symmetrical geometry of ECT sensors compared with the conventional capacitance measurement vectors method [132, 133]. Each ECI is mapped by the normalized 56 capacitance measurement with the rest padded with 0 [132]. For each capacitance value, the left number on subscript corresponds to the excitation electrode, while the right one corresponds to the measurement electrode. Capacitance measurement C_{1-2} is assumed to be the same as C_{2-1}. Therefore, the 28 capacitance measurements are doubled to 56 capacitance measurements. The duplicate data plays a part in the speed of training. However, the redundant knowledge has been used in previous literature as a method for providing the possibility of better explanations. Examples include Sidi and Keasar [134] used down-weights redundant entries rather than discarding them to help machine-learning methods achieve better accuracy. Cells with the same number on subscript are padded with 0, e.g., C_{1-1}, because an electrode is not possible to work as an excitation electrode and measurement electrode at the same time. The ECI also gives better generalisation for the CNN structure when a full ECT measurement is implemented with 56 measured capacitances. In noisy industrial environment, all the 56 measurements could be obtained since the measured capacitance may not be equal when the excitation electrode and the measuring

electrode are interchanged, e.g., $C_{1\text{-}2} \neq C_{2\text{-}1}$. Figure 4-4 shows COMSOL Multiphysics simulation models to show the superior features of ECI. The colour bar represents the values of capacitance. In these cases, the proposed ECI significantly facilitates the implementation of the neural network as the 56 measurements can be directly filled into the existing network. The data from each scenario is randomly divided into a training set with 8,925 samples and a test set with 1,575 samples. The training data set is used to develop the CNN-aided liquid holdup predictors while the test data set is used to evaluate the predictors.

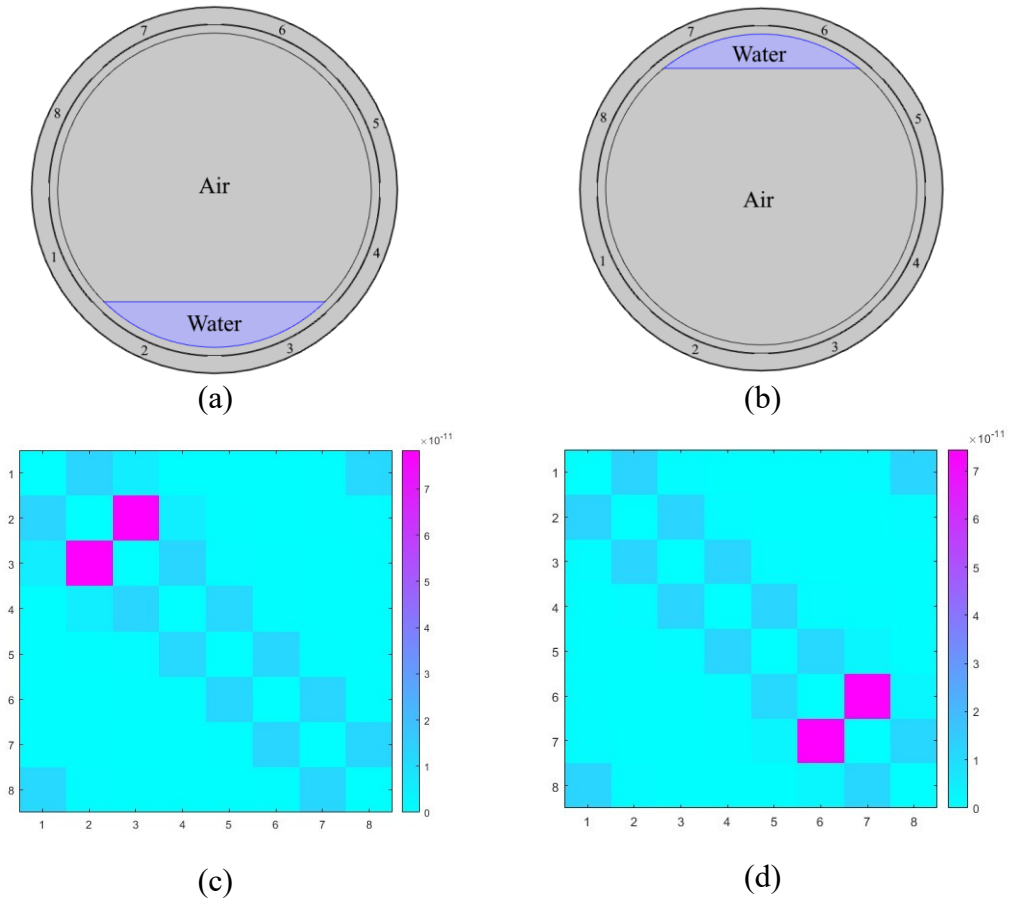

Figure 4-4: COMSOL Multiphysics simulation setup for analysis of the stratified model of air-water flow. (a) Water at bottom. (b) Water at top. (c) and (d) ECI for corresponding simulation shows the centrosymmetric feature of ECT.

4.2.4 CNN Network architecture

Different CNN architectures are tested on both the simulation dataset and the experiment dataset whilst changing certain parameters to evaluate their significance with regards to the classification accuracy results. Then, a CNN is established to predict the local liquid holdup using the network structure shown in Figure 4-5. The CNN contains four convolution layers, four average pooling layers and a fully connected layer. The input is the capacitance measurements with dimensions of 8*8*1. The real-time local liquid holdup values are calculated as reference labels. ECT training data with liquid holdup labels is pretreated by using the average method because capacitance and liquid holdup is collected at different frequencies. The weight matrix size of the kernel function is chosen as 2*2 due to the small size of the input data. The depth of the convolution layer increases from 32 and ends up with 128. Finally, a regression layer is connected to the output of the fully connected layer, performing as the final output layer of the CNN, that is, the predicted liquid holdup. Detailed hyperparameters of the CNN is shown in Table 4-1.

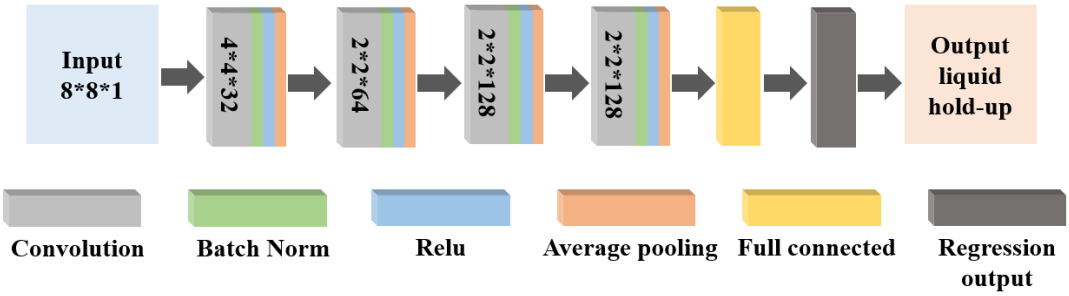

Figure 4-5: Schematic of a CNN structure for flooding prediction.

Table 4-1: Units for magnetic properties hyperparameters of CNN implemented in this work.

Layer	Input dimension	Output dimension	Weight matrix size	Stride	Padding
Conv1	8×8×1	5×5×32	4×4	(1,1)	0
Average pool 1	5×5×32	2×2×32	2×2	(2,2)	0
Conv 2	2×2×32	2×2×64	2×2	(1,1)	0
Average pool 2	2×2×64	2×2×64	2×2	(2,2)	0
Conv 3	2×2×64	2×2×128	2×2	(1,1)	0
Average pool 3	2×2×128	2×2×128	2×2	(2,2)	0
Conv 4	2×2×128	2×2×128	2×2	(1,1)	0
Average pool 4	2×2×128	2×2×128	2×2	(2,2)	0
Fc 1	512	1	2×2	-	-

4.2.5 Training

The ECI is represented as c, the output liquid holdup as $\widehat{h_L}$, and the network CNN-ECI as $f\ (\cdot;\theta)$, where θ denotes the hyperparameters of CNN-ECI. c can be mapped to $\widehat{h_L}$ by $f\ (\cdot;\theta)$:

$$\widehat{h_L} = f\ (c;\theta) \tag{4.1}$$

$\widehat{h_L}$ is expected to be as close as possible to the reference liquid holdup h_L. This purpose can be achieved by adjusting θ to minimise the loss function $E(c, h_L;\theta)$:

$$E(c, h_L;\theta) = E\|h_L - f\ (c;\theta)\|_2^2 \tag{4.2}$$

To avoid overfitting, an L_2 regularisation term is added as a weight to the loss function $E(c, h_L;\theta)$ [135]. The weighted loss function with the L_2 regularisation term is derived from the equation:

$$E_R(c, h_L;\theta) = E(c, h_L;\theta) + \lambda\Omega(w) \tag{4.3}$$

where w is weight vector, λ is regularisation coefficient. The regularisation function $\Omega(w)$ is given by:

$$\Omega(w) = \frac{1}{2}w^T w \tag{4.4}$$

Stochastic gradient descent with a momentum (SGDM) algorithm [135] is employed to optimise the networks in this work. The initial learning rate is 10^{-5}. L_2 regularisation is employed to prevent the networks from overfitting with the penalty factor set as 10^{-5}. The training and validation loss curves are shown in Figure 4-6, where RMSE is the root mean square error of the predicted liquid holdup. The number of training epochs depends on the degree of complexity of experiments. In this experiment, the number of epochs is set as 30 for adequate convergence. The batch size of each update is 128. The smallest validation loss appears at the 8th epoch. When trained with more epochs, the validation loss converges at a slightly higher value, meaning that the network is overfitted. The network is implemented with Deep Learning Toolbox in MATLAB on a computer with an Nvidia 1660 Ti GPU.

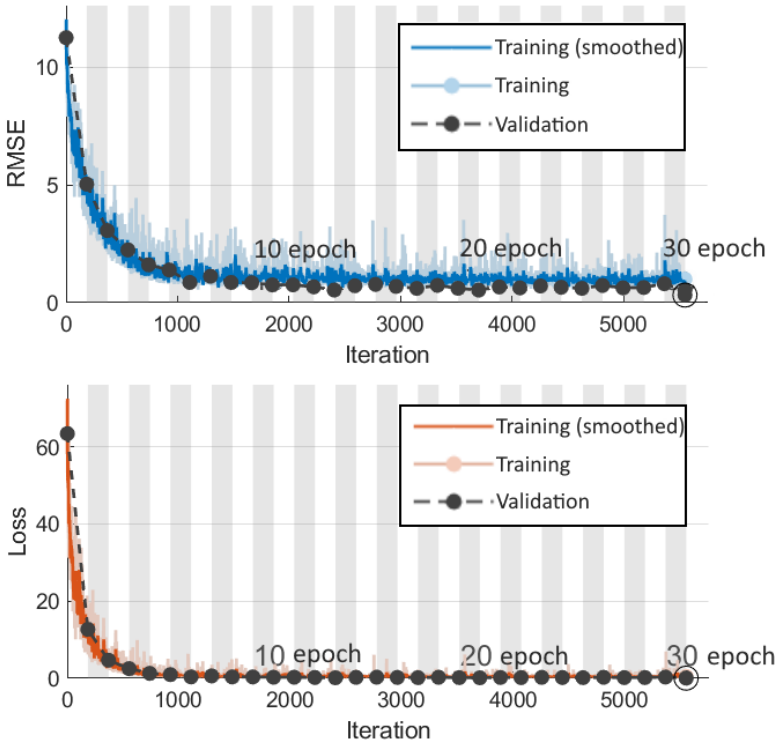

Figure 4-6: Training and validation curves.

4.3 Results and discussion

ECT measurements are first used to reconstruct the liquid distributions. Then, the reconstructed distributions are used to compute the local liquid holdup by using the Maxwell equations. The benefit of the CNN method is that it could directly predict the local liquid holdup without image reconstruction. Reference measurements of liquid holdup are available at the test rig. This allows the liquid holdup calculated by the Maxwell equations and the CNN method to be compared with the true liquid holdup. The effect of gas flow on the pressure drop and liquid holdup can be analysed based on experiment results. The ECT is installed on the top and bottom to measure the local loading point. Local loading points and local flooding points obtained in the ECT experiments are compared to global loading points and global flooding points obtained by measuring pressure drop and liquid holdup to assess the performance of the CNN-aided ECT method.

4.3.1 Results based on simulation data

The local liquid holdup predicted by CNN is validated with true liquid holdup. Figure 4-7 (a) explicitly shows the results produce a linear relationship between the predicted liquid holdup and the reference. The mean of difference and standard deviation of CNN predicted results are found to be approximately 0.02% and 0.18%, respectively. The difference between the CNN estimates and h_L shown in Figure 4-7 (b) indicates that prediction results at high liquid holdup are relatively more stable than those with low liquid holdup.

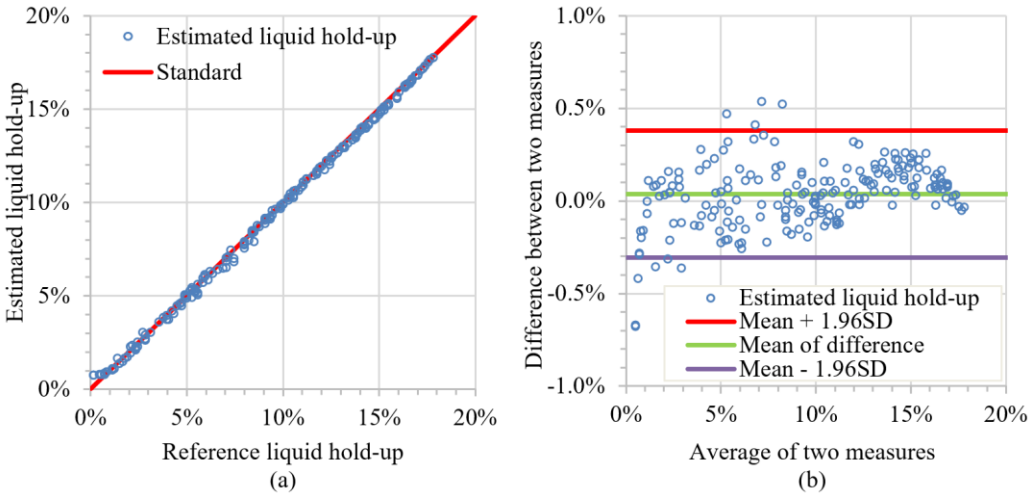

Figure 4-7: Prediction results of CNN on simulation test samples: (a) CNN liquid holdup prediction results with true liquid holdup; (b) difference of liquid holdup prediction results with true liquid holdup.

The predicted results agree well with real liquid holdup since most predicted results are bounded within the Mean $\pm$1.96 standard division error range. Therefore, the CNN method can be validated as a powerful tool for predicting the liquid holdup. These results demonstrate the utility of ECT as an agile, low-cost, non-invasive and non-destructive method for characterising hydrodynamics in post-combustion carbon capture packed column. It offers advantages over other liquid holdup measurement techniques and the proposed CNN method is expected to achieve good performance for the liquid holdup measurement. However, the simulation data does not add any noise, and the ECT may be disturbed by environmental or system noise. To verify the practical effect of the proposed CNN method, the CNN model should be validated with real experimental data.

4.3.2 Results based on bottom section of packed column flooding experiment data

1) Real-time measurement of local liquid holdup

Real-time liquid distribution of structured packing obtained in previous studies using an ultrafast electron beam X-ray tomography technology indicated that the presence of packing in counter-current flow resulted in different scales of liquid maldistribution [85, 136]. Figure *4-8* shows the ECT reconstructed images of the liquid distributions

for the given gas flow rates. The maximum holdup value in the liquid holdup map is set to 100% for all results in order to have good contrast on pictures. Figure *4-8* shows that the images at the bottom section clearly show liquid accumulation for gas superficial velocities higher than 4.49 m/s due to the liquid loading at the bottom of the column.

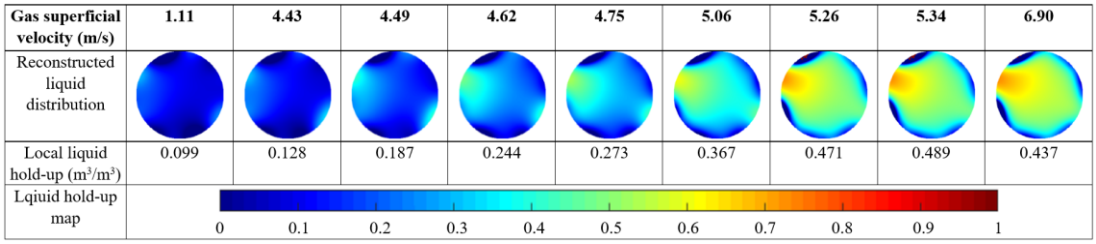

Figure* 4-8*: Reconstructions of permittivity across the whole packed column in a representative liquid holdup distribution. Cross-sections of conductivity changes at the bottom (0 mm) of the packed column at given gas superficial velocities.

The ECT could monitor local liquid holdup online without disrupting process operations and is, therefore, a preferable method to monitoring flooding. The local liquid holdup values computed using the Maxwell equation are plotted against those measured using the level meter, as shown in Figure 4-9. With a relatively lower liquid holdup (<13%), the Maxwell equation method predictions agreed with measurements to within 4%. Another important finding is the vertical pattern in the data points in Figure 4-9 (a). According to these results, it can be inferred that a maximum value of reference liquid holdup was obtained at approximately 57.8% since the capacity of packing is limited. This also explains the inclined pattern in the data points in Figure 4-9 (b). With the increase of liquid holdup, the Maxwell equation method suffers from large errors, showing an increase in maximum error from 4% to 68% compared to the reference liquid holdup. This level of agreement is likely not going to be satisfactory for packed column design. Those errors mainly come from the following two aspects: (a) linear simplification of Maxwell equation does not fit for the high liquid holdup, and (b) highly turbulent flow under flooding produces larger signal fluctuations. Therefore, a more accurate prediction method is desirable because adjustments of packings and solvents can lead to a higher value of liquid holdup. In the following context, the proposed CNN-aided ECT technique is examined to acquire accurate liquid holdup.

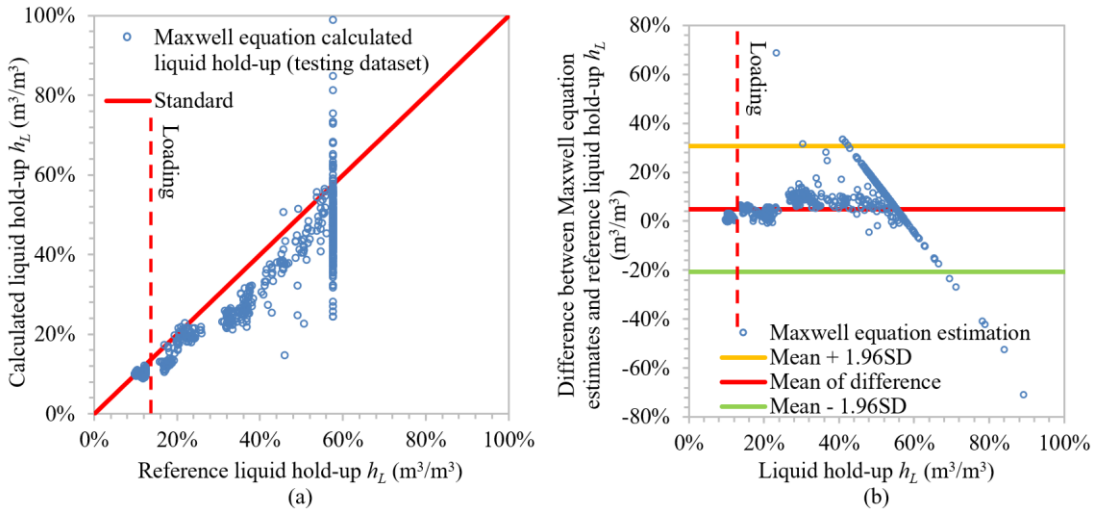

Figure 4-9: At the bottom section of the packed column, (a) Maxwell equation predicted local liquid holdup and reference local liquid holdup and (b) their differences.

2) Convolutional Neural Networks predicted local liquid holdup

In this subsection, the local liquid holdup predicted by CNN is validated in the same way as the local liquid holdup derived by the Maxwell equation, by comparing the reference local liquid holdup measured with the level meter. Figure 4-10 explicitly shows the results exhibit general linear relationships between the predicted liquid holdup and the reference. By comparing Figure 4-9 and Figure 4-10, it is obvious that a significant improvement is obtained in the majority of cases, and such improvement becomes more obvious with liquid holdup higher than 13%. The mean of difference and standard deviation of CNN predicted results is found to be 1% and 1.3%, whereas for the Maxwell predicted results are 5% and 13.1%, respectively. The difference between the CNN estimates and the reference liquid holdup shown in Figure 4-10 (b) indicates that predicted results at low liquid holdup are relatively more stable than those with high liquid holdup. The divergence of the data from the expected linear relationship for a higher value of liquid holdup (>13%) may be caused by the larger signal fluctuations possibly produced by the highly turbulent flow under flooding.

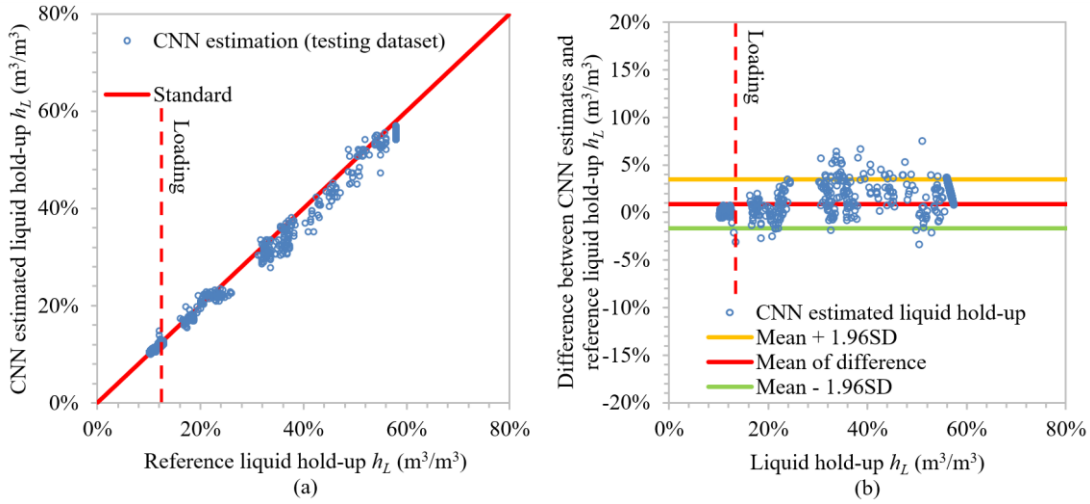

Figure 4-10: At the bottom section of the packed column, (a) CNN predicted local liquid holdup and reference local liquid holdup and (b) their differences.

3) Determination of Flooding

In order to provide a better explanation of the results, the terminologies involved will be presented in detail.

- Pre-loading zone: In the pre-loading zone, liquid flows freely onto the structured packing without any influence from the counter-current vapor flow. Therefore, the liquid holdup is only a function of liquid film formed on the structured packing surface. This zone will last until the loading point of a column, where the gas velocity is high enough to destabilise the liquid film and influence the liquid flow.

- Loading zone: When the operating column transitions from preloading zone to the loading zone, vapor flow rate starts to influence the liquid film formed over the packing. The point where this transition occurs at ECT monitored area is the loading point. The load point can be defined as the critical point at which the vapor kinetic energy is sufficient to destabilize the liquid film and influence the liquid flow. In the loading zone, the liquid gradually accumulates in the packed column due to the counter-current vapor flow and eventually completely submerged the entire packed column.

According to previous studies [137], loading points are established by a rapid increase in pressure drop and liquid holdup. Loading could be identified visually through the transparent glass pipe, indicated by a turbulent layer of liquid accumulating at the bottom of the column, as shown in Figure 4-11 (d). Flooding could also be identified visually through the transparent glass pipe, indicated by the entire column being filled with liquid and the high turbulent flow with a large amount of bubble going through the packing voids, as shown in Figure 4-11 (d). The flooding point is identified visually when the top of the column is flooded. All these physical phenomena observed in the experiments are in agreement with the literature [81]. However, the loading or flooding points determined by visual observation could cause large errors [137]. In this study, the local loading point and global loading point are determined when the gradient of each process variable reaches a value above 10% to help with quantitative calculations. Results of global liquid holdup and pressure drop are used to identify global loading point, whereas results of local liquid holdup are used to identify local loading point. The earliest detection of the loading phenomenon will indicate the transition from pre-loading zone to loading zone. In the pre-loading zone, mass transfer efficiency is independent of flow rate. In the loading zone, liquid will start to accumulate or "load" at the bottom of the bed. Partial flooding could occur at higher gas rates in this zone to achieve maximum mass transfer efficiency.

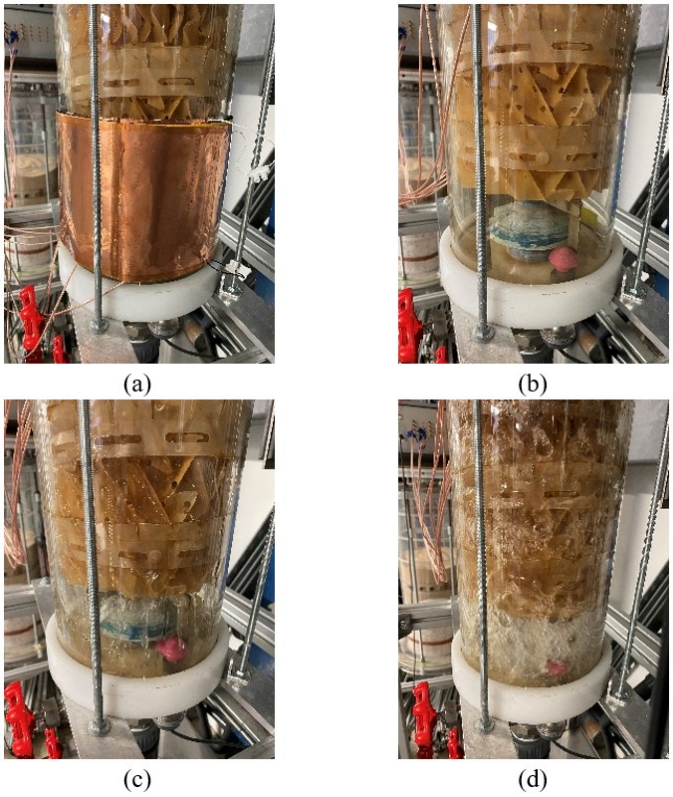

Figure 4-11: Photos of bottom end of the packed column with (a) ECT sensor, (b) no flow, (c) non-flooding water flow, and (d) flooding and entrainment.

4) Global loading point

In Figure 4-12, the global liquid holdup measured by the level meter is plotted against the gas superficial velocity at a specific liquid load of 21.17 m^3/m^3h. As the gas superficial velocity increases, the global liquid holdup shows continual growth. The liquid holdup of the entire column remains relatively constant until the gas flow velocity reaches 5.26 m/s. Beyond this point, a small increment of the gas flow results in a sharp increase of global liquid holdup that reaches between 33.9% and 36.5% of liquid holdup at 6.89 m/s. The global loading point is identified here as the gradient of global liquid holdup measurements reaches 10%. In this instance, the global loading point occurs at a gas velocity ranging from 5.26 m/s to 5.34 m/s. After the global loading point, the curve maintains a clearly rising slope, indicating rapid accumulation of liquid in the column.

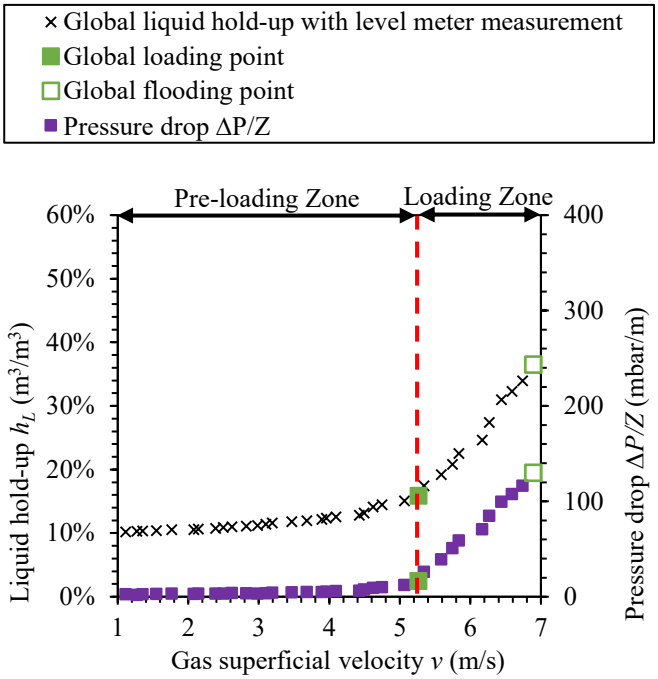

Figure 4-12: ECT installed at the bottom section of the packed column. Dependence of level meter measured global liquid holdup and pressure drop on gas superficial velocity.

Typical results of pressure drop across the whole column are also shown with purple squares in Figure 4-12. The abscissa in the figure indicates the gas superficial velocity, while the secondary ordinate indicates the pressure drop. It can be seen that the general trend of the pressure drop curve is the same as the global liquid holdup curve. The pressure drop of the entire column remains relatively constant until the gas flow reaches 5.26 m/s. Then, the pressure drop increases dramatically reaching values between 116.2 mbar/m and 129.6 mbar/m at 6.89 m/s. In this case, the global loading point is identified where a rapid increase of gradient (>10%) occurs in the pressure drop curve. Green solid squares are used to indicate global loading point in Figure 4-12. However, the loading point determined according to the gradient of the pressure drop and the global liquid holdup did not match the observations, showing discrepancies of 19% slower than accumulation of liquid been observed. After the global loading point, the pressure drop curve maintains a positive slope, meaning that the accumulation of liquid reduces the cross-section area occupied by the gas phase and therefore accelerates the pressure drop rise. Green hollow squares are used to indicate global flooding point in Figure 4-12, which was identified visually when top of the column is flooded.

5) Local loading point

Local liquid holdup predicted by Maxwell equation and CNN is illustrated using the red triangle and sky blue cross lines on Figure 4-13. Results from both methods are relatively consistent with global liquid holdup in the pre-loading zone. Interestingly, in the pre-loading zone, the local liquid holdup initially decreases from 10.9% to 9.3%, forming a minimum value, and then increases up to 57.8%. Prior studies [7, 128] also observed a similar phenomenon. A possible explanation is that the increase in gas flow breaks up the falling liquid film and causes liquid flow reversal.

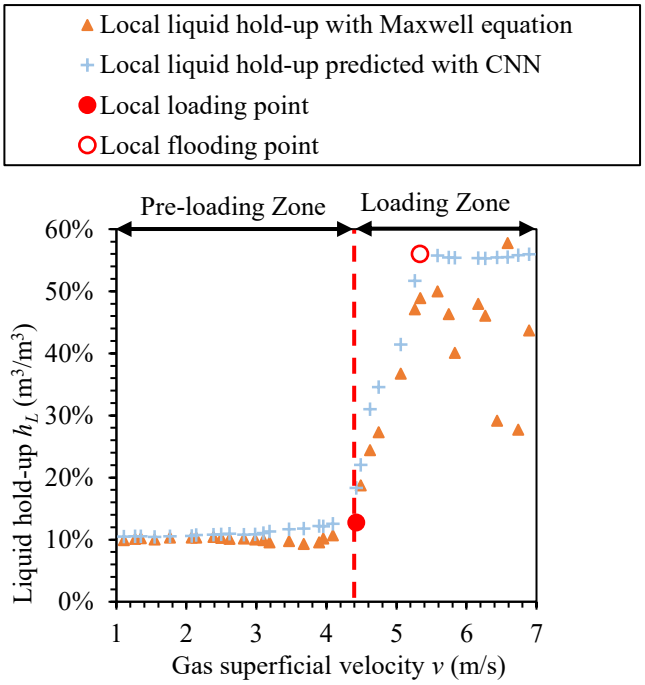

Figure 4-13: ECT installed at the bottom section of the packed column. Dependence of Maxwell equation and CNN predicted local liquid holdup on gas superficial velocity.

The local liquid holdup predicted with CNN remains relatively constant for gas velocities below 4.43 m/s, then increases dramatically to a plateau of 56%. The same local loading point is identified with a rapid increase in local liquid holdup calculated with the Maxwell equation at 4.43 m/s gas flow, shown as the red solid point at 4.43 m/s. The local loading points determined according to the gradient of the local liquid holdup matched very well with the observations. However, the gradient of the pressure drop and the global liquid holdup with respect to gas velocity had no significant change

up to gas velocity of 5.26 m/s. These results indicate that detection of localised loading can be achieved by ECT at lower gas velocities than with conventional methods. After the local loading point, it can be seen that the plateau reaches maximum values between 55% and 56% with CNN and remains constant to the end of the experiment. The local flooding point, marked as red hollow point, is identified here as flooding was identified visually above the ECT. However, the Maxwell equation calculated local liquid holdup at the plateau is very unstable at a range between 27.7% and 57.8%.

To summarise this section, the occurrence of the local loading point can be detected using the ECT at the bottom of the column. The increase in liquid accumulation in the loading zone corresponds to an increase in high relative permittivity material (water), which is detected by the ECT. Physically, because the local liquid holdup accumulation is much faster than the global liquid holdup, the Maxwell equation method and CNN method are both good indicators of loading point. The main difference lies in the trend after the loading point, where local liquid holdup shows a greater than 70% increase but global liquid holdup shows only about a 20% increase. The direct comparison with pressure drop and global liquid holdup with level meter measurement shows the validity of using ECT for the detection of liquid loading on packing.

4.3.3 Results based on top section of packed column flooding experiment data

1) Real-time measurement of local liquid holdup

Similar to the experiments at the bottom section, Figure 4-14 shows the image reconstruction of liquid distribution for the selected gas flow rates at the top section of the packed column. Images at the top section show liquid accumulation from 6.74 m/s gas superficial velocity due to the liquid loading from the base upwards. The results suggest that the distribution of liquid holdup can be reconstructed, but the structural detail, such as small-scale maldistribution due to packing channels, cannot be observed in the images.

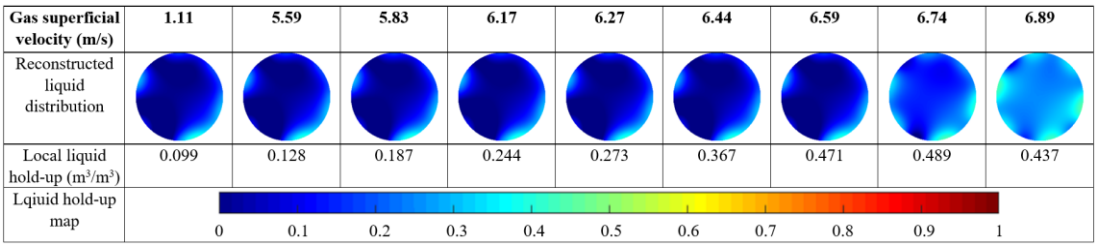

Figure 4-14: At the top section of the packed column, (a) CNN predicted local liquid holdup and reference local liquid holdup and (b) their differences.

The liquid holdup values calculated using the Maxwell equation, for gas flow rates from non-flooding to flooding, are plotted against those measured using the level meter, as shown in Figure 4-15. Before the red doted loading line, the measured liquid holdup agreed with the estimations of liquid holdup to within 2%.

Figure 4-15 (b) shows that Maxwell equation estimations have the smallest relative error on samples before the red doted loading line, at about 10%, but the largest relative error on relative high liquid holdup, at approximately 39%. This is a clear drawback of using the Maxwell equation to predict local liquid holdup as the predicted results with large error after flooding onset occurs at the top section. Therefore, the larger the liquid holdup value is, the more significant deviation between the two measurements.

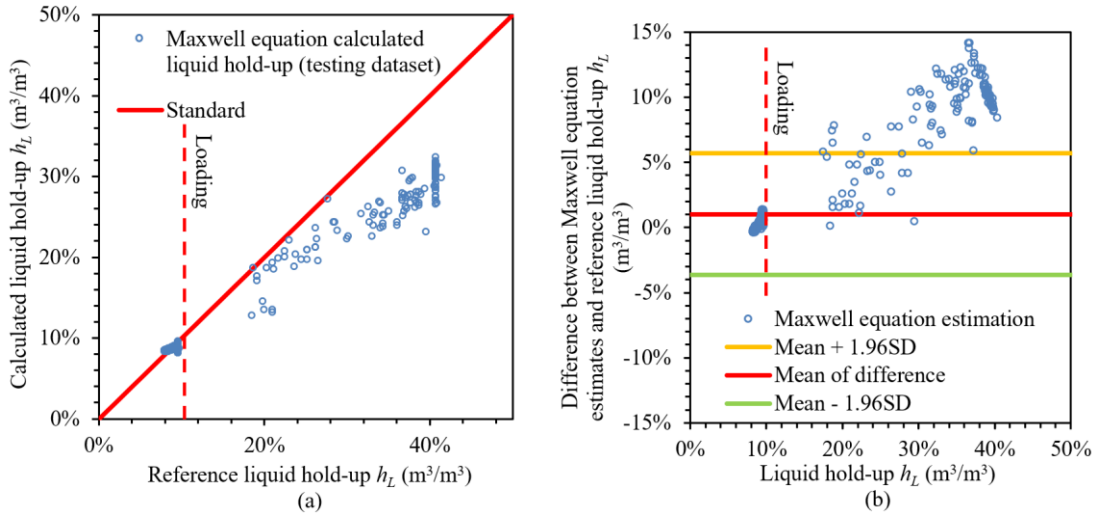

Figure 4-15: At the top section of the packed column, (a) Maxwell equation predicted local liquid holdup and reference local liquid holdup and (b) their differences.

2) Convolutional Neural Networks predicted liquid holdup for flooding in packed column

The CNN predicted local liquid holdup results are shown in Figure 4-16. The results exhibit generally linear relationships between the CNN estimated liquid holdup and reference liquid holdup. The difference between CNN estimates and reference liquid holdup in Figure 4-16 (b) shows that lower liquid holdup (<10%) are relatively more stable than higher liquid holdup (>10%). By comparing Figure 4-15 and Figure 4-16, it is evident that a significant improvement is obtained in most cases, and such improvement becomes more obvious for the higher liquid holdup (>10%). The mean of difference and standard deviation of CNN predicted results at the top section data sets are between 0.3% and 1.3%, whereas for the Maxwell predicted results are 1% and 2.4%, respectively. These results indicate that the CNN model better predicts local liquid holdup in the packed column, especially at high liquid holdup.

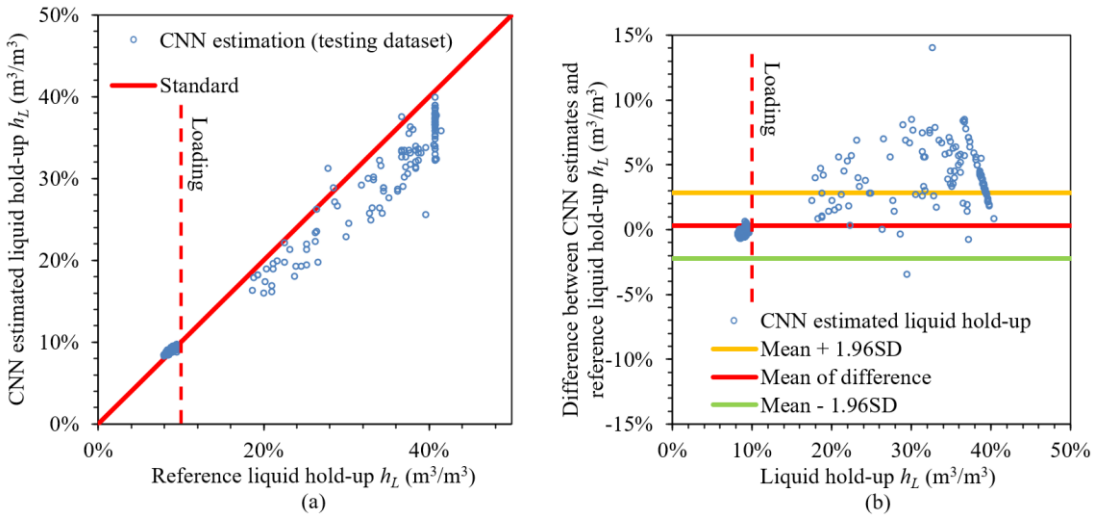

Figure 4-16: At the top section of packed column (a) CNN predicted local liquid holdup and reference local liquid holdup and (b) their differences.

3) Determination of flooding point

Similar to the experiments at the bottom section of the packed column, Figure 4-17 shows a comparison between the process variables such as pressure drop and liquid holdup used for flooding prognosis. According to Billet and Schulets [64], the

phenomenon of flooding includes liquid accumulation at the top of the bed. Our study uses experimental data sampled from the top section of the packed column to determine the local loading point as an early warning of flooding point, as shown in Figure 4-18. Flooding can be identified visually through the transparent glass pipe given a turbulent layer of liquid upon the top of the column. Therefore, the experiment is stopped when the flooding and entrainment are spotted at the top of the column, as shown in Figure 4-17 (d).

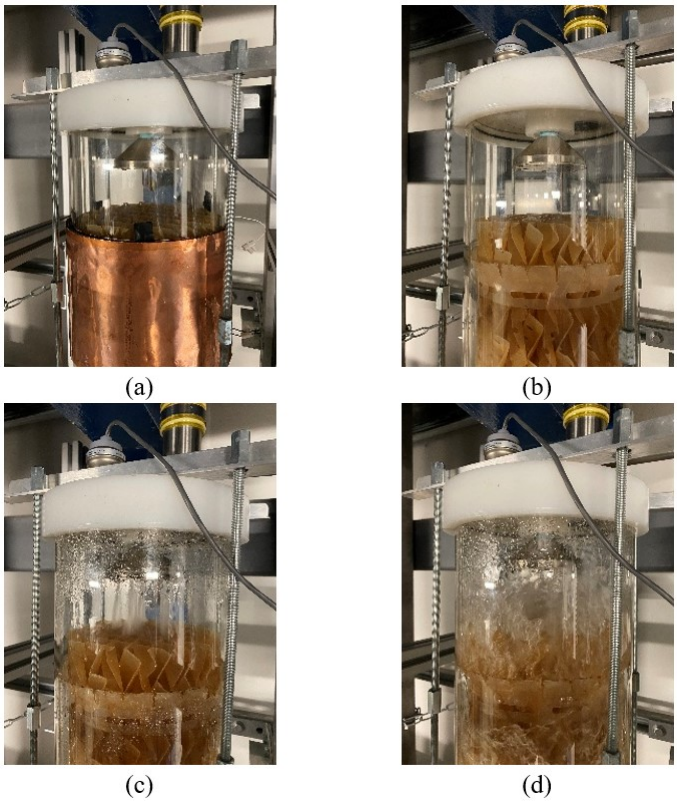

Figure 4-17: Photos of top end packed column with (a) ECT sensor, (b) no flow, (c) non-flooding water flow, and (d) flooding and entrainment.

Global liquid holdup and global pressure drop are plotted for all the 35 air flow rates. It can be seen from Figure 4-18 the overall trends of the pressure drop curve and global liquid holdup curve are similar to those at the bottom section, under the same experimental conditions. Green solid squares are used to indicate the global loading point. The global loading point is identified here as the gradient these measurements have achieved a value of 10%. However, the gradient of pressure drop increases more rapidly than that at the bottom section. It is most likely that the pre-flooding causes this phenomenon by improving packing wetting degree [138].

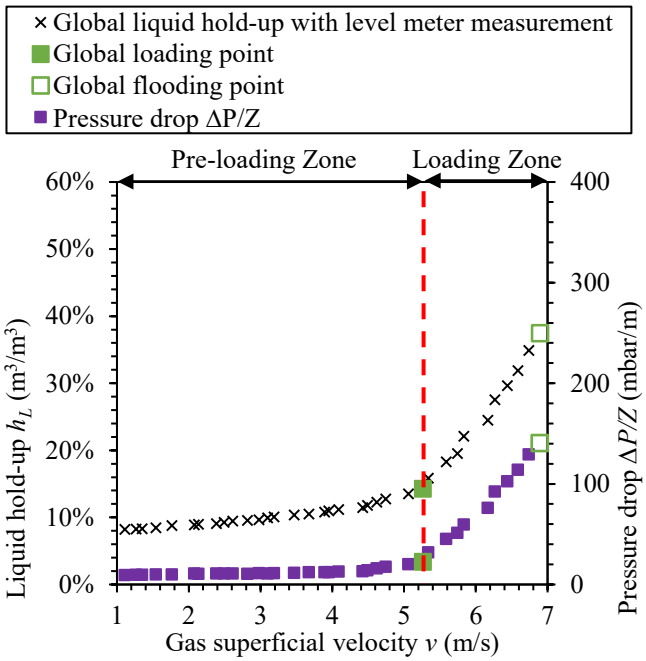

Figure 4-18: ECT installed at the top section of the packed column. Dependence of level meter measured global liquid holdup and pressure drop on gas superficial velocity.

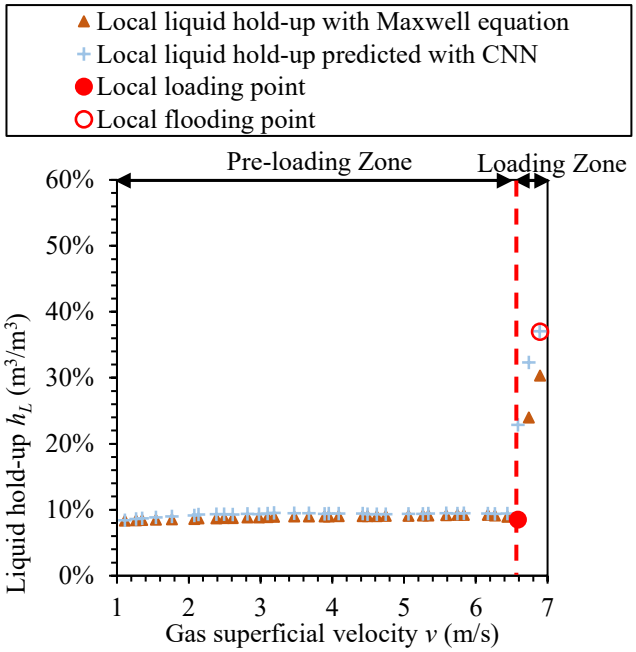

Figure 4-19: ECT installed at the top section of the packed column. Dependence of Maxwell equation and CNN predicted local liquid holdup on gas superficial velocity.

As shown in Figure 4-19, the Maxwell equation calculated local liquid holdup and the CNN estimations range from 8.4% to 37.1% during the flooding experiment. In the pre-loading zone, a small change of the gradient of local liquid holdup is observed at

the top section of the packed column. Before the local loading point (marked as the red solid circle), no temporary accumulation of liquid at the top of the bed is observed. More importantly, the gas velocity does not affect the local liquid holdup until the local loading point at the top is achieved. It can be concluded that the local liquid holdup is independent of air flow rate, leading to low interfacial area and gas-liquid interactions at the top section [64]. The two curves show a very similar tendency, with a sharp rise observed when the flooding front has advanced up. The Maxwell equation predicted local liquid holdup remains relatively constant until 6.59 m/s gas flow, then increases to a peak at approximately 6.89 m/s gas flow. In addition, the CNN predicted local liquid holdup is relatively consistent with the Maxwell equation predicted ones and global liquid holdup in the pre-flooding zone, but increases much faster in the local flooding zone. The local liquid hold up may be underestimated using the Maxwell equation as the maximum liquid holdup of 30.4% is much smaller than the global liquid holdup, i.e. 37% at the same gas flow rate. In contrast, CNN estimations agree well with the global liquid holdup close to the flooding point. The local liquid holdup profile demonstrates a rapid increase of gradient in Figure 4-19 at around 37%, which signifies that the local loading point is found at approximately 6.59 m/s flow rate. This is followed by a small increase in gas velocity and excessive entrainment at top of the column was observed at the experiment, which indicates gas velocity has also achieved global flooding point (marked as green hollow squares in Figure 4-18). Therefore, it can be concluded that the local liquid holdup at the top section of the packed column can be used as the early warning of the flooding.

4.4 Conclusions

This chapter presents the first attempt at CNN-aided flooding prognostics in a packed column using ECT. The proposed CNN methods provide results that align well with ground truth liquid holdup values. ECT with CNN accurately predicts the local liquid holdup, enabling the detection of the loading point at the bottom of the packed column and the detection of the flooding point at the top of the packed column. These findings confirm that a local measurement of liquid holdup tends to be the earliest prognostic of flooding than a global pressure drop or liquid holdup. Therefore, ECT is highly

suitable for accurately predicting the occurrence of flooding and can be deployed in packed column operation to allow for active management of the flooding and optimised capture plant operation.

Publications from this chapter:

- **Y. Chen**, C. Liu, Y. Yang, M. Lucquiaud, J. Jia, Flooding Prognostic in Packed Columns based on Electrical Capacitance Tomography and Convolution Neural Network. IEEE Transactions on Instrumentation and Measurement, vol. 71, pp. 1-14, 2022.

Chapter 5 Monitoring Frost Formation during Cryogenic Carbon Capture using ECT

5.1 Introduction

As illustrated in section 2.2.2 of Chapter 2, cryogenic carbon capture is a potential technological solution to reduce CO_2 emissions and a more cost-effective method of carbon capture than amine-based CO_2 capture technologies [48]. However, there is a lack of research on frost formation of CO_2 within packed bed systems, despite the influence of the CO_2 frost layer on thermal conductivity leading to high cooling costs. Understanding the rate of CO_2 frost accumulation within a packed bed is critical to the design of the capture column. Therefore, online measurements of frost accumulation become increasingly desirable to study the CO_2 frost formation during cryogenic carbon capture. This chapter aims to test the functionality of a novel online ECT sensor and its ability to provide in-situ, real-time measurements of CO_2 frost formation in a fixed packed bed.

This chapter focuses on the evolution of frost formation distribution during the capture process. It has been investigated in detail by experiments, elucidating the effect of the bed material type and bed material temperature. An ECT sensor was constructed to measure frost distribution and elucidate the mechanisms of CO_2 frost formation by first testing on water ice frost in the packed bed. Results show that ECT could effectively monitor the changes in relative permittivity caused by the frost formation in real time [139]. These results indicate that ECT has the potential to be a novel technique for monitoring CO_2 frost formation during cryogenic carbon capture.

5.2 Materials and methodology

5.2.1 Predictive simulation

In cryogenic carbon capture processes, a non-intrusive online sensing technique with the good temporal resolution is greatly desirable for study of CO_2 frost formation and online monitoring of fast gas dynamics. However, few techniques possessing such

capabilities have been investigated and maturely applied to date. Moreover, the existence of packed column packing raises a challenge for CO_2 frost formation imaging attributed to the spatial constraints imposed by the packing structure on the change of gas dynamics. In order to reveal the feasibility of imaging CO_2 frost formation with ceramic beads by ECT, as well as the effect of ceramic beads on imaging quality, a geometric model with a regular shape random packing is established in COMSOL Multiphysics together with the presented ECT sensor.

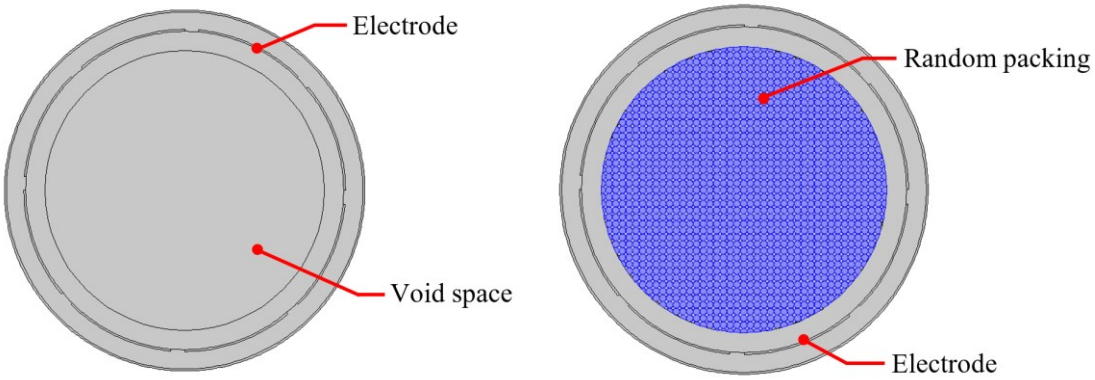

Figure 5-1: Modelling of ECT sensor with random packing. (a) Typical 2D ECT sensor; (b) 2D ECT sensor with simplified random packing.

In this work, a typical eight-electrode ECT sensor is studied, as shown in Figure 5-1 (a). Figure 5-2 shows the real random ceramic packing used in the experiment. To simplify the complexity of real random packing applied in this study, the blue circle arrays in Figure 5-1 (b) are used to emulate the random packing, while the rest grey area is referred to as void space. The presented model with ID=72 mm and OD=95 mm. The permittivity values of CO_2 frost and air are set as 1.6 and 1, respectively. Ceramic beads were selected as the random packing medium with a permittivity of approximately 30. The random packing radius is set to be 0.85 mm, as indicated in Figure 5-1 (b).

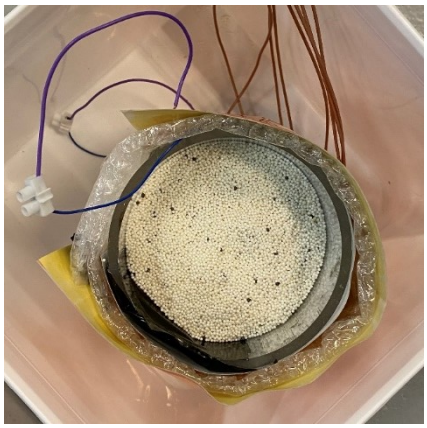

Figure 5-2: Ceramic beads used in the experiment.

5.2.2 Experimental set up

The capture column test rig consists of a small-scale cryogenic carbon capture application as shown in Figure 5-3, located at the University of Chester. More details of the test rig can be found in [46]. The experimental rig is made from a PTFE pipe, with ID=72 mm, OD=95 mm and h=1000 mm. Two feed gas injector pipes feed into the capture column, i.e. a vertical cooling gas injector and a horizontal mixed gas injector. The gas injector pipes are made from copper pipes with a series of 1 mm width perforations, across the length of the pipe that is located inside the column, on opposite sides of the copper pipe to allow gas to flow into the column uniformly. The ECT electrodes are located approximately 120 mm from the bottom of the column. The capture column was tested using small ceramic beads of Zirconia partially stabilised with Yttria from Chemco Advance Material Co., Ltd., ranging from 1.4 mm to 1.7 mm in diameter. The temperature of the bed material is recorded using thermocouples and data loggers. The thermocouples are inserted into the capture column from the top of the column and are adjusted to an appropriate height above the horizontal mixed gas (–60 °C) injector.

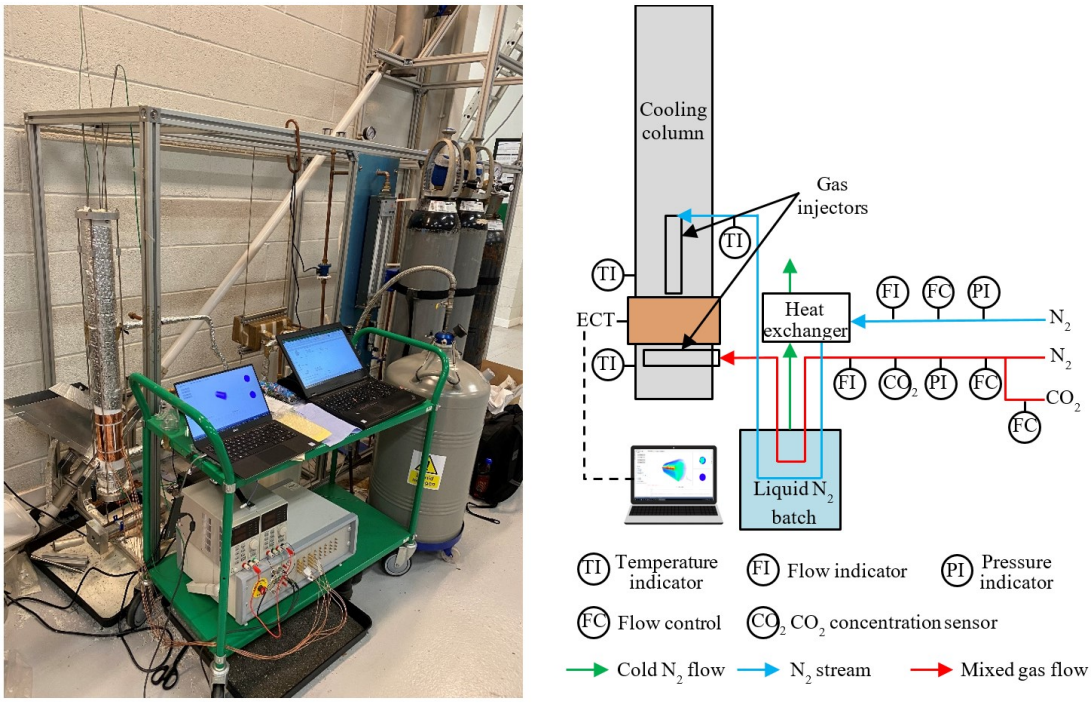

(a) Photo of experimental test rig

(b) Schematic diagram

Figure 5-3: Lab scale fixed bed experimental flow loop.

Nitrogen and CO_2 for the gas streams are supplied by BOC cylinders, with purities of 99.98% and 99.8%, respectively. The two gas injectors are used for the cooling step and capture step. The vertical cooling gas injector feeds nitrogen gas that is firstly cooled to –140 °C by passing through the liquid nitrogen bath, which cools down the ceramic bed material. The horizontal mixed gas injector feeds in a mixture of nitrogen and CO_2. The mixed gas is controlled by two automatic Bronkhorst El-Flow mass flow controllers, which set the flow rates for CO_2 and nitrogen gas before mixing the two gas streams together. The mass flow controllers provide a mixed gas flow at a specific CO_2 concentration v/v. The mixed gas is partially cooled by passing through a liquid nitrogen bath and further cooled by the bed material in the capture column. When the mixed gas is sufficiently cooled, the CO_2 present in the gas phase will desublime out of the gas phase and onto the bed material as a frost.

The composition of the mixed gas before entering the capture column and after leaving the capture column are measured with GSS CO_2 gas sensors, which have a precision of 0.001%. The in-line sensor before the capture column can detect between 0-20%

vol. CO_2 and the gas sensor in place at the outlet of the capture column can detect between 0-5% vol. CO_2.

5.2.3 Sensor optimisation for cryogenic carbon capture

According to the size of the cryogenic packed column, an ECT sensor with eight electrodes was designed in this study. Figure 5-4 (a) shows the schematic illustration of the sensor. The sensors are made of copper foil. Eight electrodes of 60 mm length are mounted outside the cryogenic packed bed and enclosed by an earthed guard electrode. In order to reduce the damage to the insulation during the cryogenic capture process due to the installation of the ECT unit, bubble wraps are used to reduce heat transfer in the freezing column and in the environment. Figure 5-4 (b) illustrates the picture of the manufactured sensor equipped with a bubble wrap for insulating operation and shield electrode.

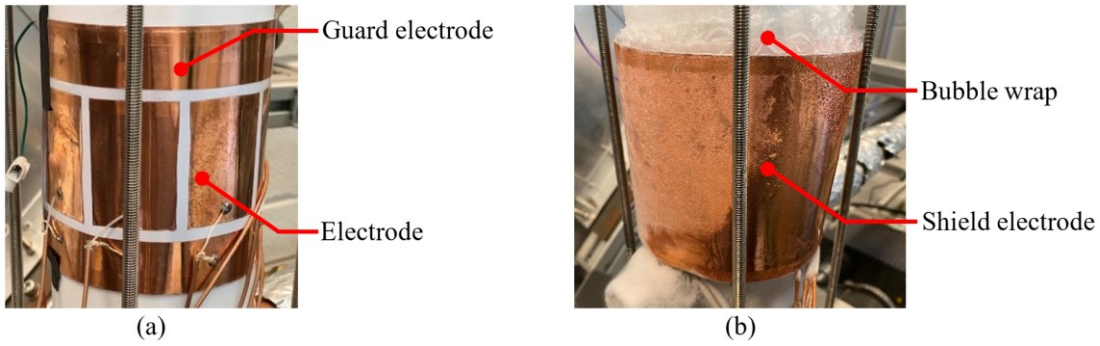

Figure 5-4: Picture of (a) the manufactured ECT sensors with guard electrode and (b) bubble wrap with shield electrode.

5.2.4 Experimental campaign

The experimental procedure begins with an empty air-filled pipe ECT reference calibration measurement to check if all electrodes are operating correctly. Next, the dry ceramic beads are added into the column and a second ECT measurement is made for calibration with dry ceramic beads. The position of thermocouples is adjusted based on ECT images. The temperature profiles from the thermocouples placed above

and below the ECT were used to estimate the temperature of the bed material within the region of the ECT sensor.

For CO_2 frost experiments, the cooling stage delivered nitrogen gas at –140 °C to the bed material. When the bed material reached the desired temperature of roughly –120 °C, the cooling stage was ended by shutting off the cooling gas stream. The ECT measurement procedure began when a cold ceramic-filled pipe ECT reference calibration measurement was taken for the ceramic packing with low permittivity material. The capture stage started by feeding a mixture of CO_2 and nitrogen through the mixed gas injector. The mixed gas, fed into the column at 40 litres per minute (LPM) with 18% CO_2 v/v, is partially cooled by passing through a liquid nitrogen bath to reach roughly –70 °C. Heat transfer between the bed and the mixed gas within the capture column would then provide sufficient cooling to the mixed gas to cause CO_2 to desublime out of the gas phase as a frost and deposit onto the bed material.

The temperature profiles would be expected to show an increase in temperature and plateau at the desublimation temperature of CO_2, for a gas of 18% CO_2 v/v, the desublimation temperature would be –97.2 °C (estimated using the Span and Wagner equation of state [140]). The presence of this plateau in the temperature profiles identifies that CO_2 frost is forming within the bed and has reached equilibrium. As mixed gas continues to pass through the column, the temperature plateau will destabilise due to CO_2 defrosting at a faster rate than it is desubliming. Using the thermocouples above and below the ECT sensor help to estimate the temperature when frost formation would be occurring within the region of bed material that the ECT sensor was measuring. When CO_2 starts defrosting, a second ECT measurement is made to determine ceramic packing with high permittivity material. Finally, after these two calibration references are taken, the ECT is connected to a computer where visualisation of the real-time images can be accessed on the computer screen, to determine whether the ECT sensor is able to detect frost formation. Also, ECT measurements are used to reconstruct the permittivity distribution off-line using the calculation method introduced in Section 2.6.

5.3 Results and discussion

5.3.1 Simulation

Figure 5-5 shows the image reconstruction of the modelled phantom. The different blues shapes in the COMSOL models simulates ceramic packing. In this study, five different blues shapes of phantom are reconstructed and compare: ellipse, rectangle, two circle, triangle and single circle. All of them are symmetric and have a relative permittivity value of 30. The background simulates a packed column filled with air, which has a relative permittivity value of 1. Note that in the reconstructed images the red colour denotes the permittivity is larger than the blue background (air). The reconstructed images show the cross sections of the packed column sensing domain. The simulation results suggest that the outline and position of ceramic can be reconstructed in the images. Next step of work will be experimental validation of the presented sensor and image reconstruction methods on practical CO_2 frost imaging.

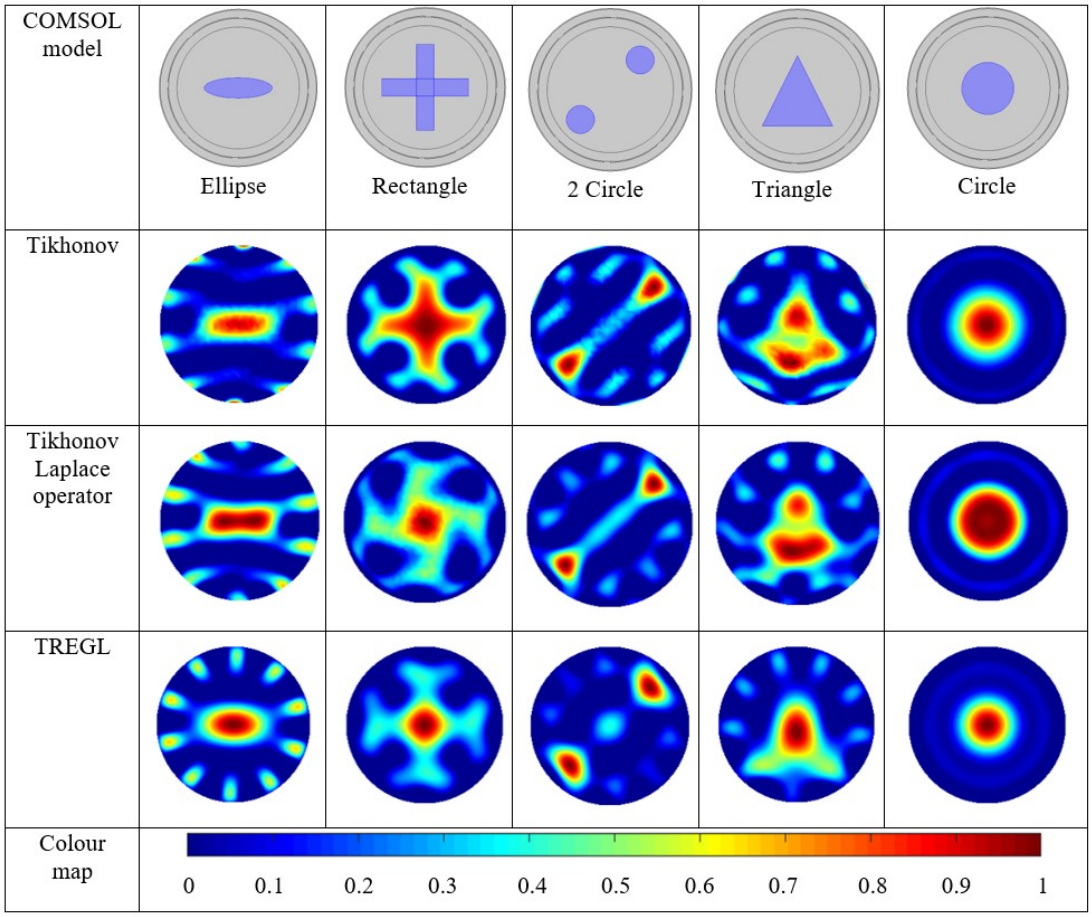

Figure 5-5: Image reconstruction of the different phantoms. The column on the left shows the algorithm used for reconstruction and on the right shows the reconstructed images.

5.3.2 CO_2 frosting experiment

Figure 5-6 shows that ECT profiles at different bed temperatures do not change much, particularly at lower capacitance values. A small relative change of capacitance indicates that the relative change of permittivity is small, which means the relative permittivity change caused by CO_2 frost is insufficient to be detectable by the ECT sensor. A greater relative change of capacitance means that the change of actual size and position of the relative permittivity differ from the original value, thus the reconstructed image can be a good presentation of the CO_2 frost change.

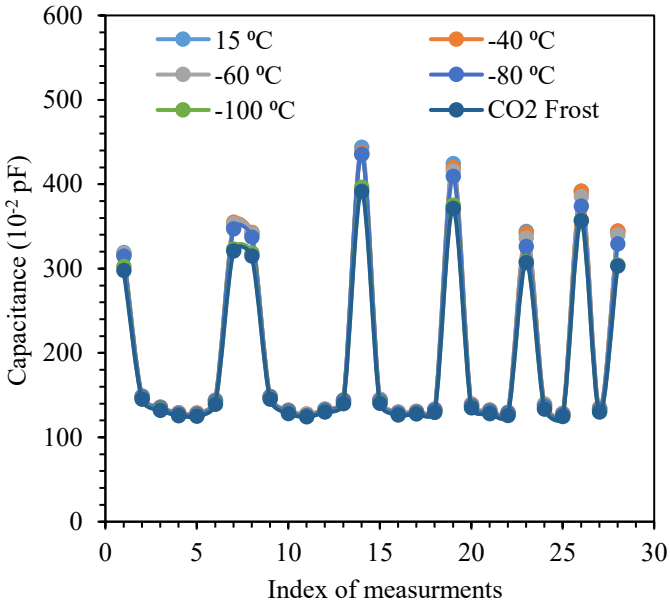

Figure 5-6: ECT measured capacitance for ceramic bed versus different temperature.

The temperature profiles in Figure 5-7 show that the temperature below the ECT reached a plateau at approximately 150 seconds. The presence of the temperature plateau shows that indeed CO_2 frost is forming on the bed material.

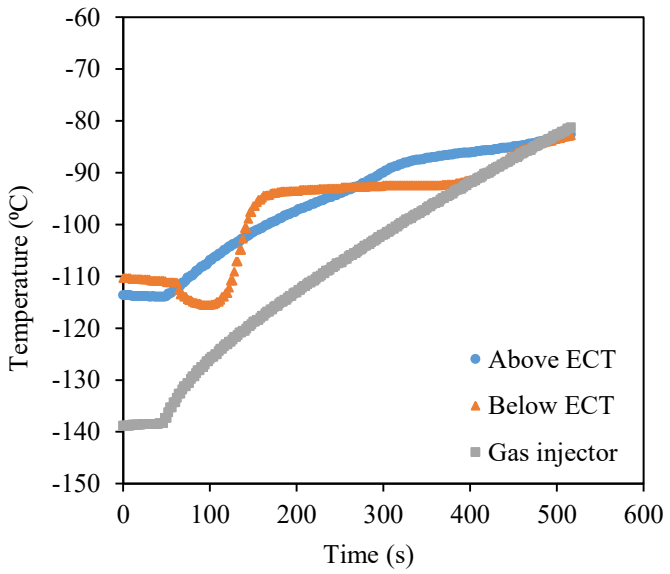

Figure 5-7: Temperature profiles of thermocouples above the ECT sensor, below the ECT sensor and gas injector under 40 LPM 18% v/v CO_2.

As shown in Figure 5-7, the capture step starts at roughly 80 seconds and the thermocouple below the ECT records a temperature profile roughly 70 seconds into

the capture step. The plateau destabilises after 400 seconds as the temperature starts to rise again, indicating the bed material is beginning to defrost. These results are consistent with data obtained in experimental analysis of CO_2 frost front behaviour studies [46]. According to Tuinier et al. [53], deposition of CO_2 causes a rise in bed temperature to an equilibrium value of approximately −93 °C and CO_2 breaks through after approximately 200 s. In our study, the equilibrium temperature of approximately −92.8 °C was recorded by a thermocouple above the ECT sensor and CO_2 breaks through after approximately 130 s. The temperature profile for the thermocouple above the ECT did not demonstrate a plateau, which makes it uncertain how fast frost accumulated in the capture column. Comparison with the ECT sensor readings during the CO_2 capture step is less accurate as a result.

Frost front velocity cannot be accurately predicted experimentally as the temperature profile above the ECT did not form a stable plateau. However, simulated predictions can be made for this experimental work and compared with simulated predictions using experimental results from Tuinier et al. [52] using correction factors derived in [46]. The correction factors consider the differences between flow rates, column dimensions, and bed material between the experimental set-ups, using equation (5.1) provided below:

$$\frac{dvdy}{dc_p d\rho} \tag{5.1}$$

where y represents the volume fraction of CO_2 in the gas phase and v represents the superficial velocity, c_p represents the specific heat capacity of the bed material and ρ represents density of the bed material. Simulated frost front velocities were calculated from equation (5.2):

$$U_{frost} = \frac{Q_g}{A\rho c_p dT} \tag{5.2}$$

where U_{frost} is the frost front velocity, Q_g is the cooling duty required by the gas phase, A is the cross-sectional area of the capture column and dT is the temperature change. Table 5-1 compares simulated results produced for conditions in this work and for experimental conditions from Tuinier et al.'s experimental work, which differ

slightly by 18%. One modification is made to Tuinier et al.'s work before applying the correction factors which is to alter the starting temperature of the bed to match this work.

Table 5-1: Frost front velocity comparison between this work and data from literature.

Simulated results	Frost front velocity (mm/s)
This work [139]	1.12
Tuinier et al. [14]	1.33

The reason the temperature profile above the ECT sensor does not show an obvious plateau is likely due to the ECT sensor. The ECT sensor attached to the capture column required the removal of insulation around the capture column, this caused the temperature of the bed material to be slightly higher than what the capture column can usually achieve. Applying the insulation around the ECT sensor affected the sensor's readings by increasing the effect of random artefacts that in the reconstructed images.

The ECT measurement procedure begins when the capture stage is started by feeding a mixed gas of CO_2 and nitrogen through the mixed gas injector. Figure 5-8 show that the ECT capacitance has little change during the entire CO_2 frost capture progress. In contrast, the presence of the temperature plateau in the temperature profiles in Figure 5-7 shows that CO_2 frost is forming on the bed material. Based on the experimental results, it was concluded that the designed ECT sensor and proposed image reconstruction methods could not properly estimate the permittivity change within the packed column in CO_2 frost capture progress.

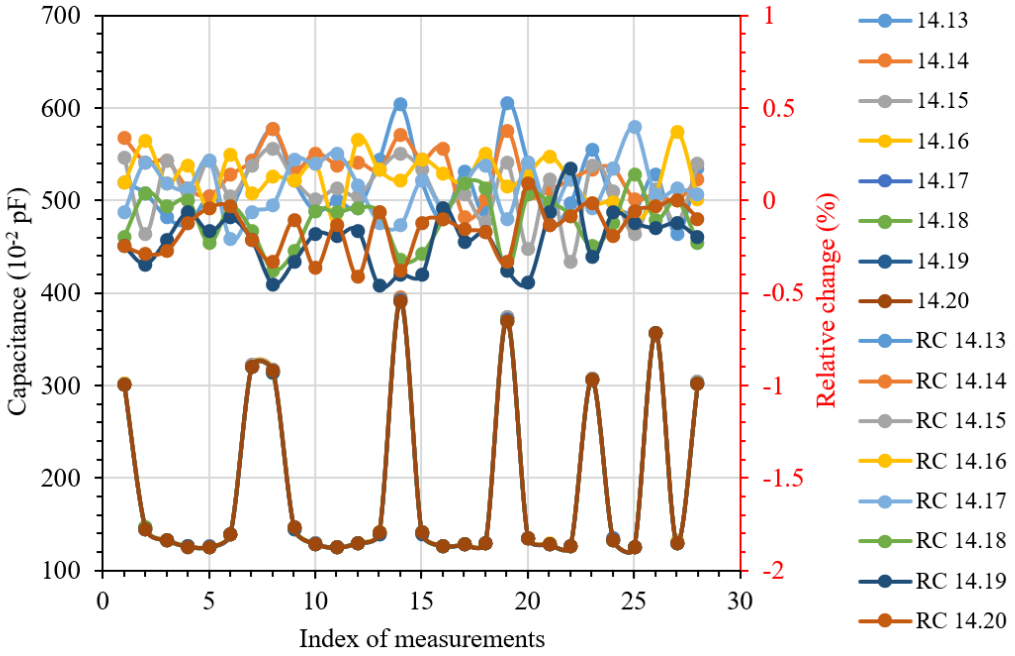

Figure 5-8: ECT measured capacitance for ceramic bed during CO2 frost formation progress (RC: relative change of capacitance).

The experimental rig fed through a gas mixture containing 18% v/v CO_2, CO_2 frost could not be detected by the ECT sensor. Increasing the concentration of CO_2 in the gas mixture would increase the mass of frost being deposited on the bed material which may have been detectable by the sensor. However, the experimental rig designed to feed up to 20% CO_2 would not be able to accurately measure the concentration of the gas mixture and would risk desublimation of CO_2 frost within the liquid nitrogen precooler. Since detecting CO_2 frost at lower concentrations would be more difficult for the ECT sensor to detect, sensitivity analysis of the CO_2 frost experiments is not continued.

The tomography sensor could not accurately detect CO_2 frost growth on the surface of the bed material. This could be due to the relative permittivity of CO_2 in the solid and vapour phase as well as the ceramic bed material or the setup of the experiment is ineffective. Further experiments were conducted to determine whether the tomographic sensor is able to detect frost growth of water droplets, which would show a much larger change in relative permittivity from phase change compared to CO_2.

5.3.3 Wet packing frosting experiment

Since the ECT sensor could not effectively detect CO_2 frost, the experimental procedure is changed to use water frost to explore the gas dynamic during ice frost formation progress in the packed column. The purpose for these experiments is to investigate two factors: firstly, whether the ECT sensor would detect water frost and subsequently whether tomography sensors are suitable for use with the experimental rig; and secondly, whether the freezing of water on the surface of the bed material gives any indication on the flow of gas through the capture column. If the ECT sensor detects water frost across the entire cross section of the capture column equally then that is evidence that the flow of gas through the capture column is uniform and predictable. Water is used as a replacement for CO_2 frost as the change in relative permittivity from water to ice (from 80 to 3.2) is substantially larger than that from CO_2 gas to frost (from 1 to 1.6). Relative permittivity of water is 88 at 0 °C and drops with rising temperature, e.g. to 55.3 at 100 °C. However, water (ice) relative permittivity is about 3.2 at −2 °C. The relative permittivity of the PTFE pipe is approximately 2.1. First, the ceramic bed material was wetted with water before being fed into the capture column, as the water would otherwise freeze inside the gas pipes when passing through the liquid nitrogen bath. Then nitrogen cooling gas was fed into the column at −15 °C to freeze the water present in the capture column. The nitrogen gas fed into the mixed gas line was used as the cooling gas for water related experiments, in order to simulate the mechanism of frost formation between the mixed gas and the bed material. The flow of cold gas through the column of wetted bed material causes water to freeze. Thus, observing the freezing of water through the ECT showed the general flow pattern of cold gas through the bed material.

Figure 5-9 shows the temperature profiles for the water frost and ceramic bed material experiments under different cooling gas flow rates. The gas injector's temperature profile mostly fluctuates within the range of −10 °C to −20 °C. Keeping the temperature of the cooling gas stable proved to be more difficult due to the high cooling duty the liquid nitrogen supplies to the cooling gas.

The temperature profile below the ECT sensor is dependent on the flow rate of gas. The temperature profile reaches 0 °C at roughly 250 seconds and −10 °C at 400

seconds for the 100 LPM graph (Figure 5-9 (b)), whereas the temperature profile reaches 0 °C at 500 seconds and −10 °C at 1000 seconds for the 50 LPM graph (Figure 5-9 (a)). The temperature profiles above the ECT sensor still have difficulty reaching the freezing temperature of the water. Due to the water being present on the bed material, the cooling duty must be supplied by the cooling gas. The ceramic bed material and water densities are far higher than that of the cooling nitrogen gas. As a result, the poor cooling duty supplied by the gas phase slows down the cooling of the bed material.

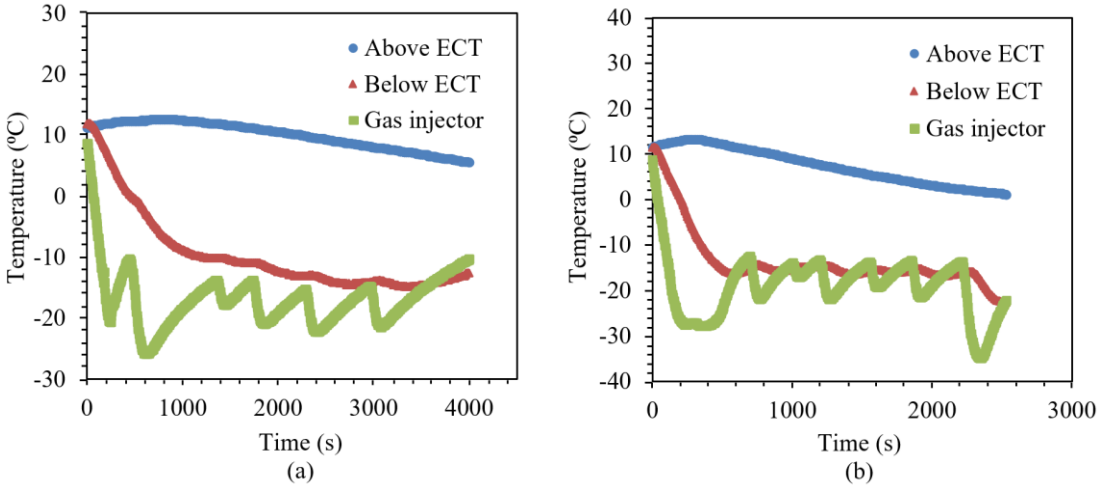

Figure 5-9: Temperature profiles of thermocouples above ECT, below ECT and gas injector under (a) 50 LPM (b) 100 LPM (100% N_2).

Unexpectedly, the temperature profiles do not show a temperature plateau at 0 °C. The reason for this is not entirely known. The most likely reason for the lack of a temperature plateau is that the ceramic bed material is wetted before being added to the capture column, which means there is minimal water presenting on the thermocouples during the experimental runs. Whereas in CO_2 frost experiments, the CO_2 frost desublimes out of the gas phase onto the bed material and likely desublimes onto the thermocouples as well. With no water freezing on the thermocouples, no temperature plateau is measured. The ECT sensors record a significant change in relative permittivity of the capture column, which indicates that water is freezing inside the capture column. Furthermore, samples of bed material taken from the capture column after the capture step show that frost presents on the bed material.

Figure 5-10 shows the ECT profiles for the water frost and ceramic bed material experiments during the water ice forming progress. Due to the different physical properties of water and CO_2, ECT for the wet packing frosting experiments needs to be calibrated separately. Based on the temperature profile, the temperature below ECT is 0 °C at approximately 4 minutes. Two minutes later, the ECT capacitance reached a peak value and this point is used as high calibration in the image reconstruction. A few minutes later, capacitance is keeping stable, and those points are used as low calibration in the image reconstruction. The calibration measurements are not made instantaneously, rather they are averaged over 60 seconds at a rate of 714 frames per second. This curve is consistent with the change of water relative permittivity with temperature. The reconstructed imaging therefore is expected to gradually change in permittivity distribution as high relative permittivity material (water) is frosting to low relative permittivity mater (ice).

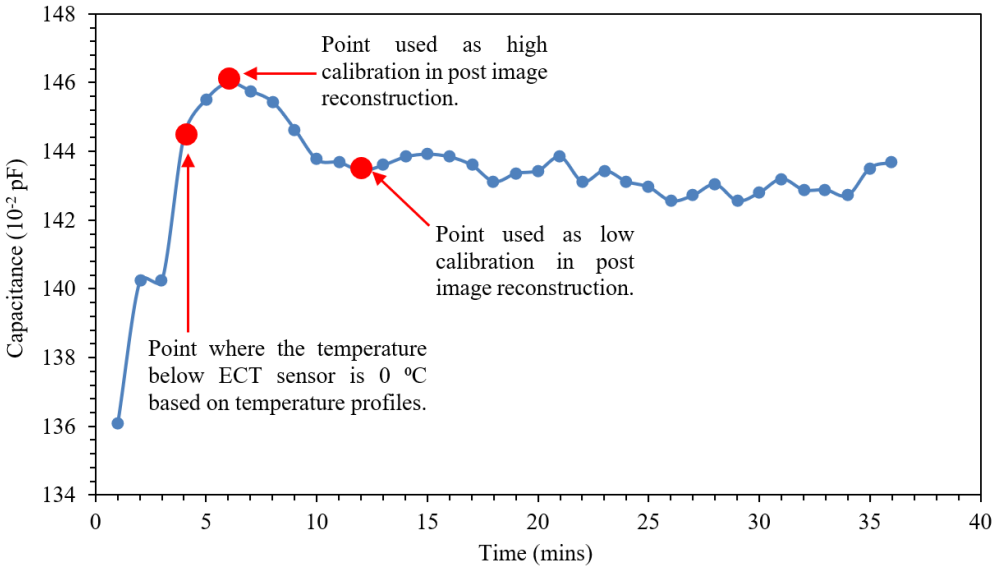

Figure 5-10: ECT measured capacitance for ceramic bed and water frost experiments.

5.3.4 Real-time measurement of frost distribution

In this section, dynamic imaging of ceramic packing cooling and water wetted ceramic packing frosting progress is carried out to validate the performance of the designed sensor. In ECT analysis, the capacitance change is used as an indicator to infer the frost formation in the packed column. Figure 5-11 shows the reconstructed permittivity

images for the experimental time sequence of frost development after the ceramic beads are wetted. The colour map of the reconstructed images is set to the same scale to facilitate the comparison. Two-end and single-end calibration methods used have been already described in Section 2.6.

In Figure 5-11, the processes in the bed over time are reconstructed in real-time with two calibration methods. The overall trend of the two calibration methods is the same. While for the two-end calibration method, the full calibration with high permittivity media is inconvenient to acquire as it would require the packed bed to be completely filled with water. Therefore, this calibration method can be less accurate as water only exists on the surface of ceramic packing during our experiment. Comparing the image in the single-end calibration group and the two-end calibration group shows that the high permittivity material (water) has the highest proportion at the beginning of frosting progress and the low permittivity material (ice) almost fills the column after a 10-minute treatment in the cooling gas.

The single-end calibration method was chosen because it significantly reduces the error caused by inappropriate high calibration required to reconstruct the image when compared to the two-end calibration method and is therefore more suitable for a new technology to monitor real-time frost progress. The absent of high calibration could have a detrimental effect on the accuracy of the results. To compare the results with and without high calibration, the root mean square error, E_{RMS} under the single-end calibration condition is evaluated from the following equation:

$$E_{RMS} = \left(\frac{\sum_{i=1}^{M-1} \sum_{j=i+1}^{M} \left(C_{norm(i,j)} - 1\right)^2}{\frac{M(M-1)}{2}} \right)^{\frac{1}{2}} \tag{5.3}$$

where M is the number of electrodes, $C_{norm(i,j)}$ is the normalised capacitance of the electrode pair *i-j*. According to Yang [141], the average E_{RMS} of the single-end calibration method is 7.1% compared with two-end calibration method. The quantitative assessment in this work shows an acceptable decline in accuracy with the single-end method using the values of low calibration data only, with $E_{RMS} \approx 5\%$ (using equation (5.3)). The results of the single-end calibration group show that a clear

boundary of a circle shape can be identified in the centre area of the reconstructed images. Results from Figure 5-11 show that the cooling progress has less effect on the permittivity located at the centre of the packed column. In the experimental data, liquid on the surface of ceramic beads causes the ECT capacitance to change from 0.41% in the first minute to 2.96% after ten minutes, which shows a clear effect of permittivity change during frost forming progress. A reasonable explanation for the result is that water has permittivity changes in a different form (liquid and solid). Prior to frost formation, the wetted ceramic beads with high permittivity are kept in the packed column. Later, the frost formed during the cooling results in the change of overall permittivity distribution after the frost appears. Consequently, the permittivity within the packed column is decreased and ECT monitors the change of permittivity distribution. However, the reconstructed images in both methods have some red area close to the boundary of the image. The most likely explanation for those red dots is that there is considerably less water at the boundary close to the pipe wall than the centre area, so the frost formation permittivity change contributes significantly less at these areas. It has been proved that for cylindrical ECT sensors, the average spatial resolution greatly increases near the electrodes. Therefore, the teeth around the edges could be an artefact caused by ceramics beads as the cylindrical packing are filled up. Figure 5-11 (c) shows the image reconstruction of the packed bed using the single-end calibration method and MSBP algorithm [142]. In comparison with the two-end calibration method result shown in Figure 5-11 (a), the single-end calibration method shows better reconstruction accuracy and better noise tolerance.

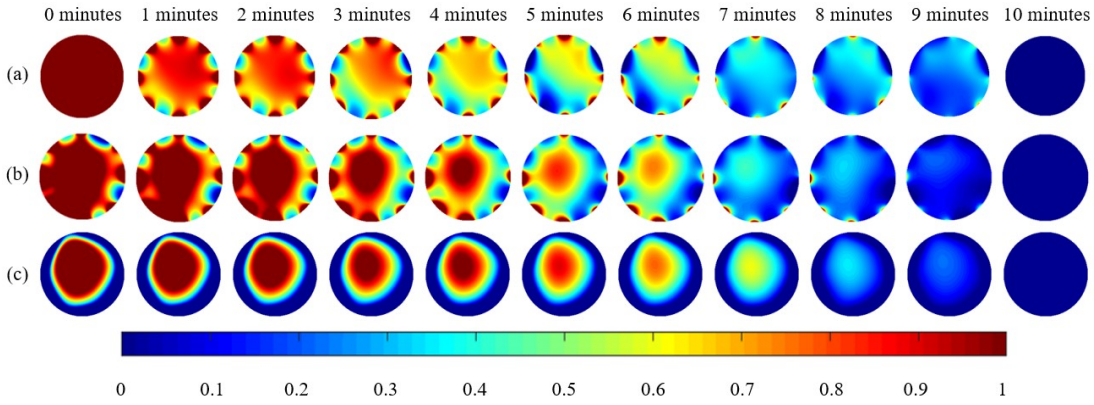

Figure 5-11: Image reconstruction of the wetted ceramic packing with (a) two-end calibration method with Landweber algorithm (b) single-end calibration method with Landweber algorithm (c) single-end calibration method with MSBP algorithm from 0 minutes to 10 minutes.

The reconstructed images show the phase of water in the bed material from liquid droplets to solid frost. The reconstructed images show that the colour change is roughly uniform across the cross section of the capture column, and as previously mentioned, indicate that the gas flow through the pipe is relatively uniform. However, there appears to be some areas close to the wall which did not change in colour due to permittivity close to the wall not changing over time. This is most likely attributable to water not being present close to the wall due to the experimental set-up. The calibration method would therefore record no change at the wall.

It is found that in CO_2 frosting experiments shown in section 5.3.2, ECT results are affected by selection of packing material. The results presented for water frost show potential for the application of ECT to cryogenic carbon capture. However, the high relative permittivity of the ceramic bed prevents the ECT sensor from detecting the small relative change in permittivity of CO_2 phase change. It would therefore be recommended in future work the selection of a bed material with a lower relative permittivity. It is anticipated that a packing material with lower permittivity, such as glass beads, should improve the detection of CO_2 frost. In addition, the preliminary model used in this work predicted that ceramic bed material with a high relative permittivity would see a significant decrease in relative permittivity when CO_2 frost forms on the surface. Complete coverage of CO_2 frost on the ceramic surface would affect the total permittivity of the ceramic material. It was expected that a bed material with high relative permittivity would show the greatest level of change in experiments.

However, this has not been the case in the experiments, which could mean that CO_2 frost is not fully coating the bed material. The possible reason for this is either that the bed material will have points of contact with each other to prevent frost completely surrounding each individual bead or that the frost nucleation and growth does not uniformly cover the surface of the bed material. Future modifications to the testing rig such as using a transparent column would help the observation of CO_2 frost formation phenomena. In order to perform sensitivity analyses, it is recommended to change more experimental conditions and variables to test their impact on frost distribution. Considering the low-temperature environment, the effect of change in temperature on the measurement capacitance must be recompensed.

5.4 Conclusions

In this chapter, the application of ECT for frost formation monitoring relevant to cryogenic carbon capture is investigated. This work found that the ceramic bed's high relative permittivity prevents the ECT sensor from detecting a small relative change in permittivity. Early experiments show challenges in detecting CO_2 frost formation using ECT. The experimental results with wetted ceramic packing showed that ECT could detect the permittivity change inside the packed column due to the frost formation progress with a high temporal resolution. ECT could strengthen the current understanding of CO_2 frost formation on fixed packed beds. Therefore, it would be recommended in future work that ECT be used to demonstrate control of cryogenic carbon capture with a moving bed packed column using real-time images, combined with knowledge of frost front velocity and thermal equilibrium.

Publications from this chapter:

- **Y. Chen**, D. Cann, J. Jia, C. Font-Palma, Preliminary Study of CO_2 Frost Formation during Cryogenic Carbon Capture using Tomography Analysis, Fuel, vol. 328, p. 125271, 2022.

Chapter 6 Conclusions and future work

6.1 Thesis overview

CCS is an essential technology for addressing global warming. ECT can accurately predict liquid retention and monitor liquid distribution, and if applied, can optimise packed column design and improve CO_2 capture rates. However, gaps in the state-of-the-art measurement methods prevent capture plants from operating optimally, leading to the vast majority of existing designs being too conservative. In addition, the parameters measured in real-time by existing plants cannot detect flooding in real-time. This thesis advances the current understanding of flooding and CO_2 frosting in the packed column by conducting simulation and experiments. The application of ECT could monitor, diagnose and optimise the performance of post-combustion capture technologies in terms of safety and CO_2 absorption efficiency.

6.2 Summary of findings

6.2.1 Key Findings - Diagnosis of Packed Column

In Chapter 3, a feasibility study is presented to investigate the potential of ECT for packed column flooding monitoring. A qualitative study of ECT images to discover liquid distribution in a counter-current flow packed column at different flow regimes. In addition, the ECT provides quantitative research of capacitance data to evaluate the relationship between flooding and a flooding index. The evolution from pre-loading to flooding status in the cross-sectional liquid distribution along the axial direction of the column is recorded and examined.

- Reconstructed images by ECT can provide a spatial distribution of liquid across different sections of a column, thus indicating the transition of flow regimes and the formation process of flooding.

- ECT is a non-intrusive, portable imaging method. It could be deployed at the carbon capture process to optimise packed column performance.

- The experimental results demonstrate that flooding can be predicted by using the flooding index method. The standard deviation of the flooding index is caused by turbulent flow.

- Dynamic datasets are obtained for three scenarios using ECT installed at the bottom position of the packed column

    - Packed column pre-loading region

    - Packed column loading region

    - Packed column flooding region

- Dynamic datasets are obtained for three scenarios using ECT installed at the top position of the packed column

    - Packed column pre-loading region

    - Packed column loading region

    - Packed column flooding region

6.2.2 Key Findings - Dynamic Flooding Monitoring

In Chapter 4, for the purpose of dynamic flooding monitoring, a portable monitoring strategy using CNN-aided ECT is proposed. A portable ECT sensor is employed for free movement in the longitudinal direction of the packed column. At each axial position, pressure drop, liquid holdup and flow information data is simultaneously recorded at the same sampling rate at the lab-scale test rig. This study shows that the flooding can be detected earlier by local liquid holdup than global liquid holdup or pressure drop. Compared with the conventional liquid holdup calculation model, the newly introduced CNN-aided method is more accurate, especially for data from dynamic flooding test campaign.

- As observed in experiment, transient disturbances flooding can result in large

fluctuations in ECT estimated local liquid holdup.

- A novel CNN with a relatively large data set is employed to predict the local liquid holdup within 1% mean of difference and 1.3% standard deviation. The flooding experiment results have verified the performance of the CNN with the largest relative error of 8.5%.

- Results confirm that a local measurement of liquid holdup tends to be the earliest prognostic of flooding than the conventional pressure drop method or the liquid holdup method. The comparison among varying process variables shows that the local liquid holdup estimated by ECT gives the earliest detection of loading point and early warning of flooding.

- ECT is highly suitable for accurately predicting the occurrence of flooding and may be deployed in packed column operation to allow for a closer process to the flooding point and reduce column size and capital costs.

- Dynamic datasets with 3 quantitative variables (capacitance, pressure drop, and liquid holdup) are obtained for three scenarios at the bottom position of the packed column

    - Packed column pre-loading region

    - Packed column loading region

    - Packed column flooding region

- Dynamic datasets with 3 quantitative variables (capacitance, pressure drop, and liquid holdup) are obtained for three scenarios at the top position of the packed column

    - Packed column pre-loading region

    - Packed column loading region

    - Packed column flooding region

6.2.3 Key Findings - Cryogenic Carbon Capture Testing

In Chapter 5, ECT is used to monitor the growth of frost from the cryogenic carbon capture progress in a packed bed. A ECT sensor which is suitable for cryogenic packed column was constructed. This study enables a better understanding of the behaviour of CO_2 frost formation from a mixture of gases during controlled experiments in a packed column. With a ECT aided design, real-time imaging of frost formation on a cryogenic packed column could provide valuable information about the deposition process within the column. Investigators or operators can modify the flow of fuel gas according to the ECT images.

- The tomographic sensor could not accurately detect CO_2 frost growth on the surface of the bed material. This could be due to the relative permittivity of CO_2 in the solid and vapour phase as well as the ceramic bed material or the setup of the experiment is ineffective.

- Considering the low-temperature environment, the effect of change in temperature on the measurement capacitance must be recompensed.

- Inference from theoretical models and ECT results show that CO_2 frost is not fully coating the bed material. The possible reasons for this are either that the bed material will have points of contact with each other to prevent frost from fully insulating each individual bead or that the frost nucleation and growth do not uniformly cover the surface of the bed material.

- Dynamic datasets are obtained for three scenarios using ECT installed at cryogenic carbon capture packed column

    - Cryogenic packed column pre-cooling process

    - Cryogenic packed column deposition process

    - Cryogenic packed column desublimation process

6.3 Recommendations for future work

Although this study initialises a new *in situ* packed column analysis method for carbon capture applications, there are still many research directions to continue this work further:

- **Evaluating different packings**: In future work, a wider variety of packings can be tested, with packing void fraction and material permittivity appearing to have the most significant impact on ECT imaging. With the help of ECT, efforts can be made to design and evaluate new packings. For example, amine-based direct air capture technology captures CO_2 directly from the atmosphere.

- **Design of new sensors**: With regards to the development of the ECT system, a further simplification of ECT sensors is worth studying. A 2-electrode configuration may be sufficient to detect frost front or flooding front and provide quantitative measurements, although the 2-electrode setup cannot provide spatial distribution information and reconstructed images.

- **Diagnosing maldistribution inside packed columns:** One of the challenges in improving mass transfer efficiency is the timely detection and diagnosis of liquid maldistribution inside packed columns. Portable and mobile features of ECT make it convenient to be applied in different locations to diagnose suspected maldistribution in packed columns.

- **Analysis of moving bed**: Powders or small particles could lead to powder fluidisation and ultimately to flooding [143]. ECT could detect powers distribution and prevent excessive accumulation of powders using real-time images. Quantitative methods can also be developed to demonstrate the control of an ECT-aided moving bed.

In the long term, a more general ECT system should be promoted to capture the critical plant operating parameters in real time for carbon capture control systems, as differences in carbon capture design significantly impact capture efficiency. Completing these goals would represent a significant step toward implementing

comprehensive measurement systems for the carbon capture process, allowing the carbon capture plant to operate as safely as possible and save operating costs.

Appendix A - Further analysis on pressure drop using Ergun's equation and Stichlmair's equation

This chapter will use Ergun's equation and Stichmair's equation to estimate the pressure drop and compare it with actual measurements from the experiments in Chapter 3. Ergun's equation can estimate the pressure drop of dry packing. Stichlmair's equation can estimate the pressure drop of irrigated packing. The derivation steps of both equations are shown below.

Calculate the pressure drop for a polypropylene Sulzer Mellapak 250 Y structured packing under the following conditions:

Gas velocity: U_G = 1.64 m/s

Liquid loading: U_L = 38.9 $m^3(m^2\ h)^{-1}$ = 0.0108 $m^3(m^2\ s)^{-1}$

Properties:

Gas density ρ_g=1 kg m^{-3}

Liquid density ρ_l=1000 kg m^{-3}

Kinematic viscosity of air = 1.416×10^{-5} $m^2\ s^{-1}$ at 10 ºC [144]

Kinematic viscosity of water = 1.307×10^{-6} $m^2\ s^{-1}$ at 10 ºC [145]

Packing type: Polypropylene Sulzer Mellapak 250 Y structured packing (α= 250 m^2/m^3; ε= 0.85)

Total height of packing: two sections of Mellapak 250.Y pp of 315mm and two additional section of 157.5 mm. Total height h=0.945 m

Calculation of the dry packing pressure drop by using Ergun's equation

$$\Delta P = \frac{150\times\mu\times L}{D_p^2}\frac{(1-\varepsilon)^2}{\varepsilon^3}v_s + \frac{1.75\times L\times\rho}{D_p}\frac{(1-\varepsilon)}{\varepsilon^3}v_s|v_s|$$
$$= \frac{150\times 1.307\times 10^{-6}\times 0.945}{(3.6\times10^{-3})^2}\frac{(1-0.85)^2}{0.85^3}v_s + \frac{1.75\times 0.945\times 1}{3.6\times10^{-3}}\frac{(1-0.85)}{0.85^3}v_s|v_s|$$
$$= 303.8\ N\ m^{-2} \qquad (a1)$$

Steps above are repeated with gas velocity increased from 1.64 to 3.47 m/s. The results are plotted in Figure A-1.

Calculation of the pressure drop by using J. Stichlmair's equation

Firstly, the equivalent diameter of the packing is calculated by using following equation.

$$d_p = \frac{6(1-\varepsilon)}{\alpha} = \frac{6(1-0.85)}{250} = 3.6\times10^{-3}\ m \qquad (a2)$$

Then the friction factor for a single particle is calculated.

$$f_0 = \frac{C_1}{Re_g} + \frac{C_2}{Re_g^{\frac{1}{2}}} + C_3 \qquad (a3)$$

where Reynolds number for the gas is given by

$$Re_g = \frac{d_p U_g \rho_g}{\mu_g} = \frac{3.6\times10^{-3}\times U_g\times 1}{14.16\times10^{-6}} = \frac{3.6\times10^{-3}\times 1.64\times 1}{14.16\times10^{-6}} = 416.9 \qquad (a4)$$

Constants for Polypropylene Sulzer Mellapak 250 Y structured packing

$$f_0 = \frac{1}{Re_g} + \frac{1}{Re_g^{\frac{1}{2}}} + 0.32 = \frac{1}{416.9} + \frac{1}{416.9^{\frac{1}{2}}} + 0.32 = 0.371 \qquad (a5)$$

Estimated dry pressure drop is calculated using equation (a6).

$$\Delta P_{est} = \frac{3}{4} f_0 \frac{1-\varepsilon}{\varepsilon^{4.65}}\rho_G \frac{Z}{d_p} U_G^2 \qquad (a6)$$

$$\Delta P_{est} = \frac{3}{4}0.371\frac{1-0.85}{0.85^{4.65}}\frac{0.945}{6\times10^{-4}}1.64^2 = 376.4\ N\ m^{-2}$$

where Z is total height of packing: two section of Mellapak 250.Y pp of 315mm and two additional section of 157.5 mm. Total height: Z = 0.945 m

$$\frac{\Delta P_{dry}}{\rho_L g Z} = \frac{376.4}{1000 \times 9.81 \times 0.945} = 0.0406 \qquad (a7)$$

Liquid holdup, below the loading point is given by equation (a8).

$$h_0 = 0.555 Fr_L^{\frac{1}{3}} = 0.555 \times (6.33 \times 10^{-3})^{\frac{1}{3}} = 0.103\ m^3\ m^{-3} \qquad (a8)$$

In equation (a8) Fr_L is the Froude number for liquid, which is given by equation (a9).

$$Fr_L = \frac{U_L^2 a}{g \varepsilon^{4.65}} = \frac{0.0108^2 \times 250}{9.81 \times 0.85^{4.65}} = 6.33 \times 10^{-3} \qquad (a9)$$

Exponent c for calculation of the irrigated pressure drop is given by following equations.

$$c = \frac{\partial \ln(f_0)}{\partial \ln(Re_g)} \qquad (a10)$$

$$c = \frac{-\frac{C_1}{Re_g} - \frac{C_2}{2Re_g^{\frac{1}{2}}}}{f_0} \qquad (a11)$$

$$c = \frac{-\frac{1}{416.9} - \frac{0.031}{(2 \times 416.9^{0.5})^{-1}}}{0.371} = -3.42 \qquad (a12)$$

The irrigated pressure drop is obtained by iterative calculations. In the first step, assume that the irrigated pressure is equal to the dry pressure drop.

$$\frac{\Delta P_{irr}}{\rho_L g Z} = \frac{\Delta P_{dry}}{\rho_L g Z} \times \frac{\left\{1 - \varepsilon \left[1 - \frac{h_0}{\varepsilon}\left[1 + 20\left(\frac{\Delta P_{irr}}{\rho_L g Z}\right)^2\right]\right]\right\}^{\left(2 + \frac{c}{3}\right)}}{1 - \varepsilon} \times \left[1 - \frac{h_0}{\varepsilon}\left[1 + 20\left(\frac{\Delta P_{irr}}{\rho_L g Z}\right)^2\right]\right]^{-4.65} \qquad (a13)$$

$$\frac{\Delta P_{irr}}{\rho_L g Z} = 0.0745 \qquad (a14)$$

$$\frac{\Delta P_{irr}}{Z} = 0.0745 \times 9.81 \times 1000 = 730.87\ N\ m^{-2} \qquad (a15)$$

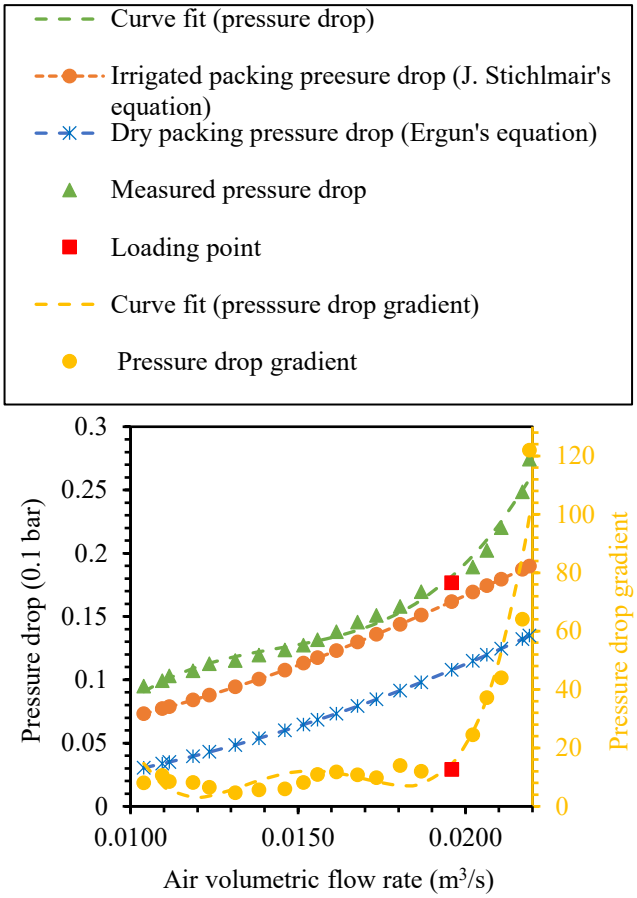

Figure A-1: Dependence of pressure drop, gradient of pressure drop and estimated pressure drop on air volumetric flow rate.

The pressure drop of the gas, for the given liquid and gas loadings, is 730.87 N m^{-2} per meter of packed height. Calculation steps above are repeated with gas velocity increased from 1.64 to 3.47 m/s. The results are plotted in Figure A-1. Compared with the estimated pressure drop values based on Ergun's equation, Stichlmair's equation can estimate pressure drop values, which are closer to measured pressure drop before loading point, but not after. Stichlmair's equation should be further tuned to cover a wider range of flow regime. Because pressure drop measurement in this work is a secondary method to validate ECT technique, detailed pressure drop estimation presented above is not included in the Chapter 3, but Ergun's equation and Stichlmair's equation were mentioned in the literature review.

Appendix B - Liquid holdup calculation procedures

In this section, the liquid holdup is calculated by the conventional ECT model without reconstructing the image. The results further validate the superiority of the CNN approach introduced in Chapter 4. The raw experiment data is revisited, and electrode capacitance values measured from two opposite electrodes, which are electrode pairs 1-5, 2-6, 3-7 and 4-8. The liquid holdup could be estimated without the image reconstruction procedure [107]. This model has been used in previous literature as a simple method for liquid in mixture ratio calculation. Examples include Li et al. [107] and Xie [109]. The step-by-step liquid holdup calculation procedures are shown below.

$$C_{norm} = \frac{\frac{1}{C_m(\varepsilon_m)} - \frac{1}{C_l(\varepsilon_l)}}{\frac{1}{C_h(\varepsilon_h)} - \frac{1}{C_l(\varepsilon_l)}} \tag{b1}$$

where C_{norm} is the normalized capacitance. C_m is the measured raw capacitance from one of the electrode pairs 1-5, 2-6, 3-7 and 4-8. C_l and C_h are the low-permittivity and high-permittivity calibration capacitances, respectively. The mixture permittivity model is derived from Ramu-Rao's model and proposed by Li et al [7] to achieve a physics-based quantification of water liquid ratio from the raw capacitance measurements.

$$\varepsilon_m = \frac{1}{C_n(\frac{1}{\varepsilon_h} - \frac{1}{\varepsilon_l}) + \frac{1}{\varepsilon_l}} \tag{b2}$$

where ε_m is the mixture permittivity. ε_h is the permittivity of water in this study. ε_l is the permittivity of gas. The relative permittivity of water is approx. 80, which is much larger than that of plastic packing approx. 2, that of air approx. 1. It was assumed that $\varepsilon_h = 80$, $\varepsilon_l = 1$. The liquid holdup calculation is given by the gas-liquid dielectric mixing model.

$$\alpha_{liquid} = \left(\frac{\varepsilon_m - \varepsilon_{gas}}{\varepsilon_{liquid} - \varepsilon_{gas}}\right)^{\frac{1}{x}} \tag{b3}$$

where α_{liquid} is the water liquid ratio, ε_{gas} the permittivity of air, ε_{liquid} the permittivity of water. x is a measurement path-dependent empirical parameter. x=0.45 is applied in this study.

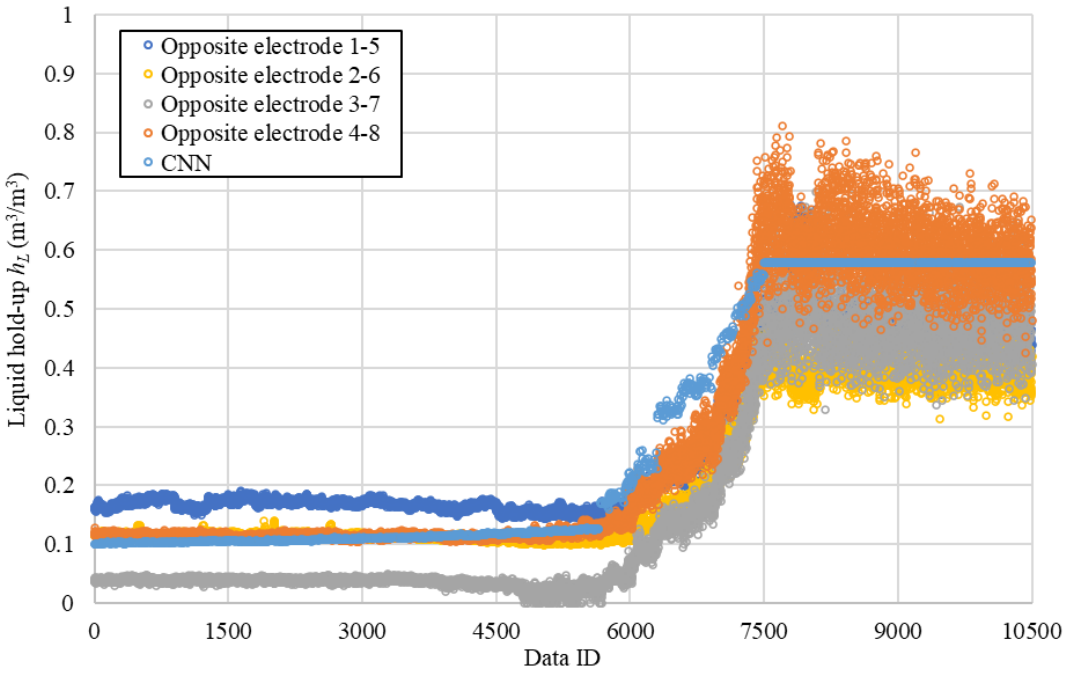

Figure B-2: Comparison between the calculated liquid holdup for opposite electrodes 1-5, 2-6, 3-7, 4-8 and CNN predicted results.

Figure B-1 shows the liquid holdup h_L calculated in the gas-liquid dielectric mixing model from the selected 2-electrode pair. The calculated liquid holdup from four different opposite electrode pairs shows a similar trend as the CNN results, although there is a wide deviation between the results obtained using various opposite electrode pairs. In addition, the selection of the measurement path-dependent empirical parameter x has a significant impact on the accurate estimation of liquid holdup. It would be expected that the model's predictions would be most accurate for flows before the loading regime. That is, the gas phase is dominant, while the liquid phase is well dispersed with the gas phase. However, results predicted by the model suffer from a non-linear behaviour with the increase of liquid holdup. Compared with the conventional method, the main advantage of CNN is that it automatically detects the important features from capacitance measurements without any empirical parameter and selection of the measurement path (opposite electrode pair), which makes CNN a more generic solution to solve the non-linear problem.

References

[1] A. Costello *et al.*, "Managing the health effects of climate change: lancet and University College London Institute for Global Health Commission," *The lancet,* vol. 373, no. 9676, pp. 1693-1733, 2009.

[2] K. P. Shine, J. S. Fuglestvedt, K. Hailemariam, and N. Stuber, "Alternatives to the global warming potential for comparing climate impacts of emissions of greenhouse gases," *Climatic Change,* vol. 68, no. 3, pp. 281-302, 2005.

[3] J. Gibbins and H. Chalmers, "Carbon capture and storage," *Energy policy,* vol. 36, no. 12, pp. 4317-4322, 2008.

[4] H. Chalmers, M. Lucquiaud, J. Gibbins, and M. Leach, "Flexible operation of coal fired power plants with postcombustion capture of carbon dioxide," *Journal of Environmental Engineering,* vol. 135, no. 6, pp. 449-458, 2009.

[5] Y. Chen, Z. Li, Y. Yang, J. Jia, C. Liu, and M. Lucquiaud, "Simulation of Flooding Phenomenon in Packed Column using Electrical Capacitance Tomography," in *2019 IEEE International Conference on Imaging Systems and Techniques (IST)*, 2019: IEEE.

[6] R. Stockfleth and G. Brunner, "Holdup, pressure drop, and flooding in packed countercurrent columns for the gas extraction," *Industrial & engineering chemistry research,* vol. 40, no. 1, pp. 347-356, 2001.

[7] Z. Li, Y. Chen, Y. Yang, C. Liu, M. Lucquiaud, and J. Jia, "Flow regime transition in countercurrent packed column monitored by ECT," *Chemical engineering journal,* vol. 420, p. 129841, 2021.

[8] F. Heymes, P. M. Demoustier, F. Charbit, J. L. Fanlo, and P. Moulin, "Hydrodynamics and mass transfer in a packed column: case of toluene absorption with a viscous absorbent," *Chemical engineering science,* vol. 61, no. 15, pp. 5094-5106, 2006.

[9] T. J. Cai, G. Chen, C. W. Fitz, and J. Kunesh, "Effect of bed length and vapour maldistribution on structured packing performance," *Chemical Engineering Research and Design,* vol. 81, no. 1, pp. 85-93, 2003.

[10] W. Yang, "Design of electrical capacitance tomography sensors," *Measurement science & technology,* vol. 21, no. 4, p. 042001, 2010.

[11] G. Liu, J. Lan, Y. Cao, Z. Huang, Z. Cheng, and Z. Mi, "New insights into transient behaviors of local liquid-holdup in periodically operated trickle-bed reactors using electrical capacitance tomography (ECT)," *Chemical engineering science,* vol. 64, no. 14, pp. 3329-3343, 2009.

[12] M. Hamidipour, F. c. a. Larachi, and Z. Ring, "Cyclic operation strategies in trickle beds and electrical capacitance tomography imaging of filtration dynamics," *Industrial & engineering chemistry research,* vol. 49, no. 3, pp. 934-952, 2010.

[13] H. Wang, G. Zhao, and G. Qiu, "Investigation the solid phase distribution in the inlet of multi-cyclone of a circulating fluidized bed by electrical capacitance tomography," *Journal of Engineering Thermophysics,* vol. 35, no. 1, pp. 109-113, 2014.

[14] H. Wu *et al.*, "Liquid distribution and hold-up measurement in counter current flow packed column by electrical capacitance tomography," *Chemical Engineering Journal,* vol. 353, pp. 519-532, 2018.

[15] B. K. Singh, S. Roy, and V. V. Buwa, "Bubbling/slugging flow behavior in a cylindrical fluidized bed: ECT measurements and two-fluid simulations," *Chemical Engineering Journal,* vol. 383, p. 123120, 2020.
[16] P. Marchot, D. Toye, A. M. Pelsser, M. Crine, G. L' Homme, and Z. Olujic, "Liquid distribution images on structured packing by X‐ray computed tomography," *AIChE Journal,* vol. 47, no. 6, pp. 1471--1476, 2001.
[17] Y. Yang, L. Peng, and J. Jia, "A novel multi-electrode sensing strategy for electrical capacitance tomography with ultra-low dynamic range," *Flow Measurement and instrumentation,* vol. 53, pp. 67-79, 2017.
[18] D. Dong, A. Tukker, and E. Van der Voet, "Modeling copper demand in China up to 2050: A business‐as‐usual scenario based on dynamic stock and flow analysis," *Journal of Industrial Ecology,* vol. 23, no. 6, pp. 1363-1380, 2019.
[19] BP. (2020, 18 Aug). *BP Energy Outlook*. Available: https://www.bp.com/content/dam/bp/business-sites/en/global/corporate/pdfs/energy-economics/energy-outlook/bp-energy-outlook-2020.pdf
[20] M. Bui *et al.*, "Carbon capture and storage (CCS): the way forward," *Energy & environmental science.,* vol. 11, no. 5, pp. 1062-1176, 2018.
[21] S. Pye, F. G. Li, J. Price, and B. Fais, "Achieving net-zero emissions through the reframing of UK national targets in the post-Paris Agreement era," *Nature energy,* vol. 2, no. 3, pp. 1-7, 2017.
[22] J. Gibbins and M. Lucquiaud, "The development of UK CCUS strategy and current plans for large-scale deployment of this technology," in *Annales des Mines-Responsabilite et environnement*, 2022, vol. 105, no. 1, pp. 26-30: FFE.
[23] A. Peter, X. Jin, X. Fan, K. I.-I. Eshiet, Y. Sheng, and D. Yang, "Effect of CO2 Phase on Pore Geometry of Saline Reservoir Rock," *Rock Mechanics and Rock Engineering,* vol. 55, no. 4, pp. 1907-1930, 2022.
[24] A. Peter, X. Jin, X. Fan, K. I.-I. Eshiet, Y. Sheng, and D. Yang, "Microscopy and image analysis of the micro-fabric and composition of saline rocks under different phaseCO2-Brine states," *Journal of Petroleum Science and Engineering,* vol. 208, p. 109411, 2022.
[25] C. Font Palma *et al.*, "Integrated Oxyfuel Power Plant with Improved CO2 Separation and Compression Technology for EOR application," 2016.
[26] C. Chao, Y. Deng, R. Dewil, J. Baeyens, and X. Fan, "Post-combustion carbon capture," *Renewable and Sustainable Energy Reviews,* vol. 138, p. 110490, 2021.
[27] Z. Chen, "A Review of Pre-combustion Carbon Capture Technology," in *2022 7th International Conference on Social Sciences and Economic Development (ICSSED 2022)*, 2022, pp. 524-528: Atlantis Press.
[28] S. Li *et al.*, "Mathematical modeling and numerical investigation of carbon capture by adsorption: Literature review and case study," *Applied Energy,* vol. 221, pp. 437-449, 2018.
[29] X. E. Hu *et al.*, "A review of N-functionalized solid adsorbents for post-combustion CO2 capture," *Applied Energy,* vol. 260, p. 114244, 2020.
[30] C. Font-Palma, D. Cann, and C. Udemu, "Review of cryogenic carbon capture innovations and their potential applications," *C,* vol. 7, no. 3, p. 58, 2021.

[31] I. Douna *et al.*, "Experimental investigation of polysulfone modified cellulose acetate membrane for CO2/H2 gas separation," *Korean Journal of Chemical Engineering,* vol. 39, no. 1, pp. 189-197, 2022.
[32] A. Lyngfelt, "Chemical looping combustion: Status and development challenges," *Energy & Fuels,* vol. 34, no. 8, pp. 9077-9093, 2020.
[33] O. Khalifa, I. I. Alkhatib, D. Bahamon, A. Alhajaj, M. R. Abu-Zahra, and L. F. Vega, "Modifying absorption process configurations to improve their performance for Post-Combustion CO2 capture–What have we learned and what is still Missing?," *Chemical Engineering Journal,* vol. 430, p. 133096, 2022.
[34] B. Sreenivasulu, D. Gayatri, I. Sreedhar, and K. Raghavan, "A journey into the process and engineering aspects of carbon capture technologies," *Renewable and Sustainable Energy Reviews,* vol. 41, pp. 1324-1350, 2015.
[35] A. Einbu *et al.*, "Energy assessments of onboard CO2 capture from ship engines by MEA-based post combustion capture system with flue gas heat integration," *International Journal of Greenhouse Gas Control,* vol. 113, p. 103526, 2022.
[36] C. Preston, C. Bruce, and M. Monea, "An Update on the Integrated CCS Project at SaskPower's Boundary Dam Power Station," in *14th Greenhouse Gas Control Technologies Conference Melbourne*, 2018, pp. 21-26.
[37] Saskpower. (2022, 12 July). *Boundary Dam Power Station*. Available: https://www.saskpower.com/Our-Power-Future/Our-Electricity/Electrical-System/System-Map/Boundary-Dam-Power-Station
[38] E. Montpetit, "Policy networks, federal arrangements, and the development of environmental regulations: a comparison of the Canadian and American agricultural sectors," *Governance,* vol. 15, no. 1, pp. 1-20, 2002.
[39] R. S. Haszeldine, "Carbon capture and storage: how green can black be?," *Science,* vol. 325, no. 5948, pp. 1647-1652, 2009.
[40] R. P. Lively, R. R. Chance, and W. J. Koros, "Enabling low-cost CO2 capture via heat integration," *Industrial & Engineering Chemistry Research,* vol. 49, no. 16, pp. 7550-7562, 2010.
[41] E. I. Koytsoumpa, C. Bergins, and E. Kakaras, "The CO 2 economy: Review of CO 2 capture and reuse technologies," *The Journal of supercritical fluids.,* vol. 132, pp. 3-16, 2018.
[42] L. Tan, A. Shariff, K. Lau, and M. Bustam, "Factors affecting CO2 absorption efficiency in packed column: A review," *Journal of Industrial and Engineering Chemistry,* vol. 18, no. 6, pp. 1874-1883, 2012.
[43] P. Tait, B. Buschle, K. Milkowski, M. Akram, M. Pourkashanian, and M. Lucquiaud, "Flexible operation of post-combustion CO2 capture at pilot scale with demonstration of capture-efficiency control using online solvent measurements," *International Journal of Greenhouse Gas Control,* vol. 71, pp. 253-277, 2018.
[44] H. Guo, C. Li, X. Shi, H. Li, and S. Shen, "Nonaqueous amine-based absorbents for energy efficient CO2 capture," *Applied Energy,* vol. 239, pp. 725-734, 2019.
[45] M. Erans, E. S. Sanz-Pérez, D. P. Hanak, Z. Clulow, D. M. Reiner, and G. A. Mutch, "Direct air capture: process technology, techno-economic and socio-

political challenges," *Energy & Environmental Science,* vol. 15, no. 4, pp. 1360-1405, 2022.
[46] D. Cann, C. Font-Palma, and P. Willson, "Experimental analysis of CO2 frost front behaviour in moving packed beds for cryogenic CO2 capture," *International journal of greenhouse gas control,* vol. 107, p. 103291, 2021.
[47] M. Tuinier, H. Hamers, and M. van Sint Annaland, "Techno-economic evaluation of cryogenic CO2 capture—A comparison with absorption and membrane technology," *International Journal of Greenhouse Gas Control,* vol. 5, no. 6, pp. 1559-1565, 2011.
[48] D. G. Cann, "Experimental exploration of cryogenic CO2 capture utilising a moving bed," Ph.D Thesis, Faculty of Science and Engineering, University of Chester, 2021.
[49] A. Ali, K. Maqsood, N. Syahera, A. B. Shariff, and S. Ganguly, "Energy minimization in cryogenic packed beds during purification of natural gas with high CO2 content," *Chemical Engineering & Technology,* vol. 37, no. 10, pp. 1675-1685, 2014.
[50] K. Nasrifar and M. Moshfeghian, "Prediction of carbon dioxide frost point for natural gas and LNG model systems," *Journal of natural gas science and engineering,* vol. 76, pp. 103206-, 2020.
[51] C.-F. Song, Y. Kitamura, S.-H. Li, and W.-Z. Jiang, "Analysis of CO2 frost formation properties in cryogenic capture process," *International journal of greenhouse gas control,* vol. 13, pp. 26-33, 2013.
[52] M. J. Tuinier, v. M. Sint Annaland, G. J. Kramer, and J. A. M. Kuipers, "Cryogenic CO2 capture using dynamically operated packed beds," *Chemical engineering science,* vol. 65, no. 1, pp. 114-119, 2010.
[53] M. J. Tuinier, M. van Sint Annaland, and J. A. M. Kuipers, "A novel process for cryogenic CO2 capture using dynamically operated packed beds—An experimental and numerical study," *International journal of greenhouse gas control,* vol. 5, no. 4, pp. 694--701, 2011.
[54] P. Willson *et al.*, "Evaluation of the performance and economic viability of a novel low temperature carbon capture process," *International journal of greenhouse gas control,* vol. 86, pp. 1--9, 2019.
[55] D. Cann, C. Font-Palma, and P. Willson, "Moving packed beds for cryogenic CO2 capture: analysis of packing material and bed precooling," *Carbon Capture Science & Technology,* vol. 1, p. 100017, 2021.
[56] M. Babar *et al.*, "Efficient CO2 capture using NH2–MIL–101/CA composite cryogenic packed bed column," *Cryogenics (Guildford),* vol. 101, pp. 79--88, 2019.
[57] V. N. Shchelkunov, N. Z. Rudenko, Y. V. Shostak, and V. I. Dolganin, "Surface desublimation of carbon dioxide from binary gas mixtures," *Journal of Engineering Physics,* vol. 51, no. 6, pp. 1432--1435, 1986.
[58] J. C. Elgin and F. B. Weiss, "Liquid Holdup and Flooding in Packed Towers," *Industrial & Engineering Chemistry,* vol. 31, no. 4, pp. 435--445, 1939.
[59] H. Patel, "Fixed-bed column adsorption study: a comprehensive review," *Applied Water Science,* vol. 9, no. 3, pp. 1-17, 2019.
[60] G. Lavalle, M. Lucquiaud, M. Wehrli, and P. Valluri, "Cross-flow structured packing for the process intensification of post-combustion carbon dioxide capture," *Chemical engineering science,* vol. 178, pp. 284-296, 2018.

[61] L. H. Macfarlan, M. T. Phan, and R. B. Eldridge, "Structured packing geometry study for liquid-phase mass transfer and hydrodynamic performance using CFD," *Chemical Engineering Science,* vol. 249, p. 117353, 2022.
[62] K. K. Unger, R. Skudas, and M. M. Schulte, "Particle packed columns and monolithic columns in high-performance liquid chromatography-comparison and critical appraisal," *Journal of Chromatography A,* vol. 1184, no. 1-2, pp. 393-415, 2008.
[63] E. Hansuld, L. Briens, and C. Briens, "Acoustic detection of flooding in absorption columns and trickle beds," *Chemical Engineering & Processing: Process Intensification,* vol. 47, no. 5, pp. 871--878, 2008.
[64] R. Billet and M. Schultes, "Prediction of mass transfer columns with dumped and arranged packings: updated summary of the calculation method of Billet and Schultes," *Chemical Engineering Research and Design,* vol. 77, no. 6, pp. 498-504, 1999.
[65] A. Ousaka, A. Kariyasaki, and T. Fukano, "Prediction of flooding gas velocity in gas–liquid counter-current two-phase flow in inclined pipes," *Nuclear engineering and design,* vol. 236, no. 12, pp. 1282-1292, 2006.
[66] J. A. Rocha, J. Carlos Cardenas, C. Sosa, and J. Rosales, "Preliminary design of sieve tray extraction columns. 1. Determination of the column diameter. Flooding velocities in sieve tray extractors," *Industrial & engineering chemistry research,* vol. 28, no. 12, pp. 1873-1878, 1989.
[67] H. Leunera, M. Hapkeb, J. Sachera, M. Grünewaldb, and J.-U. Repkea, "An Advanced Approach to Design Structured Packing Columns using Miniaturized Experimental Set-Ups," *CHEMICAL ENGINEERING,* vol. 69, 2018.
[68] J. Seader, E. Henley, and D. Roper, "Separation Process Principles. Chemical and Biochemical Operations, JohnWiley & Sons," *Inc., New Jersey,* 2011.
[69] A. A. J. Breijer, J. Nijenhuis, and J. R. v. Ommen, "Prevention of flooding in a countercurrent trickle-bed reactor using additional void space," *Chemical Engineering Journal,* vol. 138, no. 1, pp. 333--340, 2008.
[70] Y. Y. Trifonov, "Flooding in two-phase counter-current flows: numerical investigation of the gas–liquid wavy interface using the Navier–Stokes equations," *International Journal of Multiphase Flow,* vol. 36, no. 7, pp. 549-557, 2010.
[71] D. Tseluiko and S. Kalliadasis, "Nonlinear waves in counter-current gas–liquid film flow," *Journal of fluid mechanics,* vol. 673, pp. 19-59, 2011.
[72] G. F. Woerlee, J. Berends, Z. Olujic, and J. de Graauw, "A comprehensive model for the pressure drop in vertical pipes and packed columns," *Chemical Engineering Journal,* vol. 84, no. 3, pp. 367-379, 2001.
[73] K. Pihlaja Roger and P. Miller John, "Detection of distillation column flooding," 2009. Available: https://patents.google.com/patent/US8216429B2/en.
[74] V. Wolf-Zöllner, F. Seibert, and M. Lehner, "Extended performance comparison of different pressure drop, hold-up and flooding point correlations for packed columns," *Chemical Engineering Research and Design,* vol. 147, pp. 699-708, 2019.

[75] Y. Taitel, D. Barnea, and A. Dukler, "A film model for the prediction of flooding and flow reversal for gas-liquid flow in vertical tubes," *International Journal of Multiphase Flow,* vol. 8, no. 1, pp. 1-10, 1982.

[76] J.-U. Repke, O. Villain, and G. Wozny, "A nonequilibrium model for three-phase distillation in a packed column: modelling and experiments," *Computers & chemical engineering,* vol. 28, no. 5, pp. 775-780, 2004.

[77] P. Amani, J. Safdari, H. Abolghasemi, M. H. Mallah, and A. Davari, "Two-phase pressure drop and flooding characteristics in a horizontal-vertical pulsed sieve-plate column," *International Journal of Heat and Fluid Flow,* vol. 65, pp. 266-276, 2017.

[78] R. Billet and M. Schultes, "Modelling of pressure drop in packed columns," *Chemical Engineering & Technology: Industrial Chemistry ‐ Plant Equipment ‐ Process Engineering ‐ Biotechnology,* vol. 14, no. 2, pp. 89-95, 1991.

[79] J. Stichlmair, J. L. Bravo, and J. R. Fair, "General model for prediction of pressure drop and capacity of countercurrent gas/liquid packed columns," *Gas separation & purification,* vol. 3, no. 1, pp. 19--28, 1989.

[80] N. Razi, O. Bolland, and H. Svendsen, "Review of design correlations for CO2 absorption into MEA using structured packings," *International Journal of Greenhouse Gas Control,* vol. 9, pp. 193-219, 2012.

[81] J. Maćkowiak, "Determination of flooding gas velocity and liquid hold ‐ up at flooding in packed columns for gas/liquid systems," *Chemical engineering & technology,* vol. 13, no. 1, pp. 184-196, 1990.

[82] A. K. Jammula, J. R. Whiteley, M. R. Resetarits, and T. J. Cai, "New Liquid Holdup and Load Point Models in the Loading Region for Sheet Metal-Structured Packings and Performance Comparisons with Literature Models," *Industrial & Engineering Chemistry Research,* vol. 59, no. 34, pp. 15309-15316, 2020.

[83] R. Billet and M. Schultes, "Predicting mass transfer in packed columns," *Chemical Engineering & Technology: Industrial Chemistry ‐ Plant Equipment ‐ Process Engineering ‐ Biotechnology,* vol. 16, no. 1, pp. 1-9, 1993.

[84] H. Uwe, "6 - X-ray computed tomography," in *Woodhead Publishing Series in Electronic and Optical Materials*Second Edition ed., 2022, pp. 207-229.

[85] M. Fourati, V. Roig, and L. Raynal, "Experimental study of liquid spreading in structured packings," *Chemical Engineering Science,* vol. 80, pp. 1-15, 2012.

[86] K. Groß *et al.*, "Analysis of Flow Patterns in High ‐ Gravity Equipment Using Gamma ‐ Ray Computed Tomography," *Chemie ingenieur technik,* vol. 91, no. 7, pp. 1032-1040, 2019.

[87] Y. Yang *et al.*, "A noninvasive X-ray technique for determination of liquid holdup in a rotating packed bed," *Chemical engineering science,* vol. 138, pp. 244-255, 2015.

[88] S. Maurer *et al.*, "Correlating bubble size and velocity distribution in bubbling fluidized bed based on X-ray tomography," *Chemical engineering journal,* vol. 298, pp. 17-25, 2016.

[89] A. Janzen *et al.*, "Investigation of liquid flow morphology inside a structured packing using X-ray tomography," *Chemical Engineering Science,* vol. 102, pp. 451-460, 2013.
[90] A. Janzen, M. Schubert, F. Barthel, U. Hampel, and E. Kenig, "Investigation of dynamic liquid distribution and hold-up in structured packings using ultrafast electron beam X-ray tomography," *Chemical Engineering and Processing: Process Intensification,* vol. 66, pp. 20-26, 2013.
[91] A. S. Brody, D. P. Frush, W. Huda, R. L. Brent, and S. o. Radiology, "Radiation risk to children from computed tomography," *Pediatrics,* vol. 120, no. 3, pp. 677-682, 2007.
[92] M. C. Shah, M. Qussai, L. T. Fernando, and F. Liang-Shih, "1 - Electrical Capacitance Tomography," in *Woodhead Publishing Series in Electronic and Optical Materials*Second Edition ed., 2022, pp. 3-29.
[93] A. Jaworski and G. Bolton, "The design of an electrical capacitance tomography sensor for use with media of high dielectric permittivity," *Measurement Science and Technology,* vol. 11, no. 6, p. 743, 2000.
[94] W. Yang and L. Peng, "Image reconstruction algorithms for electrical capacitance tomography," *Measurement science and technology,* vol. 14, no. 1, p. R1, 2002.
[95] H. Wang and W. Yang, "Application of electrical capacitance tomography in circulating fluidised beds–A review," *Applied Thermal Engineering,* vol. 176, p. 115311, 2020.
[96] L. Peng, G. Lu, and W. Yang, "Image reconstruction algorithms for electrical capacitance tomography: state of the art," *Qinghua Daxue Xuebao/Journal of Tsinghua University,* pp. 478-484, 2004.
[97] C. Xie *et al.*, "Electrical capacitance tomography for flow imaging: system model for development of image reconstruction algorithms and design of primary sensors," *IEE Proceedings G (Circuits, Devices and Systems),* vol. 139, no. 1, pp. 89-98, 1992.
[98] W. Yang, "Calibration of capacitance tomography systems: a new method for setting system measurement range," *Measurement Science and Technology,* vol. 7, no. 6, p. L863, 1996.
[99] J. Zheng, J. Li, Y. Li, and L. Peng, "A Benchmark Dataset and Deep Learning-Based Image Reconstruction for Electrical Capacitance Tomography," *Sensors,* vol. 18, no. 11, p. 3701, 2018.
[100] G. Kłosowski, T. Rymarczyk, K. Niderla, M. Rzemieniak, A. Dmowski, and M. Maj, "Comparison of Machine Learning Methods for Image Reconstruction Using the LSTM Classifier in Industrial Electrical Tomography," *Energies,* vol. 14, no. 21, p. 7269, 2021.
[101] Z. Chen, Y. Yang, and P.-O. Bagnaninchi, "Hybrid learning-based cell aggregate imaging with miniature electrical impedance tomography," *IEEE Transactions on Instrumentation and Measurement,* vol. 70, pp. 1-10, 2020.
[102] H. Zhu, J. Sun, J. Long, W. Tian, S. Sun, and L. Xu, "Deep image refinement method by hybrid training with images of varied quality in electrical capacitance tomography," *IEEE Sensors Journal,* vol. 21, no. 5, pp. 6342-6355, 2020.
[103] Z. Chen, J. Xiang, P.-O. Bagnaninchi, and Y. Yang, "MMV-Net: A Multiple Measurement Vector Network for Multifrequency Electrical Impedance

Tomography," *IEEE Transactions on Neural Networks and Learning Systems,* 2022.
[104] A. Fabijańska and R. Banasiak, "Graph convolutional networks for enhanced resolution 3D Electrical Capacitance Tomography image reconstruction," *Applied Soft Computing,* vol. 110, p. 107608, 2021.
[105] R. Yan and S. Mylvaganma, "Flow regime identification with single plane ECT using deep learning," in *9th World Congress on Industrial Process Tomography*, 2018, pp. 289-297.
[106] S. Wang, J. Ye, and Y. Yang, "Quantitative Measurement of Two-Phase Flow by Electrical Capacitance Tomography Based on 3D Coupling Field Simulation," *IEEE Sensors Journal,* vol. 21, no. 18, pp. 20136-20144, 2021.
[107] Y. Li *et al.*, "Gas oil water flow measurement by electrical capacitance tomography," *Measurement science & technology,* vol. 24, no. 7, p. 74001, 2013.
[108] S. Wang *et al.*, "Digital Twin of Electrical Tomography for Quantitative Multiphase Flow Imaging," *arXiv preprint arXiv:2112.05792,* 2021.
[109] C. g. Xie, "Measurement Of Multiphase Flow Water Fraction And Water‐cut," in *AIP Conference Proceedings*, 2007, vol. 914, no. 1, pp. 232-239: American Institute of Physics.
[110] Z. Zeeshan, C. E. Zuccarelli, D. Ospina Acero, Q. M. Marashdeh, and F. L. Teixeira, "Enhancing Resolution of Electrical Capacitive Sensors for Multiphase Flows by Fine-Stepped Electronic Scanning of Synthetic Electrodes," *IEEE transactions on instrumentation and measurement,* vol. 68, no. 2, pp. 462-473, 2019.
[111] L. Zhu, L. Ma, Y. Li, Y. Yang, and M. Zhang, "Linearization Point and Frequency Selection for Complex-Valued Electrical Capacitance Tomography," *IEEE transactions on instrumentation and measurement,* vol. 70, pp. 1-11, 2021.
[112] A. Wongkia, F. Larachi, and S. Assabumrungrat, "Hydrodynamics of countercurrent gas–liquid flow in inclined packed beds – A prospect for stretching flooding capacity with small packings," *Chemical Engineering Science,* vol. 138, pp. 256--265, 2015.
[113] C. E. Agu, L. Tokheim, M. Eikeland, and B. M. Moldestad, "Determination of onset of bubbling and slugging in a fluidized bed using a dual-plane electrical capacitance tomography system," *Chemical Engineering Journal,* vol. 328, pp. 997-1008, 2017.
[114] D. Strazza, M. Demori, V. Ferrari, and P. Poesio, "Capacitance sensor for hold-up measurement in high-viscous-oil/conductive-water core-annular flows," *Flow measurement and instrumentation,* vol. 22, no. 5, pp. 360-369, 2011.
[115] S. H. Stavland, Y. Arellano, A. Hunt, R. Maad, and B. T. Hjertaker, "Multimodal Two-Phase Flow Measurement Using Dual Plane ECT and GRT," *IEEE transactions on instrumentation and measurement,* vol. 70, pp. 1-12, 2021.
[116] S. Sun, X. Lu, L. Xu, Z. Cao, J. Sun, and W. Yang, "Real-Time 3-D Imaging and Velocity Measurement of Two-Phase Flow Using a Twin-Plane ECT Sensor," *IEEE transactions on instrumentation and measurement,* vol. 70, pp. 1-10, 2021.

[117] M. Hamidipour and F. Larachi, "Characterizing the liquid dynamics in cocurrent gas–liquid flows in porous media using twin-plane electrical capacitance tomography," *Chemical Engineering Journal,* vol. 165, no. 1, pp. 310-323, 2010.
[118] B. Matusiak, M. J. da Silva, U. Hampel, and A. Romanowski, "Measurement of dynamic liquid distributions in a fixed bed using electrical capacitance tomography and capacitance wire-mesh sensor," *Industrial & engineering chemistry research,* vol. 49, no. 5, pp. 2070-2077, 2010.
[119] R. B. White, "Using electrical capacitance tomography to monitor gas voids in a packed bed of solids," *Measurement science and technology,* vol. 13, no. 12, p. 1842, 2002.
[120] H. Wang, H. Hu, L. Wang, and H. Wang, "Image reconstruction for an Electrical Capacitance Tomography (ECT) system based on a least squares support vector machine and bacterial colony chemotaxis algorithm," *Flow Measurement and Instrumentation,* vol. 27, pp. 59-66, 2012.
[121] Y. J. Yang, L. H. Peng, and J. B. Jia, "A novel multi-electrode sensing strategy for electrical capacitance tomography with ultra-low dynamic range," *Flow Measurement and Instrumentation,* vol. 53, pp. 67-79, Mar 2017.
[122] H. Wu *et al.*, "Liquid distribution and hold-up measurement in counter current flow packed column by electrical capacitance tomography," (in English), *Chemical Engineering Journal,* vol. 353, pp. 519-532, Dec 1 2018.
[123] J. E. Buchanan, "Pressure gradient and liquid holdup in irrigated packed towers," *Industrial and Engineering Chemistry Fundamentals,* vol. 8, no. 3, pp. 502--511, 1969.
[124] A. K. Jammula, "New Liquid Holdup, Load Point and Flooding Velocity Models in Different Regions of Operations for a Structured Packed Column," ed, 2014.
[125] S. Ergun, "Fluid flow through packed columns," *Chem. Eng. Prog.,* vol. 48, pp. 89-94, 1952.
[126] I. Iliuta, F. Larachi, M. Fourati, L. Raynal, and V. Roig, "Flooding limit in countercurrent gas–liquid structured packed beds—Prediction from a linear stability analysis of an Eulerian two-fluid model," *Chemical Engineering Science,* vol. 120, pp. 49--58, 2014.
[127] J. Sun and W. Yang, "Fringe effect of electrical capacitance and resistance tomography sensors," *Measurement science and technology,* vol. 24, no. 7, p. 074002, 2013.
[128] V. Jiřičný, V. Staněk, P. Svoboda, and J. Ondráček, "Experimental study of the flooding and appearance of a bubble bed on top of a countercurrent packed-bed column," *Industrial & engineering chemistry research,* vol. 40, no. 1, pp. 407-412, 2001.
[129] Y. Chen, C. Liu, Y. Yang, M. Lucquiaud, and J. Jia, "Flooding Prognostic in Packed Columns Based on Electrical Capacitance Tomography and Convolution Neural Network," *IEEE Transactions on Instrumentation and Measurement,* vol. 71, pp. 1-14, 2022.
[130] Z. Li, Y. Chen, Y. Yang, C. Liu, M. Lucquiaud, and J. Jia, "Flow regime transition in countercurrent packed column monitored by ECT," *Chemical engineering journal (Lausanne, Switzerland : 1996),* vol. 420, p. 129841, 2021.

[131] S. Parthasarathy, H. Gowan, and P. Indhar, "Prediction of flooding in an absorption column using neural networks," in *Proceedings of the 1999 IEEE International Conference on Control Applications (Cat. No. 99CH36328)*, 1999, vol. 2, pp. 1056-1061: IEEE.
[132] D. Hu, K. Lu, and Y. Yang, "Image reconstruction for electrical impedance tomography based on spatial invariant feature maps and convolutional neural network," in *2019 IEEE International Conference on Imaging Systems and Techniques (IST)*, 2019, pp. 1-6: IEEE.
[133] Y. Jiang *et al.*, "CSTNet: A Dual-Branch Convolutional Neural Network for Imaging of Reactive Flows Using Chemical Species Tomography," *IEEE Transactions on Neural Networks and Learning Systems,* 2022.
[134] T. Sidi and C. Keasar, "Redundancy-weighting the PDB for detailed secondary structure prediction using deep-learning models," *Bioinformatics,* vol. 36, no. 12, pp. 3733-3738, 2020.
[135] K. P. Murphy, *Machine learning: a probabilistic perspective*. MIT press, 2012.
[136] P. Marchot, D. Toye, M. Crine, A. M. Pelsser, and G. L'homme, "Investigation of Liquid Maldistribution in Packed Columns by X-Ray Tomography," *Chemical Engineering Research and Design,* vol. 77, no. 6, pp. 511--518, 1999.
[137] P. A. Schweitzer, *Handbook of separation techniques for chemical engineers*. McGraw-Hill New York, 1979.
[138] A. Pavlenko, N. Pecherkin, V. Zhukov, G. Meski, and P. Houghton, "Overview of methods to control the liquid distribution in distillation columns with structured packing: Improving separation efficiency," *Renewable and Sustainable Energy Reviews,* vol. 132, p. 110092, 2020.
[139] Y. Chen, D. Cann, J. Jia, and C. Font-Palma, "Preliminary study of CO2 frost formation during cryogenic carbon capture using tomography analysis," *Fuel,* vol. 328, p. 125271, 2022.
[140] R. Span and W. Wagner, "A new equation of state for carbon dioxide covering the fluid region from the triple-point temperature to 1100 K at pressures up to 800 MPa," (in English), *Journal of Physical and Chemical Reference Data,* Review vol. 25, no. 6, pp. 1509-1596, Nov-Dec 1996.
[141] J. Eckert, E. Foote, and L. Walter, "What effects packing performance," *Chemical Engineering Progress,* vol. 62, no. 1, pp. 59-&, 1966.
[142] J. Jia, M. Wang, and Y. Faraj, "Evaluation of EIT systems and algorithms for handling full void fraction range in two-phase flow measurement," *Measurement Science and Technology,* vol. 26, no. 1, p. 015305, 2014.
[143] D. McGlinchey, *Bulk solids handling: equipment selection and operation*. John Wiley & Sons, 2009.
[144] EngineeringToolBox. (2003, 5 June). *Air - Dynamic and Kinematic Viscosity*. Available: https://www.engineeringtoolbox.com/air-absolute-kinematic-viscosity-d_601.html?vA=10&units=C
[145] Engineersedge. (2022, 5 June). *Water - Density Viscosity Specific Weight*. Available: https://www.engineersedge.com/physics/water__density_viscosity_specific_weight_13146.htm